Fractal Analysis of Image Structures

Oldřich Zmeškal, Michal Veselý, Martin Nežádal, Miroslav Buchníček
Institute of Physical and Applied Chemistry, Brno University of Technology
Purkynova 118, 612 00 Brno, Czech Republic
zmeskal@fch.vutbr.cz

Introduction of terms

Fractals

- Fractals are of rough or fragmented geometric shape that can be subdivided in parts, each of which is (at least approximately) a reduced copy of the whole.
- They are crinkly objects that defy conventional measures, such as length and are most often characterised by their fractal dimension
- They are mathematical sets with a high degree of geometrical complexity that can model many natural phenomena. Almost all natural objects can be observed as fractals (coastlines, trees, mountains, and clouds).
- Their fractal dimension strictly exceeds topological dimension

Fractal dimension

- The number, very often non-integer, often the only one measure of fractals
- It measures the degree of fractal boundary fragmentation or irregularity over multiple scales
- It determines how fractal differs from Euclidean objects (point, line, plane, circle etc.)

Monofractals / Multifractals

- Just a small group of fractals have one certain fractal dimension, which is scale invariant. These fractals are monofractals
- The most of natural fractals have different fractal dimensions depending on the scale. They are composed of many fractals with the different fractal dimension. They are called „multifractals“
- To characterise set of multifractals (e.g. set of the different coastlines) we do not have to establish all their fractal dimensions, it is enough to evaluate their fractal dimension at the same scale

Self-similarity/ Semi-self similarity

- Fractal is strictly self-similar if it can be expressed as a union of sets, each of which is an exactly reduced copy (is geometrically similar to) of the full set (Sierpinski triangle, Koch flake). The most fractal looking in nature do not display this precise form
- Natural objects are not union of exact reduced copies of whole. A magnified view of one part will not precisely reproduce the whole object, but it will have the same qualitative appearance. This property is called statistical self-similarity or semi-self-similarity

Box-Counting method

- One of the methods used to establish fractal dimension
- It determines the fractal dimension of black&white digitised images of fractals
- It works by covering fractal (its image) with boxes (squares) and then evaluating how many boxes are needed to cover fractal completely. Repeating this measurement with different sizes of boxes will result into logarithmical function of box size (*x*-axis) and number of boxes needed to cover fractal (*y*-axis). The slope of this function is referred as box dimension. Box dimension is taken as an appropriate approximation of fractal dimension.

Mass method/ Radius dimension method

- Further method used to establish fractal dimension
- It determines the fractal dimension of black&white digitised images of fractals too
- It is based on determination of the dependency between count of black and white pixels (picture elements) on the square (circle – radius dimension method) shaped plane, with the varying area. The slope of this dependency is the mass/radius dimension, it is a good approximation of fractal dimension. Resulting mass/radius dimension should be almost the same or the same as the box dimension.

Fractal analysis

- A collection of mathematical procedures used to determine fractal dimension (or any other fractal characteristic) or set of fractal dimensions (in the case of multifractals) with the smallest error.
- Nowadays very often used to characterise properties if natural objects
- Method under continuous scientific development

HarFA

- Software equipment to perform fractal and harmonic analysis of digitised images
- Was built up by authors of this contribution
- Is available to be freely download on http://www.fch.vutbr.cz/lectures/imagesci

Description of method

To implement Box-Counting method software called HarFA was built up. Dimension determined by this method is called Box Dimension D_{BBW}. This method has simple principle: a square mesh of various sizes $1/\varepsilon$ is laid over the image object. The count of mesh boxes $N_{BBW}(\varepsilon)$ that contain any part of the fractal are counted (e.g. squares which are completely filled up by the fractal N_B and squares which contains just part of fractal N_{BW} are summed together). The slope of the linear portion of a function $\ln(N_B + N_{BW}) = \ln(N_{BBW}) = f(N_{BBW}(\varepsilon))$, where $\ln N_{BBW}(\varepsilon) = \ln K_{BBW} + D_{BBW} \ln(\varepsilon)$, gives D_{BBW} the fractal (box) dimension. Dimension D_{BBW} is referred as classical box dimension and can be easily find in many literature sources.

When modify this method (counting black N_B, white N_W and partially black squares N_{BW} separately) three new fractal dimensions D_B, D_W, D_{BW} can be achieved. D_B and D_W characterise fractal properties of black and white plane, while D_{BW} characterises properties of black&white border. So, we can say that HarFA can compute five independent fractal dimensions. The most important are dimensions D_{BW}, D_{BBW}, D_{WBW} (arises by summing squares N_W which are not filled up by the fractal so they remain white and squares which contains just part of fractal N_{BW}), while D_B and D_W are accidental, they are meaningful just for Euclidean objects (line, circle, square etc.). It's called **Linear Regression Analysis**.

To determine fractal dimension precisely is necessary to find linear portion of function $\ln(N_B + N_{BW}) = \ln(N_{BBW}) = f(N_{BBW}(\varepsilon))$. HarFA dispose of powerful tool to accomplish this goal. It's called **Single Slope Analysis**. Let's say that we have 100 data points. User of HarFA has to specify the length of analysed data points segment L_{DP} (e.g. 20). Then Slope Analysis sequently determines fractal dimension of data 1. - 20. next 2. -21. next 3. - 22...81. - 100. Finally we obtain the new set of fractal dimensions. If we display them on a graph (each point is colorized according appropriate correlation coefficient of linear regression) we can easily find linear portion of original function. It will exhibit by constant part on a new dependency (there are the same, or almost the same fractal dimensions) and by high correlation (marked by red or white colour).

But we have no assurance that value of $L_{DP} = 20$ is appropriate. So the next step is to perform Slope Analysis for all possible values of L_{DP} (from 3 to Count of Data points). This tool is called **OverAll Slope Analysis**. Its result is histogram of fractal dimension count. The

most probable value of correct fractal dimension is that with the largest count. Slope Analysis provides easy form of multifractal analysis.

As said earlier, Box-Counting method works with black&white images of fractals. But medicine or biological images are mostly displayed as grey-level images or even colorized. So we need to transform these images into black&white. Procedure to accomplish this goal is called **Masking**. HarFA provides four colour spaces conversion routines (RGB, HSB/HSV, HLS and Intensity), which enables user to select desired tint intuitively. Selected tint will be transformed into black colour and all the others tints will become white. By this way black&white fractal structure arises.

But sometimes we cannot say which colour of image is important for our purposes. For these cases there is a tool called **Fractal Analysis – Range**. Fractal dimension is automatically determined for all levels of chosen channel of colour information (Red, Green, Blue, Hue, Saturation, Brightness, Intensity). Resulting fractal dimension is displayed as a function of masked level of colour information. This dependency is called **Fractal Spectrum**. It is a new and not published method of fractal analysis.

The usage of Fractal Analysis in biological or medicine sciences

As mentioned earlier, almost all natural objects can be observed as fractals. The main „beauty“ of fractals consists in possibility to describe very complex natural phenomena (e.g. branching of trees or capillaries, fibrous structure of cells, clouds, cerebral cortex etc.) by small set of parameters. It's closely to the idea that the nature always prefers the simplest solution. Even so complex organism as anthill is composed of relatively simplex organisms, which execute a set of easy instructions. If you want to study fractals you can do it in two general ways: if you are an experimentalist, you try to calculate fractal dimension of things in nature and then you try to find the relationship between fractal dimension and some property of nature. If you are a theorist, you try to calculate fractal dimension of models chosen to describe experimental situations; if there is no agreement then you try another model. So the fractal dimension provides the benchmark against which theories are compared with experiments. HarFA provides the first way of solution. Authors of HarFA have documented the usage of HarFA in the root system analysis (Institut National de la Recherche Agronomique, France), the study of variation of shapes of dental crown pattern of voles (Moscow M.V.Lomonosov State University, Moscow), the analysis of cancer cells images (Gesellschaft fuer Schwerionenforschung, Germany), the plant cell identification (University of Florence, Italy) and many other usage within the different kinds of scientific interest (chemistry, physics, geography, sociology etc.).

Literature

1. Mandelbrot, B. B.: *Fractal Geometry of Nature*, W.H. Freeman and Co., New York, (1983).
2. Theiler, J., *Estimating fractal dimension*. Journal of the Optical Society of America, 1055±1073. (1990).
3. Buchníček M., Nežádal M., Zmeškal O.: *Numeric calculation of fractal dimension*, Nostradamus 2000, Prediction Conference, FT VUT Zlin, (2000).
4. Barnsley, M.F.: *Fractals Everywhere*, Academic Press, Boston, (1988).
5. Voss, R. *Random fractals: characterization and measurment*. R. Pynn and A. Skjeltorp, Eds., Scaling Phenomena in Disordered Systems. Plenum, New York (1986).
6. B.H. Kaye. *A Random Walk through Fractal Dimensions*, VCH Verlagsgesellschaft, Weinheim, pp 13-52, (1986)

The Fractal Dimension of Grapevine Leaves as a Tool for Ampelographic Research

Stefano Mancuso
Dipartimento di Ortoflorofrutticoltura – Polo Scientifico University of Florence –
Viale delle Idee 30 – 50019 Sesto Fiorentino (FI) – Italy
stefano.mancuso@unifi.it

Morphological leaf characters and quantitative measurements of anatomical elements of the leaf, i.e. angles, area, teeth number, petiole length, have been extensively utilised in ampelographic research (OIV-IBPGR-UPOV charts 1983; Galet 1985). However, the origin of the grapevine varieties, their heterogeneity and the frequent cases of homonimy and synonymy, often resulted in doubtful classification. It is thus important to define good shape measures that can be effectively applied to leaf shapes, so they can be compared and analysed by meaningful and objective criteria. One approach that researchers have proposed for describing biological shapes is the fractal based measure of digitally acquired images.

Many pattern of nature are either irregular or fragmented to such an extreme degree that Euclidean geometry cannot describe their form. Thus, fractal geometry based analysis has received increasing attention as a number of studies have shown fractal based measures to be useful for characterising complex biological structures. Fractal scaling is evident in natural objects from the micro-scale to the macro-scale, e.g. the human body contains many structures with fractal characteristics. In fact, it has been found that non-fractal objects were the exception, rather than the rule in many natural systems.

Figure 1: An image of grapevine leaf analysed

Thus, it seemed interesting to verify the possible application of fractal analysis to describe grapevine leaves (*Figure 1*) belonging to different genotypes with the hope to add an objective, clarifying dimension to the excessively convoluted field of ampelography.

The study was carried out with 11 putative Sangiovese-related ecotypes and the registered clone Sangiovese R 10 as a reference (*Table 1*). Samples were collected from the grapevine germplasm collection of the Department of Horticulture of the University of Florence, Italy. At the veraison, 50 fully expanded, healthy leaves, from 15 plants per accession, located between the 7th and 11th shoot node from the apex were selected according to uniformity of appearance, growth habit and exposure.

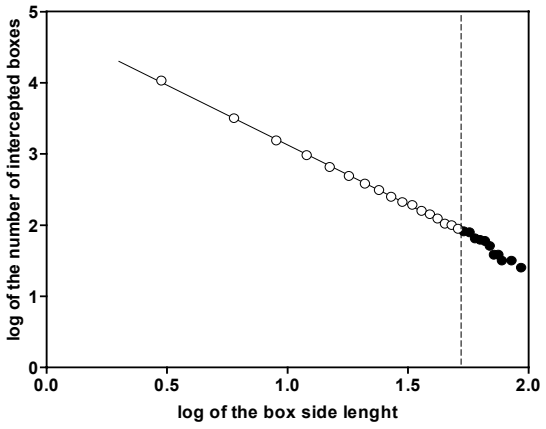

Figure 2: Determination of the fractal dimension

The steps of the box-counting algorithm were as following. The original grayscale image was thresholded to create a binary image, where leaves were represented by black pixels. An edge detection algorithm was applied to the binary image to create an image containing only the edge of the leaf.

The edge image was divided into a grid of square subimages, or "boxes", of fixed length, *d*, and the number of boxes containing part of an edge, N(*d*), was counted. N(*d*) was determined for a range of values of *d*, and then the log[N(*d*)] versus log(*d*) was plotted. The most linear portion of the curve (shown as open circle in *Figure 2*) was chosen and linear regression was performed on that segment of the curve. The box-counting dimension (BCD) was the negative of the slope of the regression line.

The typical technique for determination of the BCD consists in partitioning the image space in boxes of size *d* x *d* and counting the number N(d) of boxes that contain at least one part of the shape to be investigated. Several values of *d* are chosen and the least square fitting of log[N(*d*)] x log(*d*) is used to determine the value of BCD. However, this approximation will suffer the effects caused by spatial quantization as well as the limited fractality of most natural objects (such as grapevine leaves). Therefore the curve log[N(*d*)] x log(*d*) will exhibit two distinct regions (*Figure 2*). The error is minimized calculating D in the region where the curve is most linear. Such guidelines were applied in the present research to the grapevine leaves to obtain their fractal dimensions.

Table 1: Fractal dimension of homogeneous sets of leaves in different Sangiovese-related ecotypes.

Genotype	Mean	S. E.	Minimum	Maximum
Prugnolo gentile	1.301	0.001	1.283	1.310
Brunellone	1.294	0.001	1.271	1.316
Brunelletto	1.230	0.004	1.202	1.274
Prugnolo acerbo	1.457	0.003	1.415	1.472
Prugnolo dolce	1.448	0.001	1.426	1.462
Prugnolo medio	1.468	0.001	1.444	1.482
Casentino	1.204	0.008	1.136	1.294
Chiantino	1.240	0.003	1.216	1.298
Morellino	1.278	0.001	1.262	1.315
Morellino di Scansano	1.246	0.004	1.225	1.302
Piccolo precoce	1.499	0.002	1.471	1.512
Sangiovese R 10	1.372	0.001	1.353	1.389

The fractal dimensions of a homogeneous sample of leaves from different *Sangiovese*-related genotypes are listed in Table 1. The mean values of BCD ranged from 1.204 for *Casentino* to 1.499 for *Piccolo precoce*, showing a rather ample interval.

In spite of plant variability, the fractal dimension can be found quite accurately with a small sample size. The average standard error of D for 12 genotypes shown in Table 1, for example, was only 0.19 % (n = 50), that is much less than the standard error that occurs using the traditional ampelographic parameters.

A fundamental question on the applicability of fractal analysis to vine leaves is if vine leaves are genuine self-similar objects. Results presented here show that leaves are not truly fractal because they do not show the highly hierarchical structure characteristic of artificial fractal object. Nevertheless, the BCD gives an effective dimension that can be used to measure the complexity of highly complex structures such as vine leaves. Complex objects may show a power-law property over a limited range of scales and this property may be captured using fractal techniques. Similar discussions were met in the application of fractal analysis to other not truly fractal objects as the human trabecular bone or the neurons. Consequently, this study rather than proposing that vine leaves are fractal, emphasizes the usefulness of fractal analysis in ampelography.

Literature

1. Galet, P.: *Précis d'ampelographie pratique*. Imprimerie Charles Dehan (Ed.), Montpellier, France, 15-26. (1985)
2. OIV-IBPGR-UPOV: *Code de caractéres descriptifs des variétés et espèces de Vitis*. Office International de la Vigne e du Vin, Paris. (1983)

The Fractal Analysis of Image Structures for Microbiologic Application

Mária Veselá, Oldřich Zmeškal, Michal Veselý, Martin Nežádal
Brno University of Technology, Faculty of Chemistry
Purkyňova 118, 612 00 Brno
vesela@fch.vutbr.cz

The methods for an image analysis are used in biology and medicine more often. This is due to development of image recording equipment (digital cameras, scanners), more efficient personal computers and their peripheries (A/D converters, TV cards, Video CD, DVD) and special software for image data processing.

The harmonic and fractal analysis of the image or its colour separations belongs to the basic methods for the image analysis. This analysis can be performed by various software equipment, which is commonly available [1], [2], [3]. These software are developed for special purposes so that are not fully suitable for many applications.

At the Faculty of chemistry was developed software HarFA [4], which attempts to solve the problems of image analysis more complex, although the main area of its application is focused on fractal analysis. Just this method was used for analysis of microbiological specimens for the determination of number of yeast cells in digital image (*Figure 1*).

The image was taken by recording equipment, which consists of optical microscope SM-6, digital camera SONY and PC.

The microscope magnification, resolution of digital camera gives the connection between image size and studied sample size (10 μm per 48 pixels).

The number of cells was determined by following expectations:

1. the cells are of round shape,
2. the cells are similar in size,
3. the cells differs form background by colour.

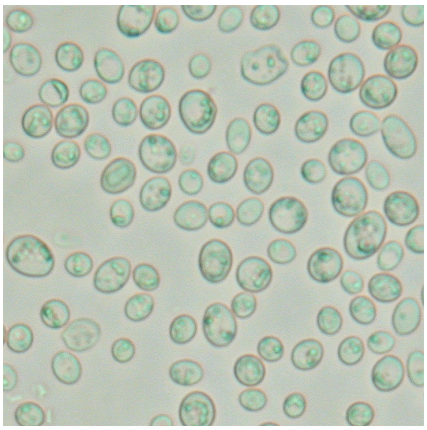

Figure 1: An image of analysed microbiologic specimen

The procedure of cell size determination and its number determination was as follows:

1. By means of proper colour separation (RGB channel, intensity, brightness, contrast) the masking procedure is made for colour adjustment – white (W) for cell and black (B) for background.
2. By means of fractal analysis the fractal dimension and fractal measure is determined for such masked image including interface (K_{WBW}, D_{WBW}) and cell interface (K_{BW}, D_{BW}). According to following equations

$$N_{BW}(\varepsilon)=K_{BW}\varepsilon^{-D_{BW}}, \quad N_{WBW}(\varepsilon)=N_W(\varepsilon)+N_{BW}(\varepsilon)=K_{WBW}\varepsilon^{-D_{WBW}}, \tag{1}$$

the quantity is connected to number of white ($N_W(\varepsilon)$) and partially white ($N_{BW}(\varepsilon)$) squares of network of size $\varepsilon\times\varepsilon$ pixels. From such determined constants is possible by using of the following equations

$$N_{BW}=x\frac{\pi(2r+\varepsilon)}{\varepsilon}\approx x\frac{2\pi r}{\varepsilon}, \quad N_{WBW}=x\frac{\pi r^2}{\varepsilon^2}, \tag{2}$$

to determine number of cells x and their round shape radius r.

From equation (1) and (2) we get

$$x=\frac{K_{BW}^2\varepsilon_m^{-2D_{BW}}}{4\pi K_{WBW}\varepsilon_m^{-D_{WBW}}}=\frac{K_{BW}^2}{4\pi K_{WBW}}\varepsilon_m^{D_{WBW}-2D_{BW}}, \tag{3}$$

where ε_m is network size, with maximum of fractal dimension. For smaller values of ε $(\varepsilon < \varepsilon_m)$ will be a border line formed by pixels of image discrete (a fractal dimension of interface will decrease), for $(\varepsilon > \varepsilon_m)$ will be a border line broad (it causes the decreasing of fractal dimension again).

In both cases it is displayed by decreasing the number of investigated cells *x*, or by increasing their radius (*Figure 3*), respectively. From this figure is possible to determine the number of cells stated by fractal analysis ($x = 100$) and their mean radius ($r = 29$ pixels).

Comparing these results with values, which are easy to estimate from *figure 2* ($x \approx 85$) we can see, that the error of determination of number of cells in this case is smaller than 15 %. The higher accuracy is achievable by optimal choice of cell size in image (it can be easy modified by change of optical magnification) and by optimal cell count in image (can be changed by dilution of cell culture).

The most proper parameters (cell size, number of cells in image) can be established by their evaluation in two ideal cases:

1. for different number *N* of round shaped cells with the same radius *r*,
2. for fixed number *N* of round shaped cells with the various radius *r*.

It was found, that the optimal size of cells (the mean radius *r*) for the image analysis is 35 pixels, the optimal cell number is approx. 50. From the analysed structure can be seen that parameters of analysed image structure are at the edge of suggested conditions. The further information will be presented on the poster.

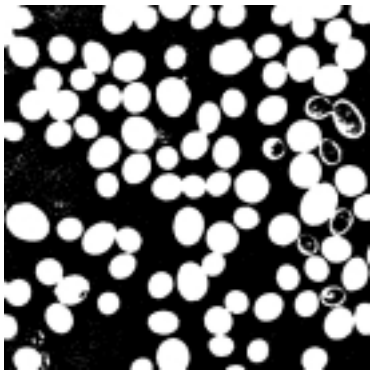

Figure 2: The masked image of microbiologic specimen

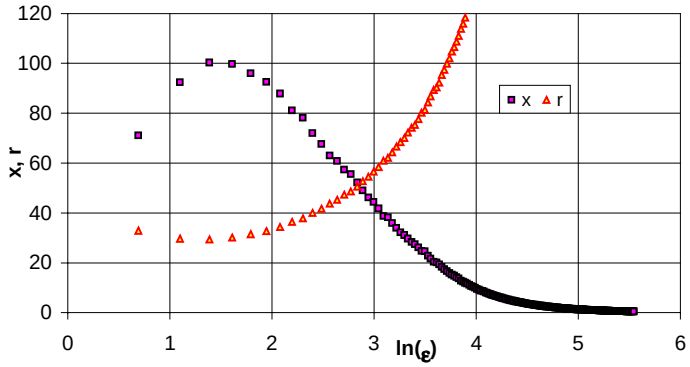

Figure 3: The determination of number of cells N and their radius r (x = 100, r = 29 pixels)

Conclusion

It is evident that the cell count determined by the fractal analysis differs from true value to about 15 %. This difference is caused by unequal cell size and shape, by quality of specimen (it should be removed the thermal noise of CCD element, should be performed the correction of illumination non-homogeneity, gamma correction) and by colour differences of individual cells. From these results we can claim that the mean size of analysed cells is 12 μm.

Literature

1. *Benoit*, Fractal Analysis System, True Soft International (1999)
2. *Lucia*, Image Archiv Plus, Users' guide, Laboratory Imaging, s.r.o., (1999)
3. Fooley J. D., van Dam A., Feiner S. K., Hughes J. F., Phillips J. R.: *Introduction to Computer Graphics*, Addison-Wesley Publishing Company, Reading USA (1997)
4. *HarFA*, Harmonic and Fractal Image Analyser, Software For Determination of Fractal Dimension, www.fch.vutbr.cz/lectures/imagesci. (2001)

Fractal Dimension Analysis of Hollow-Cone Darkfield Images

Rand Dannenberg
Chahaya Optronics, 94954 Fremont, USA

Abstract. The fractal dimension is used as a guide to setting the threshold for converting darkfield images into binary images. This can be used to support the existence of a preferred orientation in a thin film (Ag), or to get quantitative information about the phase content of multi-phase films (Ni-Ni_3P).

Summary.

Setting the threshold when converting a darkfield image to a binary one, to get quantitative information about orientation or phase content, can be tricky. It depends on the operators intuition as to when he or she feels the binary image is a good representation of the micrograph, and when comparing a series of images, can often lead to erroneous trends.

Box counting is overlaying a grid of boxes of side *s* and counting the number of boxes that contain part of the image *N(s)*. The fractal dimension *D* is defined as

$$N(s) = s^{-D}. \quad (1)$$

D governs the rate at which *N* changes with *s*.

One can estimate by visual inspection of an image some bounds on the expected form of the *log (N(s)) vs. log (1/s)* curve from a box counting routine. The threshold may then be set to meet those expectations. The operator may then compare the resulting binary image to the darkfield one, and if it's a good representation visually, then there is a supporting mathematical basis for it.

There are several regimes for the fractal dimension *D*. Consider an image that is a series of parallel lines of length *L* and spacing *d*, and width of line *w*. $L >> d >> w$. As the box size *s* falls, the dimensionality changes,

1. $D = 0$ for $s>>L$ (2)

2. $D \rightarrow 2$ for $d < s < L$ (3)

3. $D \rightarrow 1$ for $w < s < d$ ($D \sim 0$ if these are particles of diameter *w*) (4)

4. $D \rightarrow 2$ for $s < w$. (5)

5. $D = 2$ for $s<<w$ (6)

That example illustrates that the *D* computed from the slope of *log (N(s)) vs. log (1/s)* depends on magnification, density, feature size, and the size of the "measuring stick".

With this kind of visualization tool, consider the hollow cone darkfield images. They are an ideal case, as they are taken at the same magnification, are about the same size, and have similar illumination conditions. In the upper right hand corner of the 220 darkfield collage is a feature that looks like a handprint. The "palm" part of the print is 45 pixels wide. Our boxes have $s=2,3\ldots17$ pixels per side.

I assume that if an area shows *any contrast* and is not completely black, its coming from grains oriented perpendicular to the *hkl* of whatever ring is being examined. Note all

the grains in those images are nearly space filling and connected so $D>1$. Most of the time $s \leq w$ where w is the feature size so $D \rightarrow 2$ as $s << w$. Also $s \leq d$ where d is the spacing between feature edges. As s decreases, the number of boxes of side s, $N(s)$, that contain a portion of the image should increase almost as $A_{diffract}/s^2$, but slightly slower since some boxes won't be counted due to the spacing between unconnected grains, so D must be slightly less than 2. In addition, s is in pixels and does not range over many orders, so the slope D of *log (N(s)) vs. log (1/s)* will stay less than 2 and not vary too much.

This reasoning suggests setting the threshold until *log (N(s)) vs. log (1/s)* has almost the same slope for small boxes as it does for big boxes, and the slope D should be a bit less than two, but not too far away.

Fractal dimensions were computed with threshold settings for the 220, 111, 200, 311 hollow cone darkfield images for an Ag film on Si_3N_4, Table 1. By *threshold = 210* the small and large s fractal dimensions agreed more closely.

Table 1. Fractal dimensions with threshold setting.

Thresh = 210	**220**	**111**	**200**	**311**
s = 2-3	1.614242	1.702474	1.654951	1.667205
s = 13-17	1.507534	1.705807	1.766551	1.754871
Thresh = 188	**220**	**111**	**200**	**311**
s = 2-3	1.608247	1.602977	1.582639	1.547907
s = 13-17	1.313757	1.511971	1.436904	1.525707
Thresh = 150	**220**	**111**	**200**	**311**
s = 2-3	1.568375	1.52711	1.48587	1.419023
s = 13-17	0.92678	1.110822	1.163722	1.046953

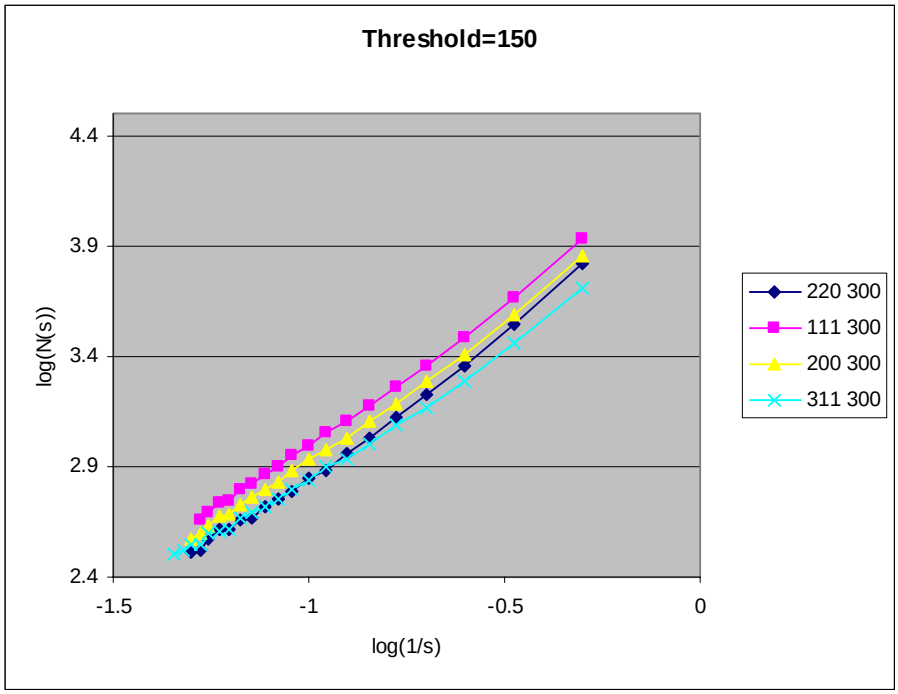

The images and graphs follow on the next pages. Note how by *threshold=188* that the 220 diffracting grains *log (N(s)) vs. log (1/s)* curves lay significantly beneath those of 111, 200, 311. This means that the total area of the 220 diffracting grains for all boxes is smaller than the others. If the film is 220 oriented, the number of grains capable of diffracting 220 should be reduced, and those capable of 111, 200, 311 reflections are increased. Ergo, this analysis supports 220 oriented Ag resulting from annealing at 300 ^{o}C of the as deposited film. Note also the rapid rise of the 311 *log (N(s)) vs. log (1/s)* curve with thresholding. Lastly, I thought the *threshold=210* was a pretty good binary representation of the overall shape of the diffracting grains. Conclusions follow pics.

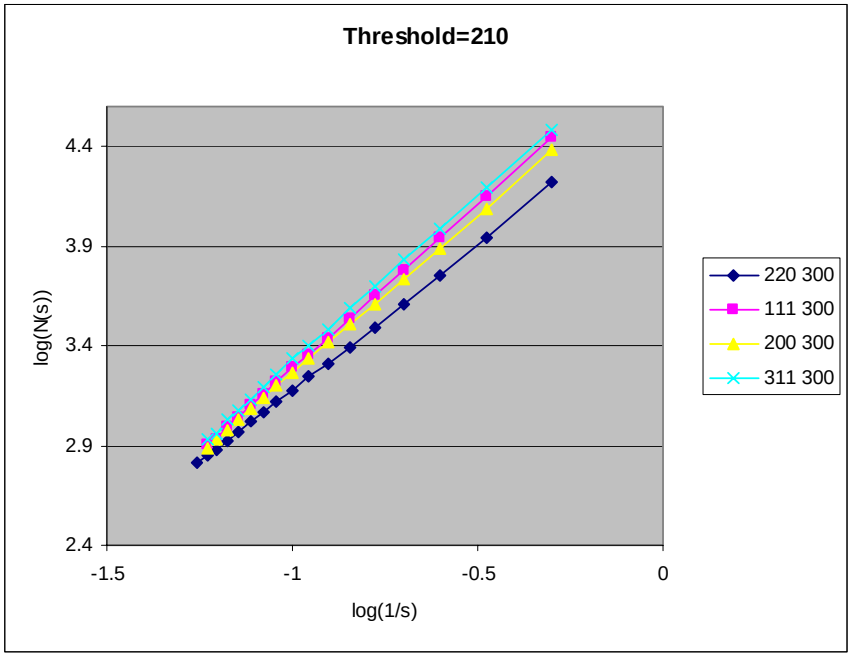

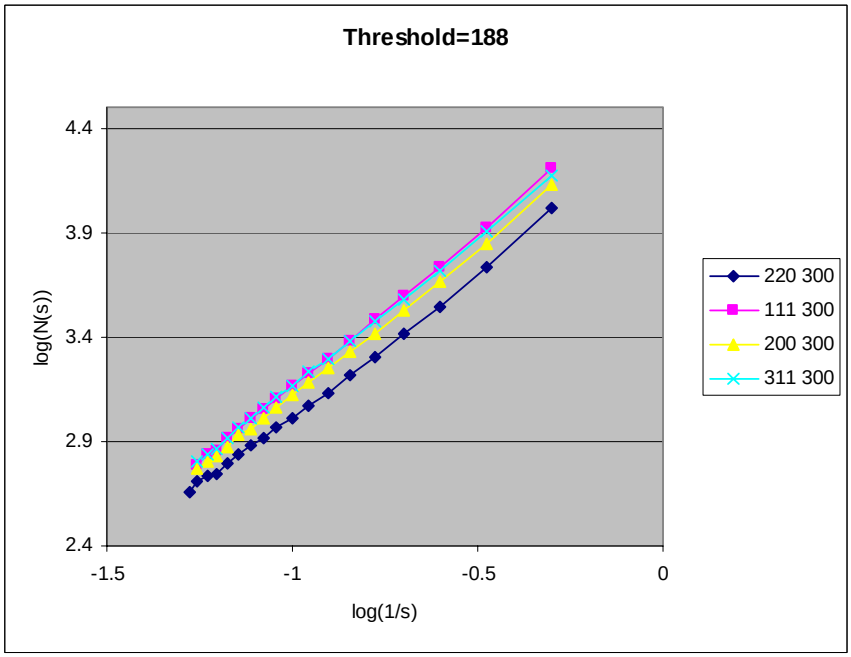

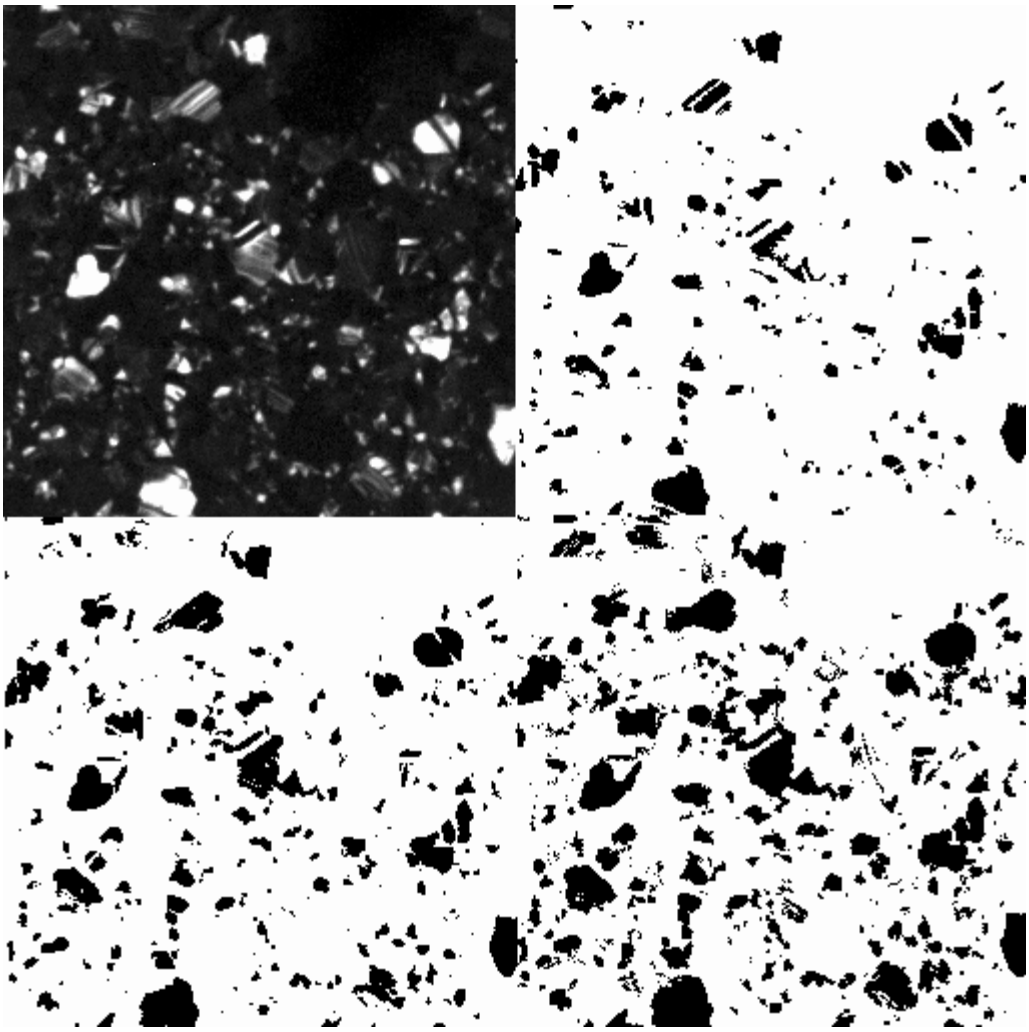

220 hollow cone and threshold=150, 188,210. See "handprint" 45 pixels wide.

Compare the "dark" non-diffracting grains in the original image to the white areas of the binary ones. The shape of the dark areas is captured more accurately in the highest threshold setting.

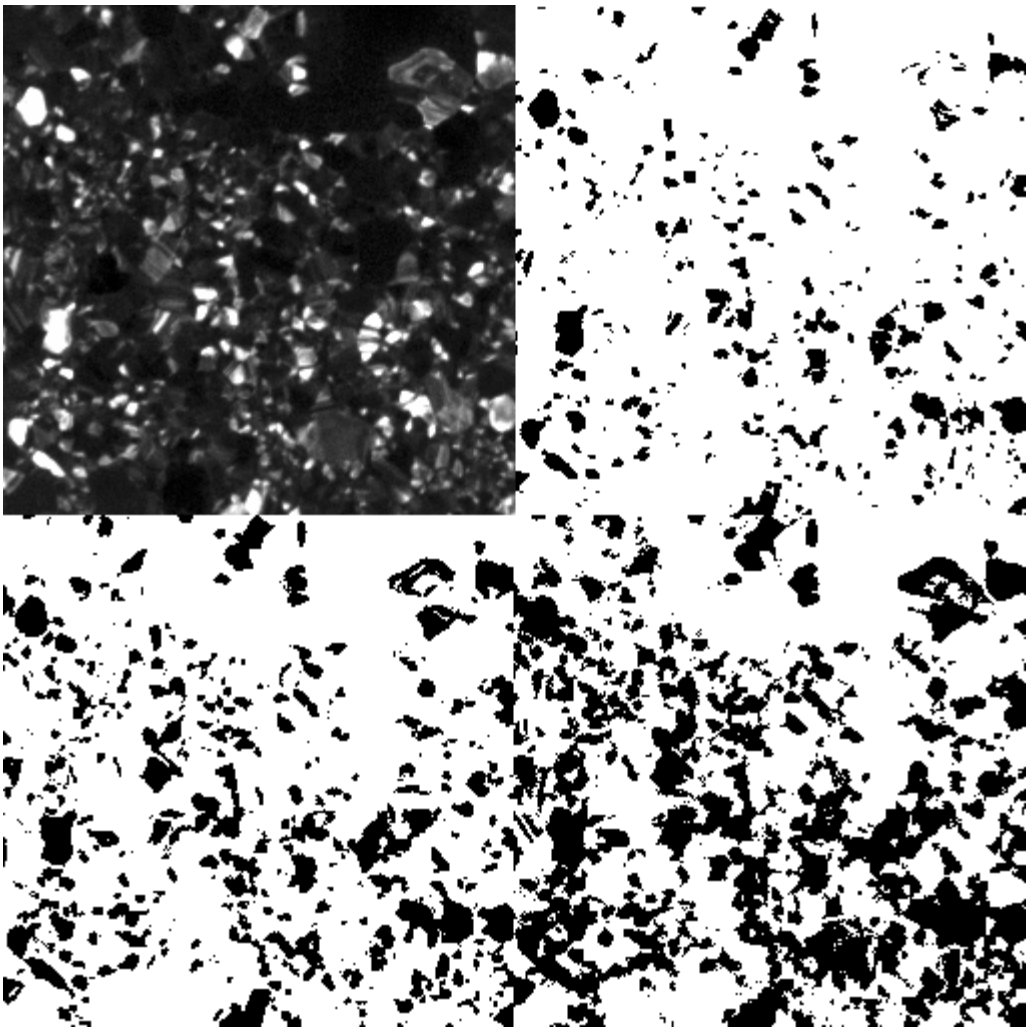

111 hollow cone and threshold=150, 188, 210.

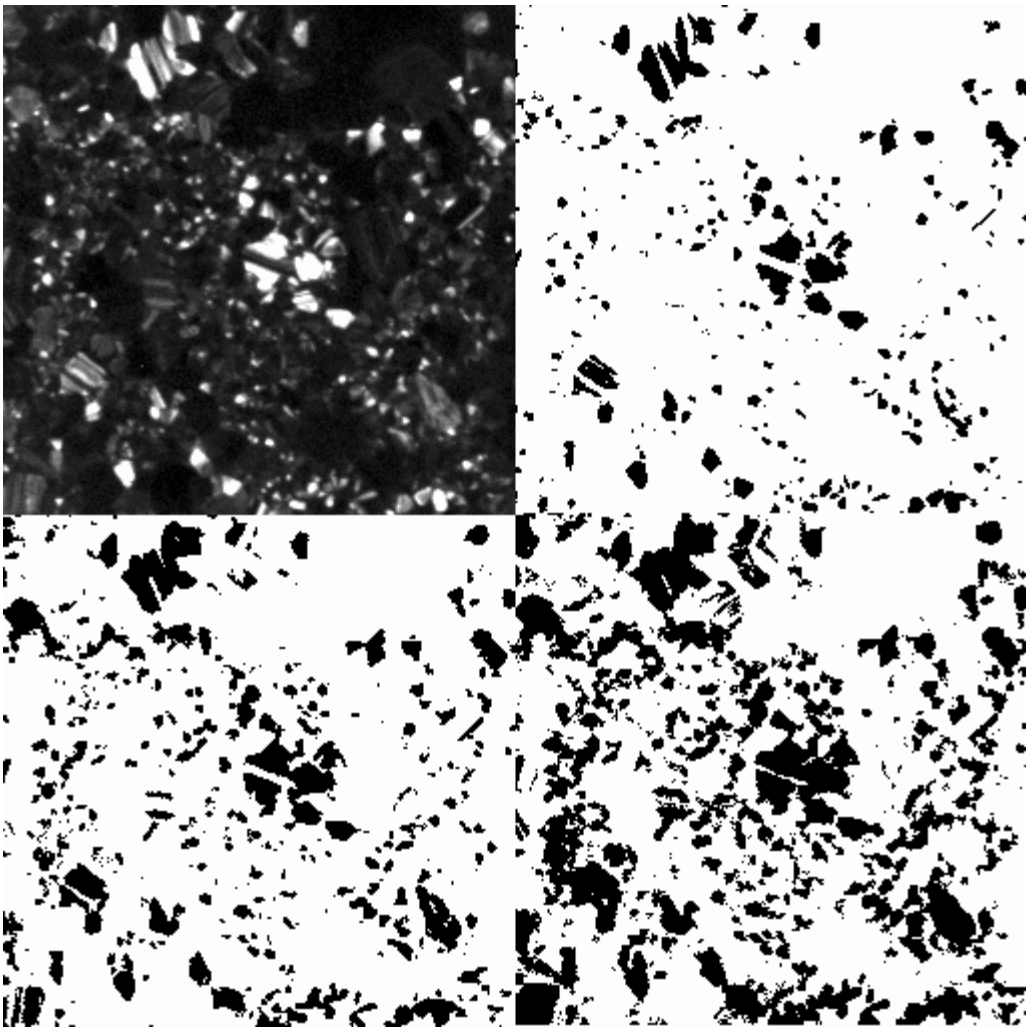

200 hollow cone and threshold=150, 188, 210.

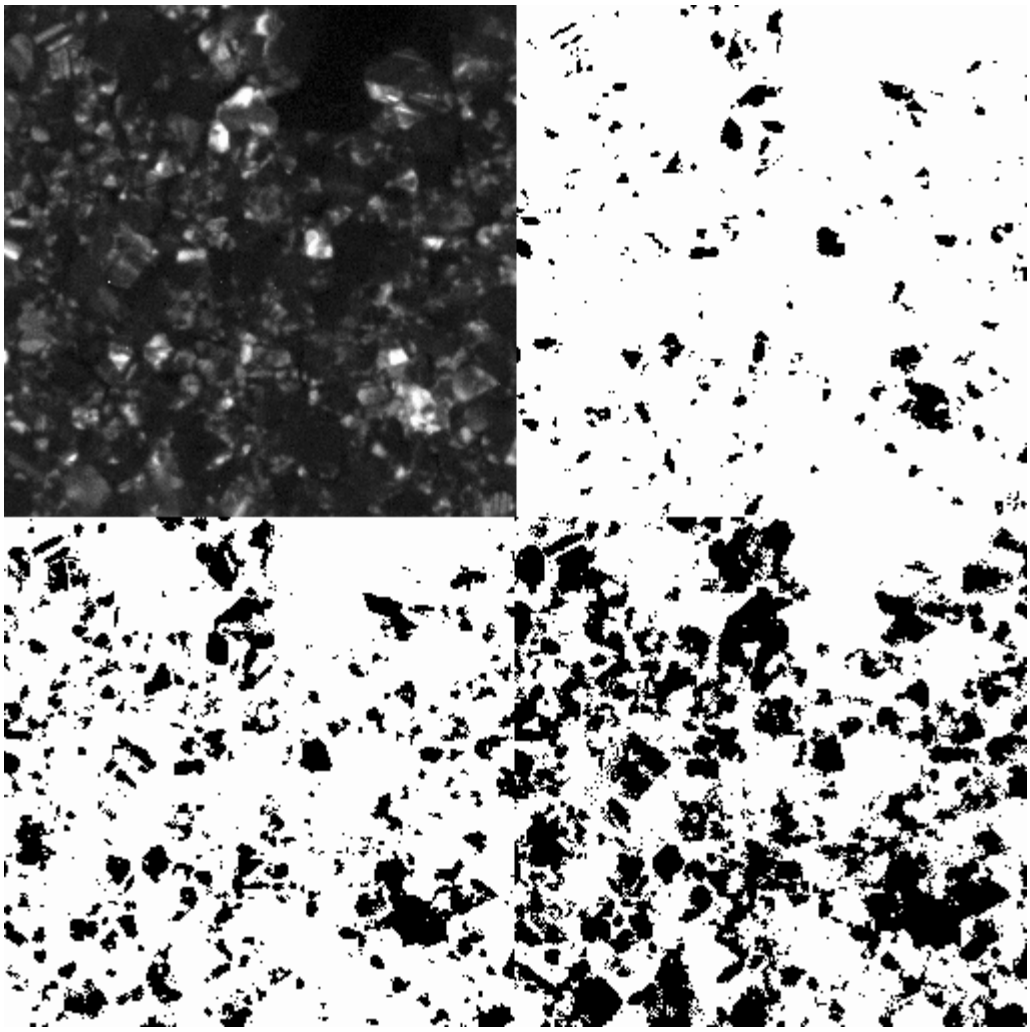

311 hollow cone and threshold=150, 188, 210.

Conclusions.

- *D~1.6-1.7* for all the grains diffracting in the hollow cone darkfield images.
- The *threshold=210* setting may be just a bit shy of the optimal setting as there is still some structure in the 220 diffracting grains.
- Setting the threshold to achieve a fairly constant *D* in the range estimated from visual inspection of the image removes some of the operator feel from the process, and allows some data to be collected without manual circling of grains or outlining.
- The analysis supports a 220 oriented film.
- Analysis of a bi-crystal series of images using the same assumptions would be helpful. The assumptions that help determine the regime of *D* which may change with microstructure.
- Hollow cone and the fractal analysis may be helpful in imaging and gaining quantitative information about Ni_3P segregating in grain boundaries of plated Ni films on heating.

Lastly, I found a much more sophisticated program call HarFA (harmonic fractal analysis) which creates some beautiful data, is very fast, and allows a larger range of boxes to be analyzed. It calculates the fractal dimension spectrum as well, so you can see structure in the *D(s)* that corresponds to the particle size distribution and distribution of spacings between particle edges. I will provide the analysis of the hollow cone images with this program shortly.

The Use of Fractal Analysis for the Determination of Cell Diameter – Model Calculation

Ondřej Sedlák, Oldřich Zmeškal, Barbora Komendová, Petr Dzik
Brno University of Technology, Faculty of Chemistry
Purkyňova 118, 612 00 Brno
sedlak@fch.vutbr.cz, zmeskal@fch.vutbr.cz, barakom@seznam.cz, dzik@atlas.cz

The methods of image analysis are being used in biology and medicine more often. This is due to the development of image recording equipment (digital cameras, scanners), more efficient personal computers and their peripheries (A/D converters, TV cards, Video CD, DVD) and special software for image data processing.

The harmonic and fractal analysis of the image or its color separations belongs to the basic methods for the image analysis. This procedure can be performed by various software tools, which are commonly available [1], [2], [3]. However, this software is developed for special purposes, and therefore it is not applicable generally.

For the past few years, the application HarFA (Harmonic and Fractal Image Analyser) [4] has been developed at the Faculty of Chemistry of BUT. This software enables the user to make various correction of the captured image, to apply filters, color separations and both harmonic and fractal analysis. It has been showed, that this software tool can be used for the characterization of the images of microscopic specimen. If we apply the fundamentals of fractal mathematics on the image of cellular structure complying with certain criteria (spherical shape of the cells, similarity of sizes and contrast background – *figure 1*), we can determine both their number and size.

If we cover the analyzed image by a virtual sampling mesh with the size of one box $\varepsilon \times \varepsilon$ pixels, we can formulate the following relations

$$N_{\mathrm{BW}}(\varepsilon)=K_{\mathrm{BW}}\varepsilon^{-D_{\mathrm{BW}}}, \quad N_{\mathrm{BBW}}(\varepsilon)=N_{\mathrm{B}}(\varepsilon)+N_{\mathrm{BW}}(\varepsilon)=K_{\mathrm{BBW}}\varepsilon^{-D_{\mathrm{BBW}}},$$

where $N_{\mathrm{B}}(\varepsilon)$ stands for the number of totally black and $N_{\mathrm{BW}}(\varepsilon)$ stands for the number of partially black boxes of that sampling mesh. D_{BW} (D_{BBW}) is so called fractal dimension and K_{BW} (K_{BBW}) so called fractal measure. Using these constants, it is possible to determine the number of cells x and their radius r

$$N_{\mathrm{BW}}=x\frac{\pi(2r+\varepsilon)}{\varepsilon}\approx x\frac{2\pi r}{\varepsilon}, \quad N_{\mathrm{BBW}}=x\frac{\pi r^2}{\varepsilon^2},$$

From these equations we get

$$x=\frac{K_{\mathrm{BW}}^2\varepsilon_m^{-2D_{\mathrm{BW}}}}{4\pi K_{WBW}\varepsilon_m^{-D_{\mathrm{WBW}}}}=\frac{K_{\mathrm{BW}}^2}{4\pi K_{WBW}}\varepsilon_m^{D_{\mathrm{WBW}}-2D_{\mathrm{BW}}}$$

where ε_m is the mesh size corresponding to the maximum of fractal dimension. For smaller values of ε ($\varepsilon < \varepsilon_m$) will be a borderline formed by pixels of image discrete (a fractal dimension of interface will decrease), for ($\varepsilon > \varepsilon_m$) will be a border line broad (it causes the decreasing of fractal dimension again). From the extremes of the curves at *figure 2*, it is possible to determine the number of cells and their radius.

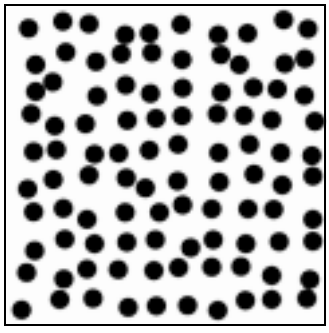

Figure 1: Model cellular structure; 100 cells, radius 38 pixels

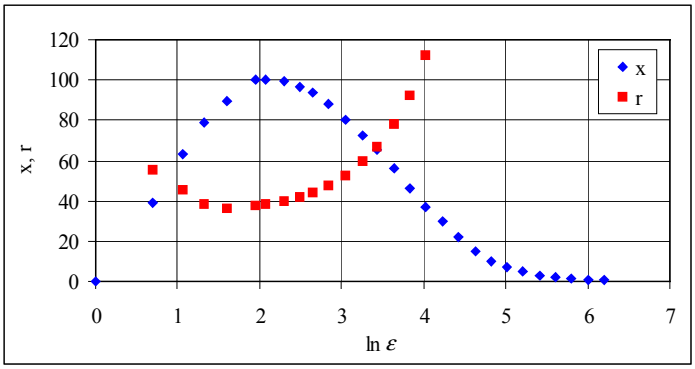

Figure 2: The determination of number of cells x and their radius r (x = 100, r = 38 pixels)

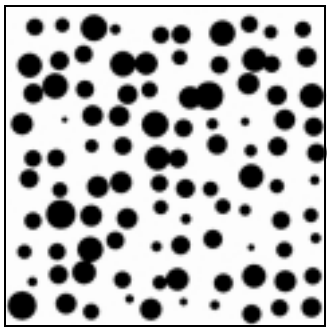

Figure 3: Model cellular structure with Gaussian size distrubution; 100 cells, mean radius 38 pixels, standard deviation 4 pixels

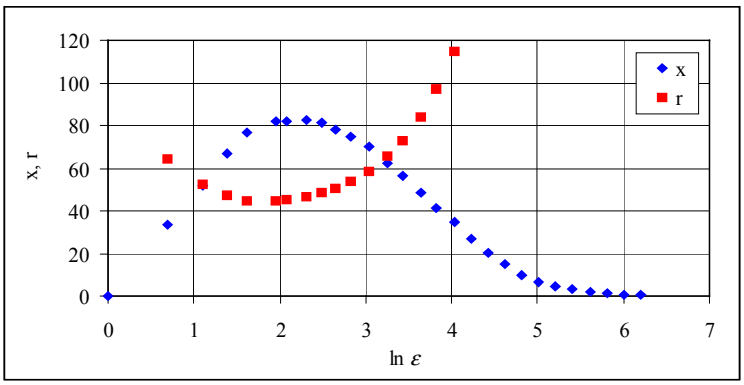

Figure 4: The determination of number of cells x and their radius r (x = 82, r = 43 pixels)

The determination of cell number and size by this method is valid only for structures consisting of cells of equal size. It was found that when the structures showing certain distribution of cell sizes (*figure 3*) were analyzed, the calculated numbers of cells were always smaller then the real numbers and on the other hand, the cell sizes were always bigger then the real sizes (*figure 4*). So, the relation between the real and calculated number of cells with respect to the distribution was studied.

For this purpose, model images were used. These images contained defined (Gaussian) distribution of cell sizes with varying standard deviation. The processing sequence described above was applied at these images and the cell number and size was calculated. Then, the dependences between the calculated number of cell and their radii *versus* selected standard deviation were evaluated. These dependences can be used as calibration curves of real cell number versus calculated cell umbers. (*figure 5, 6*).

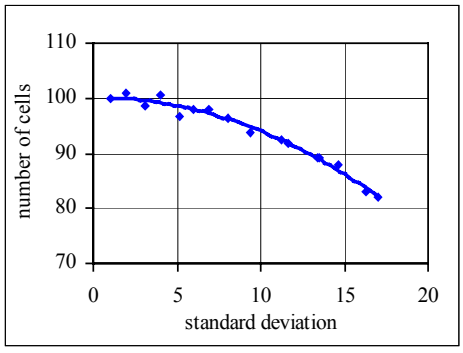

Figure 5: Calibration curve for tthe cell number for x = 100, r = 38 pixels

If we know the number of cells of certain structure, we can calculate their average radius and variation in the following way:

1. Perform the fractal analysis, by which we get a fictive number of cells and average radius (these values are distorted because of the cell size variation).
2. From the calibration curve of real cell size *versus* calculated size we get the cell radius variation (the standard deviation) (*figure 5*).
3. From the calibration curve of radius percentual deviation for the variation found it the previous step we get the real average radius (*figure 6*).

In this paper, a new method for the determination of size distribution of cellular structures is proposed. This method is not based on the area calculation, but on the determination of fractal parameters of the studied structure. The error of determination of average radius and of the standard deviation is less then 5 % when this method is applied to model data. The error does not exceed 15 % when real data is used.

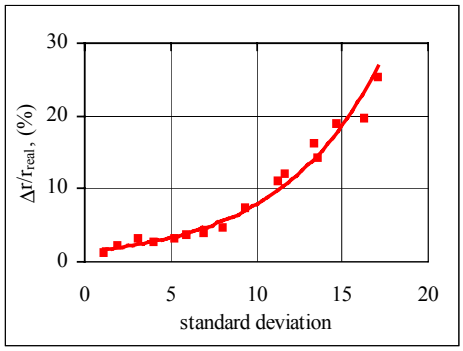

Figure 6: Calibration curve for percentual deviation of cell radius for x = 100, r = 38 pixels

References

1. *Benoit*, Fractal Analysis System, True Soft International (1999)
2. *Lucia*, Image Archiv Plus, Users' guide, Laboratory Imaging, s.r.o., (1999)
3. Fooley J. D., van Dam A., Feiner S. K., Hughes J. F., Phillips J. R.: *Introduction to Computer Graphics*, Addison-Wesley Publishing Company, Reading USA (1997)
4. *HarFA*, Harmonic and Fractal Image Analyser, software for determination of fractal dimension, www.fch.vutbr.cz/lectures/imagesci (2001)

The Use of Fractal Analysis for the Determination of Yeast Cell Diameter

Mária Veselá, Oldřich Zmeškal, Michal Veselý, Martin Nežádal
Brno University of Technology, Faculty of Chemistry
Purkyňova 118, 612 00 Brno
vesela@fch.vutbr.cz, zmeskal@fch.vutbr.cz, vesely-m@fch.vutbr.cz, nezadal@fch.vutbr.cz

The advances in digital image recording techniques and especially the price reductions have made these technologies suitable and available for various techniques of image analysis. These digital techniques are now applicable in those segments of scientific research, where manual processes of image evaluation prevailed until nowadays.

There exist many ways of biological specimen image analysis and they are readily available as complete commercial software products. Anyway, the image analysis is not only applicable to biological and microbiological research. Software application HarFA [4] has been developed at our faculty. Originally, it has been designed for the image analysis of print patterns. This software enables the user to make various correction of the captured image, to apply filters, colour separations and both harmonic and fractal analysis. At the same time, it can be used for the image analysis of biological specimens as well.

The harmonic and fractal analysis of the image or its colour separations belongs to the basic methods for the image analysis. This analysis can be performed by various software equipment, which is commonly available [1], [2], [3]. However, this software is developed for special purposes, and therefore it is not applicable generally. Just this method was used for analysis of microbiological specimens for the determination of diameter distribution of yeast cells in digital image (*figure 1*).

It has been shown that under certain circumstances, HarFA can be used to analyse the image of a microscopic specimen. The circumstances are:

- cells have to be spherical or ellipsoidal,
- cells have to be similar in size,
- cells have to be coloured different from the background.

Under these conditions it is possible to determine the number of cells in the image, their size and the size distribution.

The image was taken by recording equipment, which consists of optical microscope SM-6, digital camera SONY and PC. The microscope magnification, resolution of digital camera gives the connection between image size and studied sample size (100 μm per 514 pixels).

According to the experience from previous work we tried to widen the field of application of this method. During the previous work, it was possible to determine the number and size of cells fairly correctly. The samples contained suitable estimated number of cells (100) of appropriate size (35 pixels). When compared with the standard manual method of counting by *Bürker box,* the error was less than 10 %.

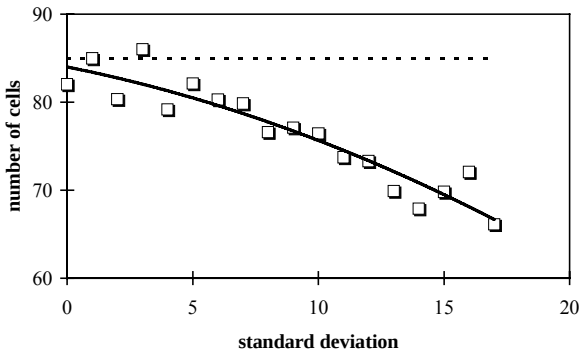

Figure 1: Calibration curve of the cell number

During the analysis of captured image, it is necessary to respect this optimal number and the deviation from correct values determined manually. Our proposed analytical process consists of the following steps:

1. It is necessary to calculate the calibration curve of real number of cells (85 cells were used) versus the number determined by fractal analysis for different distribution. The deviations are caused by just by the size

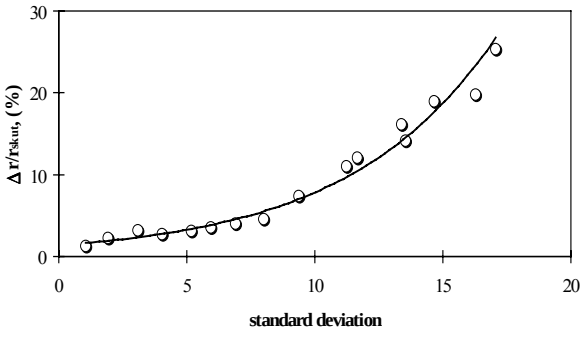

Figure 2: Calibration curve of radius deviation

distribution. This is true also for the deviations between the real radius and the radius determined by fractal analysis (*figure 1* and *2*).

The image analysis is based on:

2. The capturing of the digital image of the specimen (*figure 3*). The image must not contain larger number of cells the number for which the calibration curve was calculated (85). Naturally, the cells have to be easily recognisable.
3. The captured image is cropped so that it contains approximately the number of cells for which the calibration curve was calculated (85 cells, *figure 1*).
4. The image is Gaussian-blurred in order to remove noise, which deteriorates the results of masking.
5. The determination of the optimal colour level for masking. After masking, the image consists only of two colours, so the cells are well separated from the background (*figure 3*).
6. The fractal analysis of the masked image, by which the approximate average radius of the cell is determined.
7. The image is then resampled, so that the approximate cell radius is equal to the radius for which the calibration curve was calculated (35 pixels, *figure 2*).
8. The fractal analysis, by which the number of cells and the average radius are determined (*figure 4*). These values are distorted because of the cell size distribution.
9. The determination of cell size variation from the calibration curve of real number of cells versus the number determined by fractal analysis (*figure 1*).
10. The determination of real average cell radius from the calibration curve of percentual deviation of radius for the variation determined in the previous step (resampled image).
11. The determination of real average radius from the factor of resampling. The results of this analysis are the standard deviation and the average cell radius for the selected cropped image area.

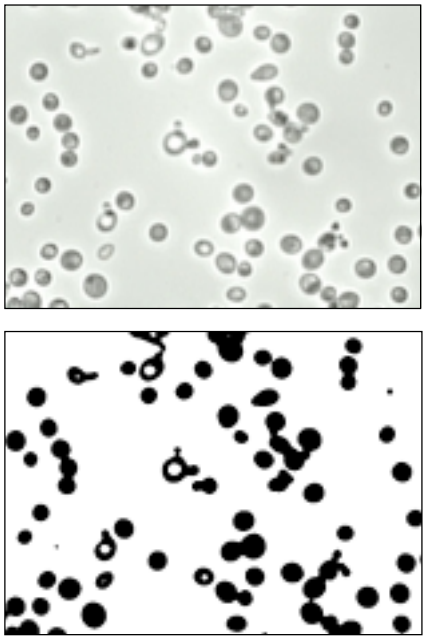

Figure 3: An image of specimen blurred by microscope (top), the same image after processing

The analysed specimen contained 81 cells whose average radius was 3.1 μm and the standard deviation 0.8 μm as determined by standard practice [2]. The following values were determined by the algorithm described above: average radius was 3.3 μm and the standard deviation 0.8 μm. By the evaluation of series of specimen it was determined, that the error of average radius and of standard deviation when compared with standard practice does not exceed 10%, even when the cells are not ideally spherical.

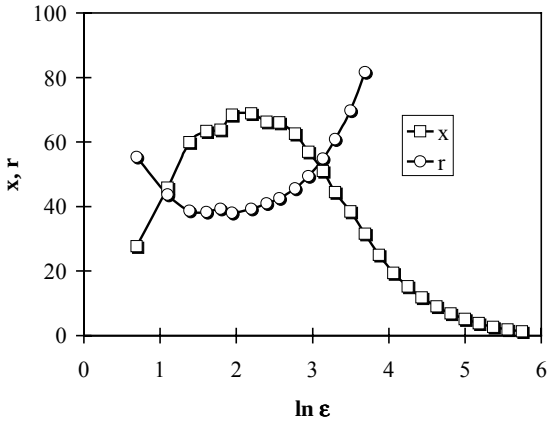

Figure 4: The determination of number and radius of cells

References

1. *Benoit*, Fractal Analysis System, True Soft International (1999)
2. *Lucia*, Image Archiv Plus, Users' guide, Laboratory Imaging, s.r.o., (1999)
3. Fooley J. D., van Dam A., Feiner S. K., Hughes J. F., Phillips J. R.: *Introduction to Computer Graphics*, Addison-Wesley Publishing Company, Reading USA (1997)
4. *HarFA*, Harmonic and Fractal Image Analyser, software for determination of fractal dimension, www.fch.vutbr.cz/lectures/imagesci. (2001)

Fractal Geometry of Modern Art

George Johnson and James Croft
Nottingham University 3rd year undergraduates
ppyugpj@nottingham.ac.uk, ppyujrc@nottingham.ac.uk

Can science be used to understand modern art?

This question triggers reservations from both scientists and artists. However, for the abstract paintings produced by Jackson Pollock in the late 1940s, science proves to be an important tool for determining their fundamental content. Pollock dripped paint from a can on to vast canvases rolled out across the floor of his barn. The Pollock's patterns were found to be chaotic trajectories, i.e. they have fractal geometry.

Figure 1: Jackson Pollock – lavender mist

The present project is about designing a system to generate chaotic trajectories where the degree of chaos can be tuned. The system consists of a pendulum which records its motion by dripping an identical paint trajectory on to a horizontal canvas positioned below. When left to swing on its own, the pendulum follows a predictable, non-chaotic motion. However, by knocking the pendulum at a frequency slightly different from the one at which it naturally swings, the system becomes a kicked oscillator. By tuning the kick, which can be applied using, for example, electromagnetic driving coils, chaotic motion and Pollock-like patterns could be generated.

An initial system using fixed magnets both below the canvas and attached to the pendulum was set up. Some pictures were produced.

The bellow picture (*fig. 2*) was produced when the pendulum was released from the lower right corner of the canvas and allowed to swing until it came to rest.

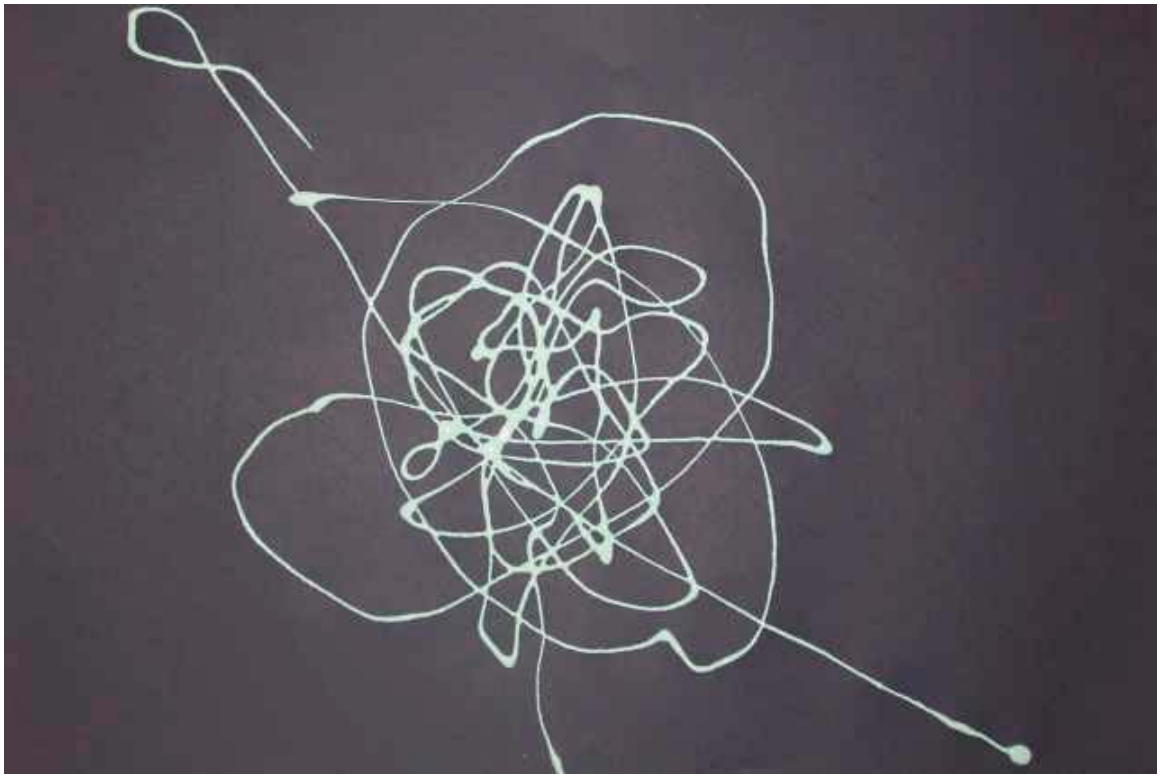

Figure 2

This is a preliminary result and we hope to produce more complex works as we hone the technique.

Having experimented with the demo version of HarFA we wish to use the full version to analyse our paintings and compare fractal dimensions calculated for Jackson Pollock paintings and our own.

The project is due for submission in Jan 2003.

Contact details:

George Johnson ppyugpj@nottingham.ac.uk
James Croft ppyujrc@nottingham.ac.uk

The Fractal approach as a tool to understand asymptomatic Brain hyperintense MRI Signals in Divers

Costantino Balestra [1,2,4], Peter Germonpré [1,3], Alessandro Marroni [1], Brigitte Farkas [1,5], Philippe Peetrons [5], Frédéric Vanderschueren [1], Emilie Duboc[1,2,4], Thyl Snoeck [1,2,4]

[1] DAN Europe Research Division [2] Université Libre de Bruxelles I.S.E.P.K. Bruxelles, Belgium. [3] Center for Hyperbaric Oxygen Therapy, Military Hospital Queen Astrid, Brussels, Belgium; [4] Department of General Human Biology, Haute Ecole Paul Henri Spaak, Brussels, Belgium. [5] Radilogy service , Hôpital Molière Longchamps (Brussels), Belgium
balestra@daneurope.org

1. Introduction

Since 1989 the first publication that spoke about the possible correlation between the presence of a Patent Foramen Ovale and the occurrence of decompression sickness (Moon *et al.*, 1989) there has been no respite in the quest about the possibility of such a relationship. Since 1996 the research department of DAN Europe set out to investigate and respond to a serious concern at the time as a result of this alarming article: is there really an increased risk of DCS for a diver who has PFO? (Wilmshurst *et al.*, 1986; Wilmshurst *et al.*, 1995; Knauth *et al.*, 1997).

The decompression bubbles are found primarily in the veins; in the heart they are mainly found in the superior and inferior vena cava. Frequently, divers regard PFO as a hole that allows the continual passage between the right atrium and the left - the arterial part of the heart where we don't want to see bubbles (see the illustration). The flow coming from superior vena cava has to pass over a fold, providently given by Nature before touching the PFO (or the Fossa Ovalis).

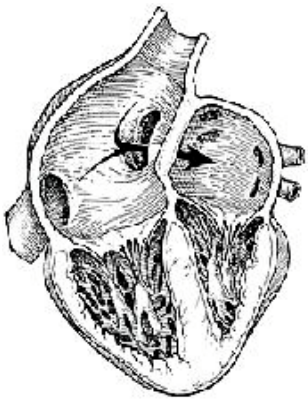

This causes a sudden increase in the rate of the flow, which meets the flow coming from the inferior vena cava and thus turbulence is caused which causes the bubbles to be TAKEN AWAY from the interatrial septum. Therefore if we understand correctly, the bubbles would not cross the Foramen Ovale in natural conditions. But then why the injections of bubbles that are made during the transesophageal echocardiogram to measure the PFO, since they pass in the left atrium?

The reason is that respiratory movements are made to reverse the intracardiac flow caused by variations in the intrathoracic pressure.

2. Spots on the brain and PFO

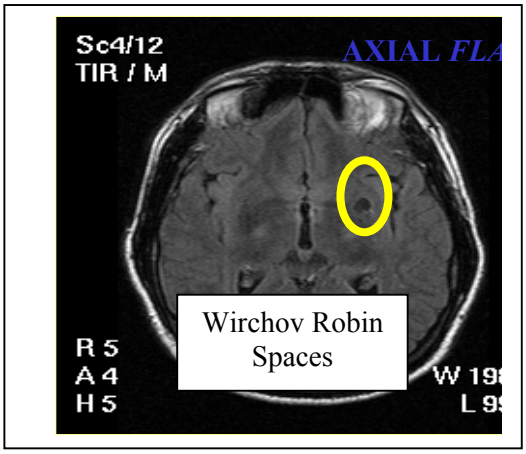

A number of years ago some studies declared the relationship between PFO and cerebral "LESIONS" (Reul *et al.*, 1995) (Knauth *et al.*, 1997). Since then others have found that there was not a direct relationship(Gerriets *et al.*, 2000; Saary & Gray, 2001). In all of these studies, however, we encounter the same population bias. DAN therefore asked two groups of people to sit a test of nuclear magnetic cerebral resonance imaging; 50 were divers and 50 were non-divers. All of the participants had to be under 41 years old because according to studies spontaneous lesions cerebral can occur after 45 years. The distinguishing feature was that this population was randomised; we asked 400 volunteers: 200 divers and 20 non-divers. We asked the divers to declare that they had never suffered from DCS. However, often certain accidents and cerebral incidences in particular were not declared because of benign or brief symptoms.

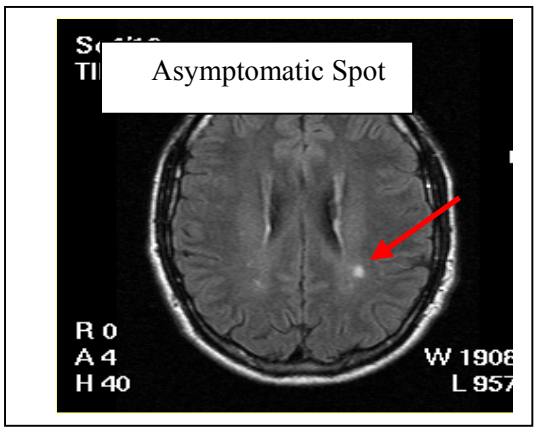

How many divers had have felt a little dazed after a dive ...which goes away after a few minutes ... a case of badly equalised ears or a transient cerebral bubble?

To avoid this situation of poor choice of population we took the case of 1 diver in 4.

Then we made a comparison between the numbers and the size of the "spots" found among the divers and those found among the divers and non-divers.

A little more spots were detected among the divers but there was not significantly more. This is contrary to what some authors say with populations that are not randomised and without a control group. Also, to ensure accuracy in the results a particular imaging filter, which allows a reliable diagnosis of the FLAIR sequence to be made, was used. Another pitfall that was present was the possibility of finding naturally lacunar zones known as the Wirchow-Robin spaces and diagnosing them as "LESIONS".

The use of fractal analysis is a known technique in clinical science and particularly in pathology (Rossitti, 1995; Sisodiya *et al.*, 1995; Cross, 1997a; Caldwell *et al.*, 1998; Handels *et al.*, 1998; Luzi *et al.*, 1999) , the interesting predictive opportunity of fractal analysis in breast cancer (Byng *et al.*, 1996a; Byng *et al.*, 1996b; Velanovich, 1998; Heymans *et al.*, 1999; Zheng & Chan, 2001) or osteoporosis (Feltrin *et al.*, 2001; Dougherty & Henebry, 2002; Lespessailles *et al.*, 2002; Libouban *et al.*, 2002) is related in pattern differentiation on the medical diagnostic images.

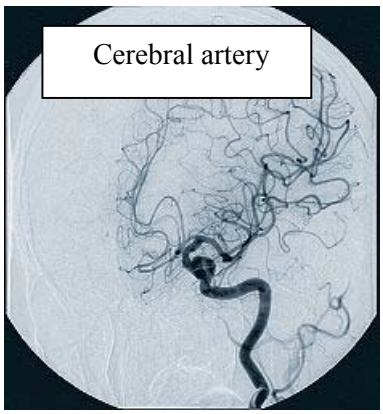

The important possibility of diagnosis before the rise of real objective or clinical symptom is a paramount of interest in the medical field. The precise use of fractal analysis in neuroimaging is a moving field with a very promising future. The study of with matter hyperintense signal has been analyzed with the fractal approach in geriatric patients to see if some links can be considered with the white matter hyperintense "spots" and the epileptic seizures (Takahashi *et al.*, 2001) .

In the young patient, to our knowledge, nothing has been done yet in order to investigate some relations between the significant difference of the fractal dimension of some hyperintense white matter spots in the brain and their spatial distribution.

We tried to use the self-similarity concept of the fractals as this has already been used to mark differences between architectural (Cross, 1997b; Chen & Chen, 1998; Behar, 2001) or even cancerous structures (Peiss *et al.*, 1996).

Our aim was to verify if the fractal dimension of some cerebral vascularization images was compatible with the Fractal Dimension of the a symptomatic brain Spots in divers who never experienced a decompression disease nor PFO related headache (Anzola *et al.*, 1999; Wahl *et al.*, 2001; Sztajzel *et al.*, 2002). All these criteria were included in the population selection criteria.

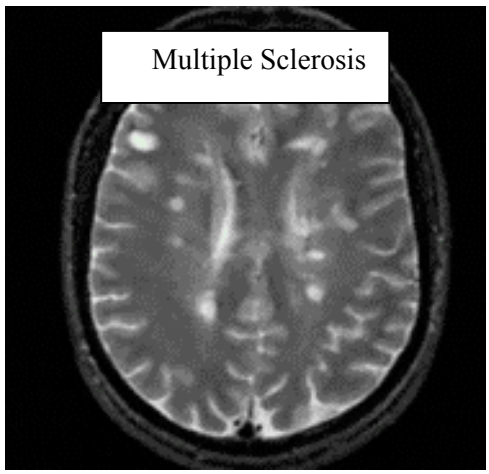

To calculate the fractal dimension of the images we used the Harfa 4.0 program applying the box counting method after appropriated filtering and thresholding and accepting the final result as the fractal dimension the better occurrence of the slope described in the slope analysis option.

3. Methods

Our population was a group of 50 healthy divers (scuba divers) not older then 40 yr. This population has been randomized from a larger population of 200 voluntary divers, which has been drastically selected by very strict criteria: less than 41 yr old; at least 200 dives; no history of cardiovascular or decompression disease and other conditions such as multiple sclerosis or headache brain lesions.

The randomization has been performed to exclude some population bias that can occur in such a voluntary based selection process.

We tried to compare the fractal dimension of some clearly non-vascular spots in the white cerebral matter and the dimension of some other spots from other origin.

The purpose was to determine weather the "lesion like" spots could be associated with the circulating arterial bubbles coming up to the brain from the patent cardiac Foramen Ovale or just another unexplained or non diving dependent mechanism.

Furthermore to investigate the potential difference of the spatial distribution between the fractal dimension ischemic lesions of the cerebral vascular accident and the haemorragic ones we separated them and controlled exclusively the clearly ischemic ones.

If the "lesions like asymptomatic spots" were from vascular origin, their spatial distribution should be compatible either with the cerebral vascular images or the ischaemic lesions fractal dimension.

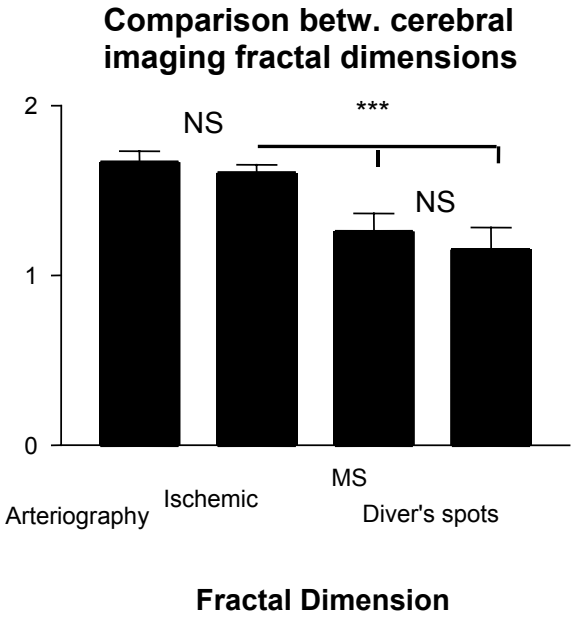

4. Results

We could find in our population of 50 asymptomatic divers (randomized out of 200; 1 excluded for MS) 4 lesion like white matter hyperintense spots. Then we compare the fractal dimensions of 18 brain angiographies; 9 images of Multiple Sclerosis; 5 Ischemic vascular brain lesions images. (see graph.)

The Anova statistical test was performed after testing the normality of the population and the posttest performed was the Neuman-Keuls discriminate test.

The differences between all the vascular depending images fractal dimension and the "diver's sports" were highly significant ($p<0.001$), conversely the differences between the vascular bed spatial distribution and the ischemic lesions images was not statistically different. This allows us to be sure that the fractal dimension is a good tool to be used in our experimental paradigm.

The non-vascular brain lesion fractal dimension was not statistically different of the "diver's spots" one, thus our assumption was to postulate that those spots are not clearly to be defined likes vascular related ischemic lesions as generally admitted.

5. Conclusions

The fractal analysis of cerebral images is good tools to determine weather the spatial distribution is compatible with the vascular bed and allow us to postulate another non vascular mechanism. Moreover the link between the patency of the Foramen Ovale of the heart and the diver's "brain spots" seem not to be as clear as it has been postulated. (Knauth *et al.*, 1997; Schwerzmann & Seiler, 2001)

Correspondent : balestra@daneurope.org

6. References

1. ANZOLA, G. P., MAGONI, M., GUINDANI, M., ROZZINI, L. & DALLA VOLTA, G. (1999). Potential source of cerebral embolism in migraine with aura: a transcranial Doppler study. *Neurology* **52,** 1622-1625.

2. BEHAR, T. N. (2001). Analysis of fractal dimension of O2A glial cells differentiating in vitro. *Methods* **24,** 331-339.

3. BYNG, J. W., BOYD, N. F., FISHELL, E., JONG, R. A. & YAFFE, M. J. (1996a). Automated analysis of mammographic densities. *Phys Med Biol* **41,** 909-923.

4. BYNG, J. W., BOYD, N. F., LITTLE, L., LOCKWOOD, G., FISHELL, E., JONG, R. A. & YAFFE, M. J. (1996b). Symmetry of projection in the quantitative analysis of mammographic images. *Eur J Cancer Prev* **5,** 319-327.

5. CALDWELL, C. B., MORAN, E. L. & BOGOCH, E. R. (1998). Fractal dimension as a measure of altered trabecular bone in experimental inflammatory arthritis. *J Bone Miner Res* **13,** 978-985.

6. CHEN, S. K. & CHEN, C. M. (1998). The effects of projection geometry and trabecular texture on estimated fractal dimensions in two alveolar bone models. *Dentomaxillofac Radiol* **27,** 270-274.

7. CROSS, S., S. (1997a). Fractals in Pathology. *Journal of Pathology* **182,** 1-8.

8. CROSS, S. S. (1997b). Fractals in pathology. *J Pathol* **182,** 1-8.

9. DOUGHERTY, G. & HENEBRY, G. M. (2002). Lacunarity analysis of spatial pattern in CT images of vertebral trabecular bone for assessing osteoporosis. *Med Eng Phys* **24,** 129-138.

10. FELTRIN, G. P., MACCHI, V., SACCAVINI, C., TOSI, E., DUS, C., FASSINA, A., PARENTI, A. & DE CARO, R. (2001). Fractal analysis of lumbar vertebral cancellous bone architecture. *Clin Anat* **14,** 414-417.

11. GERRIETS, T., TETZLAFF, K., LICENI, T., SCHAFER, C., ROSENGARTEN, B., KOPISKE, G., ALGERMISSEN, C., STRUCK, N. & KAPS, M. (2000). Arteriovenous bubbles following cold water sport dives: Relation to right-to-left shunting. *Neurology* **55,** 1741-1743.

12. HANDELS, H., ROSS, T., KREUSCH, J., WOLFF, H. H. & POPPL, S. J. (1998). Image analysis and pattern recognition for computer supported skin tumor diagnosis. *Medinfo* **9 Pt 2,** 1056-1062.

13. HEYMANS, O., BLACHER, S., BROUERS, F. & PIERARD, G. E. (1999). Fractal quantification of the microvasculature heterogeneity in cutaneous melanoma. *Dermatology* **198,** 212-217.

14. KNAUTH, M., RIES, S., POHIMANN, S., KERBY, T., FORSTING, M., DAFFERTSHOFER, M., HENNERICI, M. & SARTOR, K. (1997). Cohort study of multiple brain lesions in sport divers: role of a patent foramen ovale. *Bmj* **314,** 701-705.

15. LESPESSAILLES, E., POUPON, S., NIAMANE, R., LOISEAU-PERES, S., DEROMMELAERE, G., HARBA, R., COURTEIX, D. & BENHAMOU, C. L. (2002). Fractal analysis of trabecular bone texture on calcaneus radiographs: effects of age, time since menopause and hormone replacement therapy. *Osteoporos Int* **13,** 366-372.

16. LIBOUBAN, H., MOREAU, M. F., LEGRAND, E., AUDRAN, M., BASLE, M. F. & CHAPPARD, D. (2002). Comparison of histomorphometric descriptors of bone architecture with dual-energy X-ray absorptiometry for assessing bone loss in the orchidectomized rat. *Osteoporos Int* **13,** 422-428.

17. LUZI, P., BIANCIARDI, G., MIRACCO, C., DE SANTI, M. M., DEL VECCHIO, M. T., ALIA, L. & TOSI, P. (1999). Fractal analysis in human pathology. *Ann N Y Acad Sci* **879,** 255-257.

18. MOON, R. E., CAMPORESI, E. M. & KISSLO, J. A. (1989). Patent foramen ovale and decompression sickness in divers. *Lancet* **1,** 513-514.

19. PEISS, J., VERLANDE, M., AMELING, W. & GUNTHER, R. W. (1996). Classification of lung tumors on chest radiographs by fractal texture analysis. *Invest Radiol* **31,** 625-629.

20. REUL, J., WEIS, J., JUNG, A., WILLMES, K. & THRON, A. (1995). Central nervous system lesions and cervical disc herniations in amateur divers. *Lancet* **345,** 1403-1405.

21. ROSSITTI, S. (1995). Energetic and spatial constraints of arterial networks. *Arq Neuropsiquiatr* **53,** 333-341.

22. SAARY, M. J. & GRAY, G. W. (2001). A review of the relationship between patent foramen ovale and type II decompression sickness. *Aviat Space Environ Med* **72,** 1113-1120.

23. SCHWERZMANN, M. & SEILER, C. (2001). Recreational scuba diving, patent foramen ovale and their associated risks. *Swiss Med Wkly* **131,** 365-374.

24. SISODIYA, S. M., FREE, S. L., FISH, D. R. & SHORVON, S. D. (1995). Increasing the yield from volumetric MRI in patients with epilepsy. *Magn Reson Imaging* **13,** 1147-1152.

25. SZTAJZEL, R., GENOUD, D., ROTH, S., MERMILLOD, B. & LE FLOCH-ROHR, J. (2002). Patent foramen ovale, a possible cause of symptomatic migraine: a study of 74 patients with acute ischemic stroke. *Cerebrovasc Dis* **13,** 102-106.

26. TAKAHASHI, T., MURATA, T., OMORI, M., KIMURA, H., KADO, H., KOSAKA, H., TAKAHASHI, K., ITOH, H. & WADA, Y. (2001). Quantitative evaluation of magnetic resonance imaging of deep white matter hyperintensity in geriatric patients by multifractal analysis. *Neurosci Lett* **314,** 143-146.

27. VELANOVICH, V. (1998). Fractal analysis of mammographic lesions: a prospective, blinded trial. *Breast Cancer Res Treat* **49,** 245-249.

28. WAHL, A., WINDECKER, S. & MEIER, B. (2001). Patent foramen ovale: pathophysiology and therapeutic options in symptomatic patients. *Minerva Cardioangiol* **49,** 403-411.

29. WILMSHURST, P., EDGE, C. J. & BRYSON, P. (1995). Long-term adverse effects of scuba diving. *Lancet* **346,** 384.

30. WILMSHURST, P. T., ELLIS, B. G. & JENKINS, B. S. (1986). Paradoxical gas embolism in a scuba diver with an atrial septal defect. *Br Med J (Clin Res Ed)* **293,** 1277.

31. ZHENG, L. & CHAN, A. K. (2001). An artificial intelligent algorithm for tumor detection in screening mammogram. *IEEE Trans Med Imaging* **20,** 559-567.

Fractal geometry for the characterisation of urban-related states: Greater Montreal Case

Catherine Morency and Robert Chapleau (rchapleau@polymtl.ca)
École Polytechnique de Montréal, Civil Engineering Department, CANADA
Transportation planning
www.transport.polymtl.ca

This paper summarises a brief experimentation of fractal geometry applied to the characterisation of urban-related states in the Greater Montreal Area (GMA). Research in the field of travel behaviour and urban modelling can be classified according to four basic axes of concern: the measure of urban mobility, the assessment of urban land use, the monitoring of demographic and economic forces and the appraisal of the role of the transportation networks. Fractal measures, used in conjunction with other measures, could lead to renewed description of several issues related to those axes of concern. As an introduction, methods for computing fractal measures were experimented in order to assist in the description of the land and transportation network coverage, as well as in the study of the dynamics of settlements over the area.

1. Methods for computing fractal dimensions

Two methods were used in order to estimate the fractal dimension of the urban states: the box-counting method as implemented in *Harfa* and the mass-radius method computed within a GIS environment. Results from both methods are presented.

1.1. Box-counting method

This method computes the number of cells required to entirely cover an object, with grids of cells of varying size. Practically, this is performed by superimposing regular grids over an object and by counting the number of occupied cells. The logarithm of N(r), the number of occupied cells, versus the logarithm of 1/r, where r is the size of one cell, gives a line whose gradient corresponds to the box dimension. A refinement of this method is implemented in *Harfa* where a distinction between completely occupied cells and partially occupied cells is introduced. This allows the computation of several box dimensions by plotting the logarithm of combination of cells: completely occupied, completely non-occupied, partially-occupied.

Box-counting method relies on digitized representations of the objects of interest and will be affected by their resolution. It is also sensible to the orientation of the grid as well as to its initial placement. In addition, treatment of phenomenon involving intensities (number of dwellings per enumeration areas) will require special processing such as the use of graduated symbols arbitrarily specified.

1.2. Mass-radius method

The mass dimension defines the relationship between the area located within a certain radius and the size of this radius (or box). This is performed for various radiuses as well as from various points of origin. The mass dimension can be estimated from the log-log plot of the area as a function of the radius.

In our case, the center of mass of the territory is computed and serves as origin point. The area located within a growing radius (1 to 62 km) is estimated using GIS capabilities. Moreover, urban phenomena such as population dispersion or transit share are often examined as a function of distance to CBD (Central Business District). In this view, mass dimension is also computed in reference to this point.

2. Demonstration

Fractal geometry will be experimented to characterise the morphology of the Greater Montreal Area (5 390 sq. km.) and of the spatial extent of the transportation network (1 927 sq. km.). Data from the 1996 Canadian census will also be used to illustrate the dynamics of settlements construction over the territory. Those data are disseminated at the enumeration area (EA) level (app. 250 households/EA and more than 4 500 EA in the GMA) and construction information is available for six periods: before 1946, 1946-1960, 1961-1970, 1971-1980, 1981-1990 and 1991-1996.

2.1. The Greater Montreal Area

Box counting dimension was computed over a black and white representation of the area (948 X 891 pixels), hence no threshold operation was necessary. Dimension obtained while considering both completely and partially occupied cells is 1.8583.

Mass dimension was computed using both GIS and spreadsheet functions. Results from considered origins, mass centre and central business district, are presented in *Figure 1*.

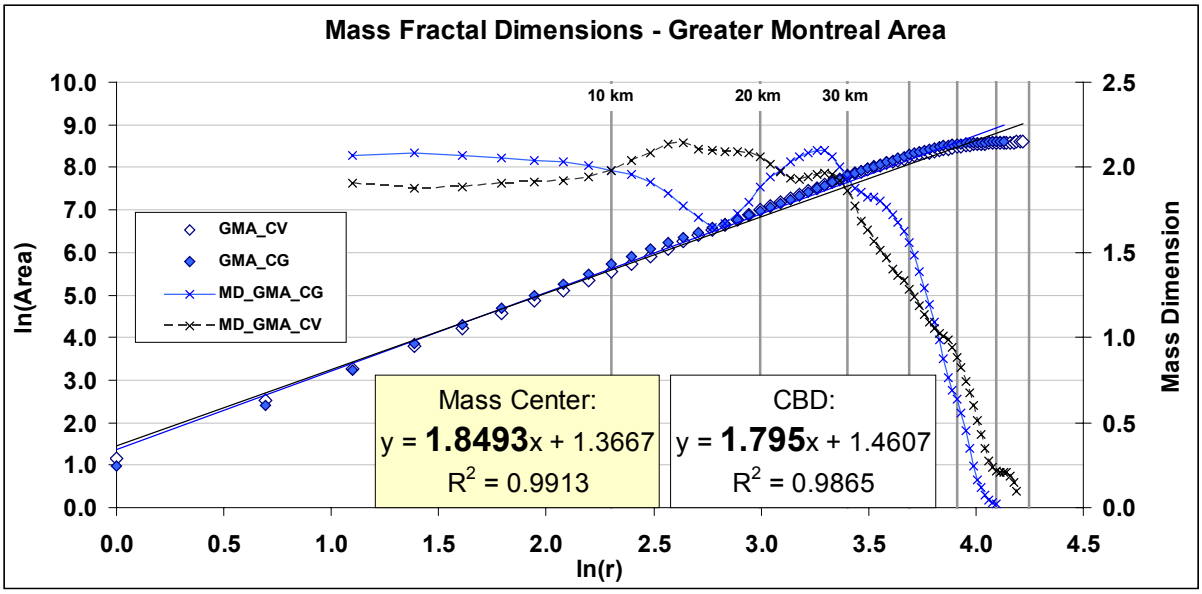

Figure 1 - Mass dimensions for Greater Montreal Area - from mass centre and central business district

The mass dimension computed from the Mass Centre, 1.8493, approaches the one measured with the box-counting method. These plot however reveals a non-linear relation between the area and the radius, especially over 30 kilometres. The fluctuation of the mass dimension can be appreciated with the rough estimation of the slope with successive data pairs; it severely drops over 30 kilometres, the radius of gyration.

The two following figures illustrate the superimposition of radiuses from mass centre and CBD.

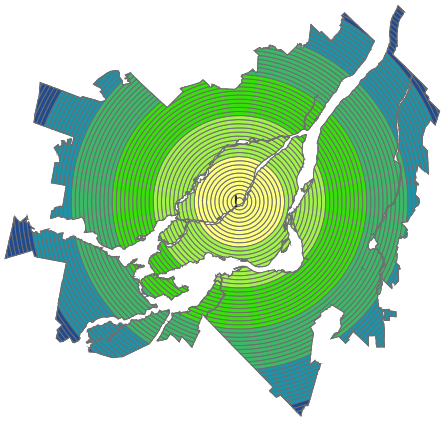

Figure 2 - 1 kilometre radius from Mass Center

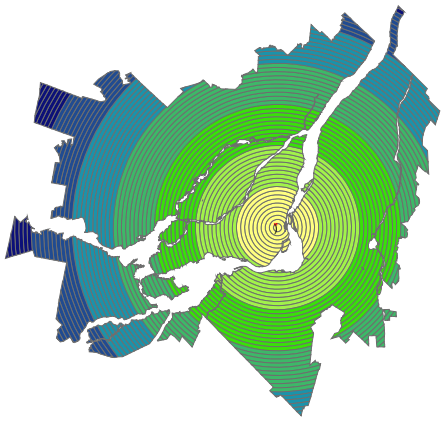

Figure 3 - 1 kilometre radius from CBD

2.2. The transportation network

A similar approach was used in order to estimate the fractal dimension of the surface covered by the transportation network. A 100 metres buffer applied over the entire network approximates this surface. The dimension and resolution of the digitised representation were maintained identical to the one used for GMA estimations (and will be preserved for the study of settlements construction).

The box-counting dimension obtained while considering both completely and partially occupied cells is 1.7392, which appears consistent with the previous results.

The computation of mass dimensions with the selected origins is synthesised in *Figure 4*. Again, the plot reveals a non-linear relation between the area and the radius that is less adequately modelled by a linear regression. The curve representing the fluctuation of the mass dimension is declining, affected by the dedensification of the network towards the suburbs.

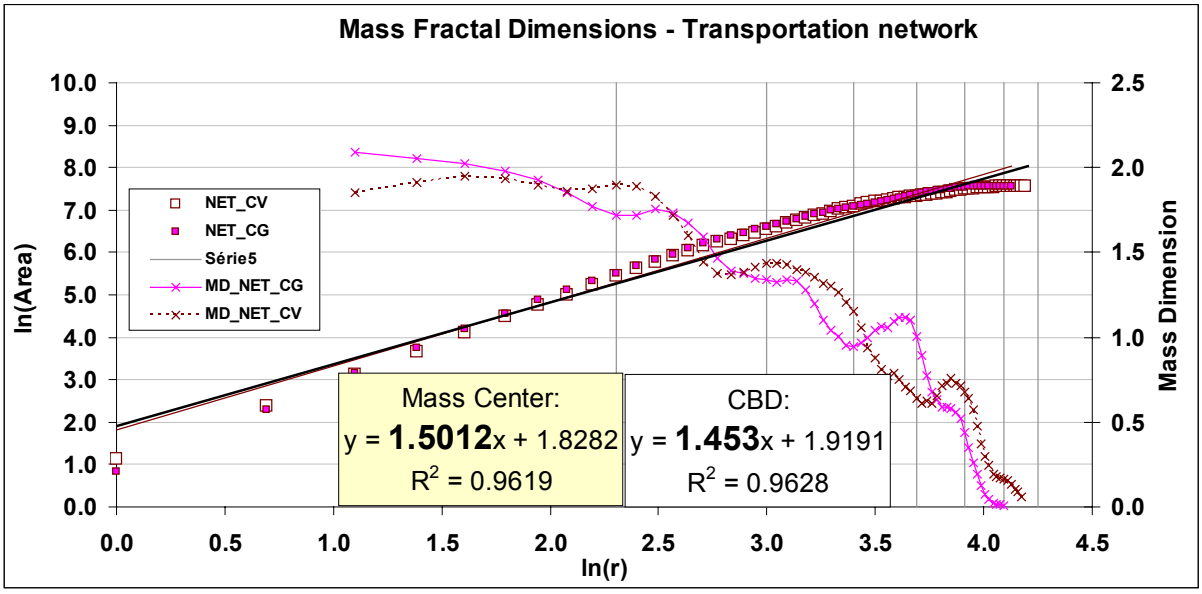

Figure 4 – Mass dimensions for the Transportation Network - from mass center and central business district

2.3. The dynamics of settlements patterns

Our final experimentation deals with dwellings' construction data from the 1996 Canadian census. Information are available for six periods of construction (number of dwellings constructed in every period) and are disseminated at the enumeration area (EA) level, one EA containing data for approximately 250 households. Since data are aggregated and spatially located according to centroids (app. 4500 to cover the GMA), it was decided to use graduated symbols for the consideration of intensities, that is the number of dwellings constructed at a specified period at every location. This processing, arbitrary for the moment, allowed the estimation of box-counting dimensions at six different stages of residential development. The results are summarised below.

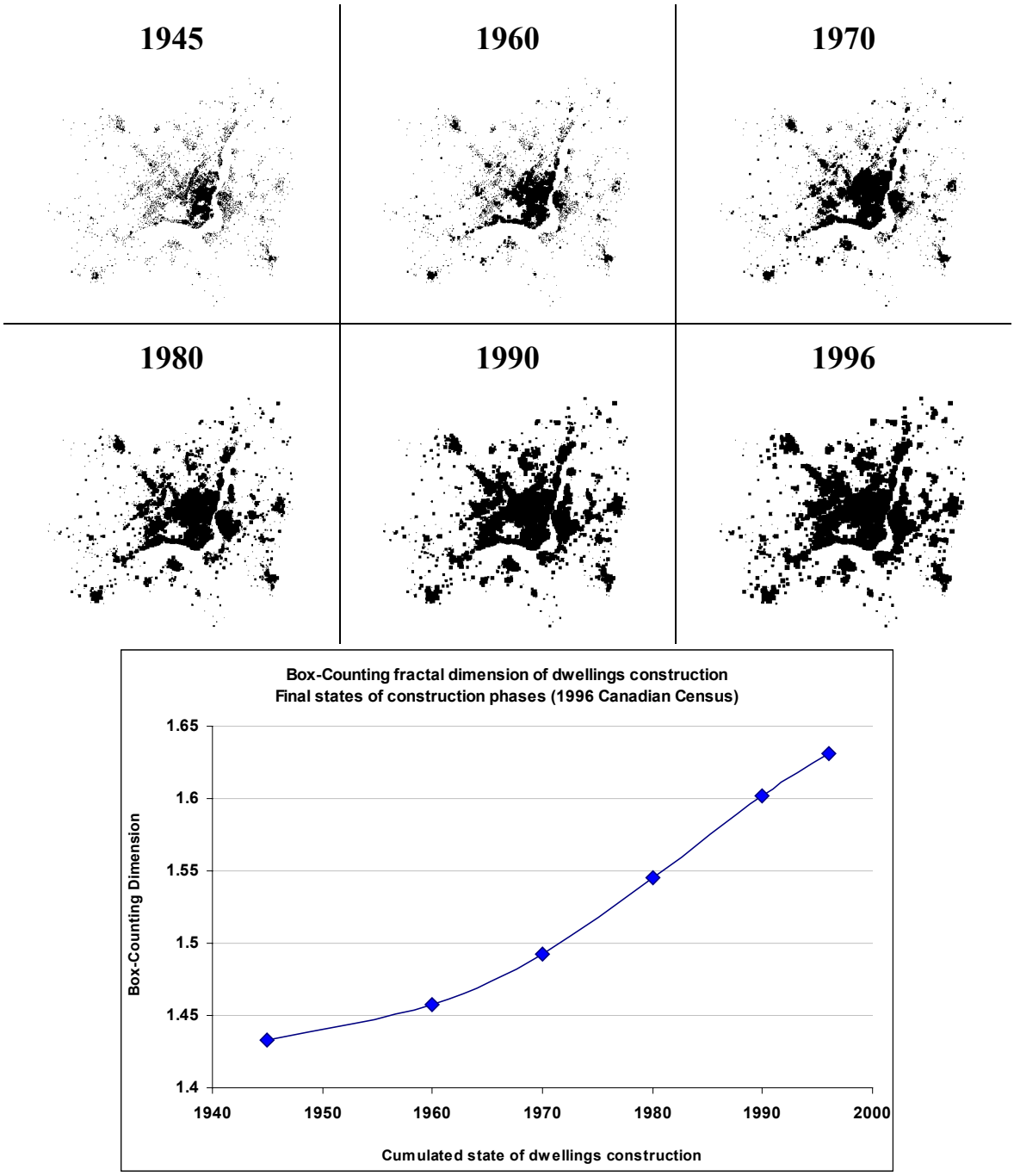

Figure 5 - Evolution of the box-counting dimension of residential construction over the GMA

3. Conclusion

At this stage, only computation feasibility was experimented over urban-related data. Interpretation of the fractal dimensions as well as demonstration of relevance/irrelevance for the modelling of transport modelling issues needs further experimentation.

4. Literature

Fractal geometry:

1. FRANKHAUSER, P., GENRE-GRANDPIERRE, C. (1998). La géométrie fractale – un nouvel outil pour évaluer le rôle de la morphologie des réseaux de transport public dans l'organisation spatiale des organisations, *les Cahiers Scientifiques du Transport* No 33, pages 41-78.
2. HARFA, Harmonic and Fractal Image Analyser, Software for the Determination of Fractal Dimension, www.fch.vutbr.cz/lectures/imagesci

3. KENKEL, N., WALKER, D.J. (1996) Fractals in the biological sciences, http://www.umanitoba.ca/faculties/science/botany/labs/ecology/fractals/fractal.html

Travel behaviour and socio-demographic trends:

1. CHAPLEAU, Robert (1991). Socio-Démographie Suburbaine et Transport Urbain: Tendances Récentes, *6th International Association of Travel Behaviour*, Québec, Tome 2, pages 175-190.
2. CHAPLEAU, Robert (1998). Free-wheeling urban mobility: a question of densities, motorization, employment and transit decline,*World Conference on Transportation Research*, Anvers, Belgique.
3. CHAPLEAU, Robert, MORENCY, Catherine (1999). How urban sprawl affects mobility market, *34e congrès de l'Association québécoise du transport et des routes*, Montréal.
4. CHAPLEAU, Robert, MORENCY, Catherine (2001). Impacts of settlement patterns and dynamics on urban mobility behavior: findings from the combination of multiple data sources, *World Conference on Transportation Research*, July 2001, Séoul, Corée, CD-ROM.
5. MORENCY, Catherine, CHAPLEAU, Robert (2002). Implications of Settlement Patterns on Travel Behaviours: A Totally Disaggregate Empirical Study in the Greater Montreal Area, *Compte-rendus de la 30e conférence annuelle de la Société canadienne de génie civil*, Montréal, pages 263-272.

Publications by our research group can be obtained through the following web site: http://www.sti.polymtl.ca/articles/titre.asp

Influence of GSM Microwaves on Fractal Structure of brain tumours

M. Babincová[1], P. Sourivong[2], D. Leszczynska[3], and P. Babinec[1]

[1]Department of Biophysics and Chemical Physics, Comenius University, Mlynská dolina F1, 842 48 Bratislava, Slovakia
email: babincova@fmph.uniba.sk

[2]U.S. Army Center for Health Promotion and Preventive Medicine (USACHPPM), Health Physics Program, 5158 Blackhawk Road, Aberdeen Proving Ground, MD 21010-5402, USA

[3]Department of Civil Engineering, FAMU-FSU College of Engineering, Tallahassee, FL 32310, USA

Abstract

Fractal dimension of C-6 rat glioma tumours growing in microwave field generated by signal simulation of the Global System for Mobile communications (GSM) with frequency 960 MHz was found significantly enhanced as compared with field free tumours growing at different temperatures.

1. Introduction

The Mandelbrot answer to Richardson question: "How long is the coastline of Britain ?" was concept of fractals [1]. Similar answer may be given to the question: "How long is the borderline of tumour ?", as has been found in the works of Sedivy, Landini and Rippin, Waliszewski, and several others [2-4]. In all these studies was emphasized the usefulness of fractal parameters in tumour pathology. The fractal dimension of a tumour could be understood as a measure of irregularity, which serves as an additional morphometric parameter in surgical pathology and is specific for a given tumour. Many epidemiological studies have implicated environmental and residential exposure to electromagnetic field as a possible factor in the development of certain human cancers [5-7]. Extremely low frequency electromagnetic radiation has been reported to affect a wide range of basic cellular functions, including cell proliferation [8] gene transcription and expression [9] on transport [10], protein kinase C activation [11] and cell morphology [12]. Although the detailed mechanism of the influence of a weak electromagnetic field on cellular processes is still unknown [13], electrostimulation of the proliferation of *Saccharomyces cerevisiae* [14] or *Pseudomonas stutzeri* [15], in a weak low frequency field have already direct biotechnological implications.

Recently media attention has focused on claims for damages due to alleged brain tumours, in particular glioblastomas, caused by mobile phone usage. The aim of the present communication is to study the influence of a weak AC magnetic field on rat C6 glioma cell line growing in monolayer. Glioblastomas are high-grade malignant neuroepithelial tumours having a median survival time of 8 months. These tumours have such a grim outcome in part due to their rapid volumetric growth, but also because the tumour has already grossly invaded the surrounding brain tissue long before it can be diagnosed.

As has been recently shown [16] this brain tumour model has super-rough fractal contour and therefore tumour growth may be more susceptible to external influences than ordinary three-dimensional tumours. Moreover tumour interface speed growth is in this two-dimensional case linear and not exponential [17,18] and may be characterized by one-parameter. During tumour growth and evolution, mutations continue and cells behave differently from the normal cells of the tissue where they appeared. In advanced stages of cancer, cells start to detach from the tumour and invade the blood stream or lymphatic system. They can be carried to other body parts producing new metastatic tumours. The detachment and invasion of other tissues result in part from the incorrect expression of adhesion molecules on the cell surface for the mutated genome. This process causes a decrease in cellular adhesion between cells with additional consequences such as an increase in mobility of the cells on the surface of the tumour. As a result, the boundaries of the tumour become very irregular.

This change on tumour morphology, associated with additional information, help physicians to diagnose cancer stage of development. Recent studies indicate that the fractal dimension of tumours is useful as an indicative of malignancy.

2. Material and methods

2.1. Exposure system

The microwave field was generated by signal simulation of the Global System for Mobile communications (GSM), a 960 MHz carrier amplitude modulated with a 217 Hz square pulse of duty cycle 12 %. The experimental apparatus consisted of a pair of horizontal rectangular (25cm x 15cm) coils, maintained in a pseudo-Helmholtz configuration (distance between the coils was 15cm) and powered by AC generator. Field intensities were measured using a Hall effect probe magnetometer (FW Bell, Model 9640). The cell cultures were placed in the middle part between the coils and were exposed to magnetic field and cells were allowed to grow for another 24 hours in field free box. The whole system was placed in at thermostatic box kept at 37.0 ± 0.1 °C. The temperature of the culture medium was monitored by using a nonabsorbing fluoroptic thermometry system (Luxtron 3000, Mountain View, CA, USA) and no relevant heating of medium was observed during the experiments.

2.2. Cell culture

10^4 dissociated C6 glioblastoma cells, cloned originally from rat glioma [19] and obtained from The American Type Culture Collection (Rockville, MD, USA), were plated in a 5 µl of Dulbecco's modified Eagle's medium containing 10 % (v/v) horse serum and 2.5 % (v/v) fetal-calf serum on 35 mm Petri dishes. After cells attachment 2 µl of medium was added to growing culture, which allowed tumours to grow mainly on plate surface. In a regular time intervals control and exposed tumours were photographed under the inverted microscope with a coupled digital photocamera (*Figure 1*).

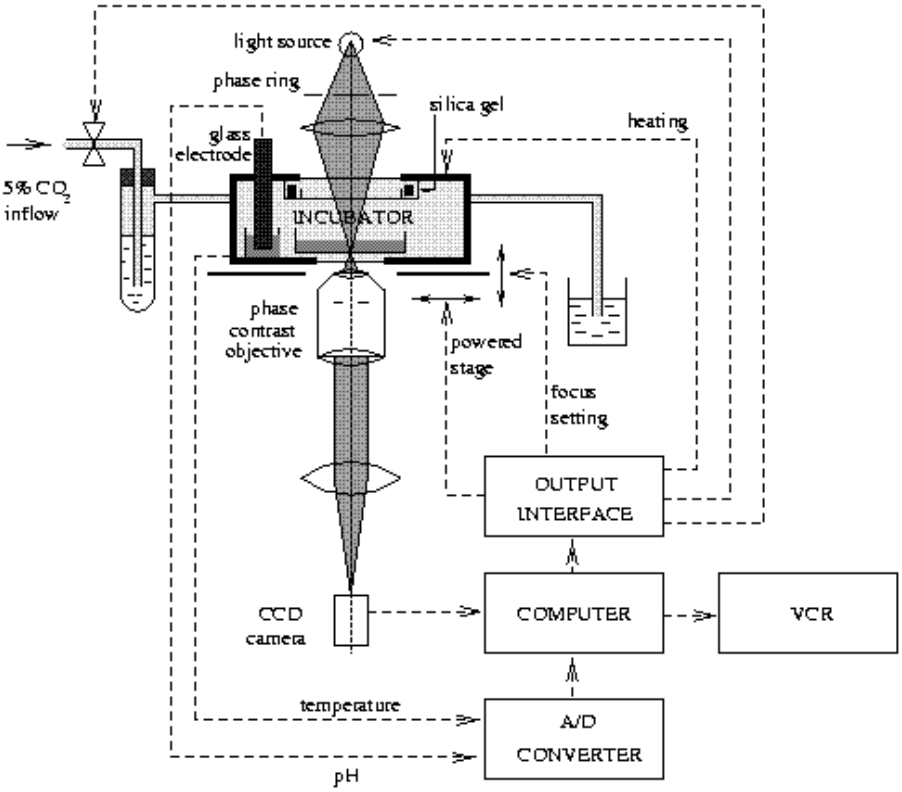

Fig. 1 Experimental setup for the study of two-dimensional tumour growth.

2.3. Determination of fractal dimension

The photographs were analyzed in a computer and tumour images were analyzed using program HarFA [20] based on the improved box counting method where binary images of tumours were covered with different grids (box length ε), and the number of boxes $N(\varepsilon)$ required to cover the structures of the nuclei was recorded. If an object is fractal, $N(\varepsilon)$ increases according to the relation

$$N(\varepsilon) = C\,\varepsilon^{D}$$

where D is fractal dimension and C is constant. From this equation the fractal dimension can be obtained as

$$D = \lim_{\varepsilon \to 0}\{-\log[N(\varepsilon)]/\log(\varepsilon)\}\,.$$

2.4. Statistical analysis

Statistical evaluation of the exponential data was performed with two-tailed Student's t-test with $p<0.05$ as the minimum level of significance.

3. Results and discussion

Fractal dimensions of tumour boundaries are shown in *Figure 2*. For the comparison we have determined fractal dimension of tumours growing at 37 °C (control), tumours growing in microwave field (GSM) and tumours growing at temperature 40 °C (heat).

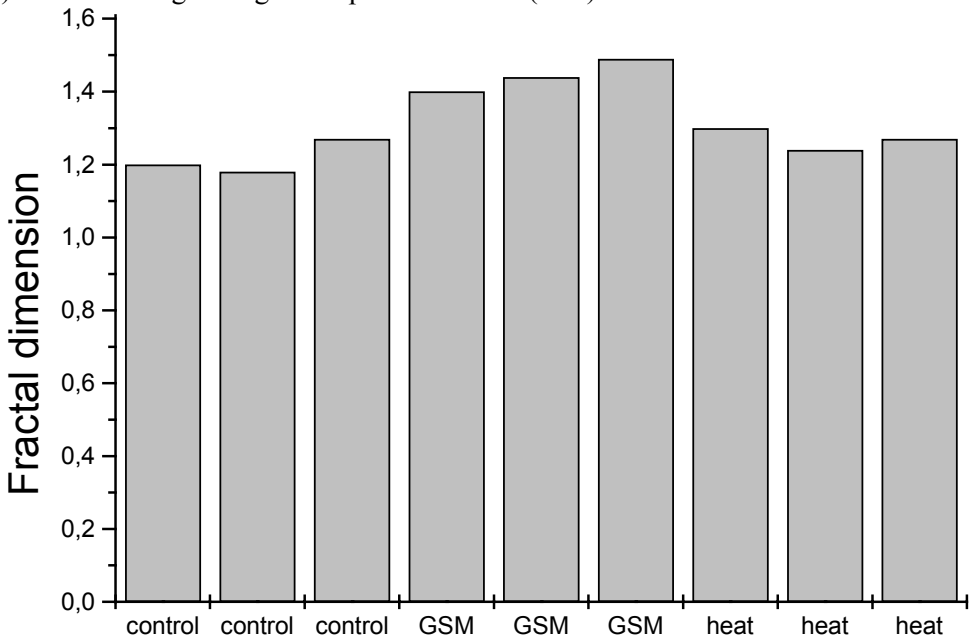

Fig. 2. Fractal dimensions of tumours boundaries at different conditions.

As is clearly seen the fractal dimension of "GSM" tumours is significantly higher than in the other two groups, which demonstrate for the first time the new effect mediated by mobile phones. It should be stressed that the intensity of used GSM microwave radiation is about 50 fold higher than the intensity which is generated by mobile phones during their common use. Nevertheless these results indicates possible role of GSM radiation not in initiation but in acceleration of brain tumour growth and metastasing activity, which is probably higher in tumours with enhanced fractal dimension.

In conclusion, our results gives evidence of altered cellular reactions responsible for tumour cells proliferation by microwaves used in mobile communication. Because the fractal dimension of tumours growing at enhanced temperature 40 ^{o}C was not significantly different from the control growth, we can only hypothesize that observed increase in tumour growth in GSM field is due to some previously suggested nonthermal mechanisms behind the cells growth during electrostimulation.

4. Acknowledgement

This work was supported by VEGA grant 1/9179/02.

5. References

1. Mandelbrot BB. How long is the coast of Britain? Statistical self-similarity and fractional dimension. Science 1967;156:636-38.
2. Sedivy R. Fractal tumours: their real and virtual images. Wien Klin. Wochenschr. 1996;108:547-51.
3. Landini G, Rippin JW. Fractal dimensions of the epithelial-connective tissue interfaces in premalignant and malignant epithelial lesions of the floor of the mouth. Anal. Quant. Cytol. Histol. 1993;15:144-9.
4. Waliszewski P. Complexity, dynamic cellular network, and tumourigenesis. Pol. J. Pathol. 1997;46:235-41.
5. Sheikh K. Exposure to electromagnetic fields and the risk of leukemia, Archiv. Environ. Health. 1986;41:56-63.
6. Ahlbom A. A review of the epidemiological literature on magnetic field and cancer. Scand. J. Work. Environ. Health 1988;14:337-43.
7. Szmigielski S. Cancer morbidity in subjects occupationally exposed to high frequency (radiofrequency and microwave) electromagnetic radiation. Sci. Total. Environ. 1996;180:9-17.
8. Kwee S, Rasmark P. Changes in cell proliferation due to environmental non-ionozing radiation. 1. ELF electromagnetic fields. Bioelectrochem. Bioenerg. 1995;36:109-113.
9. Garcia-Sancho J, Montero M, Alvarez J, Fonteriz RI, Sanchez A. Effects of extremely-low-frequency electromagnetic fields on ion transport in several mammalian cells, Bioelectromagnetics 1994;15:579-83.
10. Monti MG, Pernecco L, Moruzzi MS, Battini R, Zaniol P, Barbiroli B. Effect of ELF pulsed electromagnetic fields on protein kinase C activation process in HL-60 leukemic cells. J. Bioelectr. (USA) 1991;10:119-25.
11. French PW, Donnelan M, McKenzie DR. Electromagnetic radiation at 835 MHz changes the morphology and inhibits proliferation of a human astrocytoma cell line. Biolectrochem. Bioenerg. 1997;43:13-8.
12. Berg H. Possibilities and problems of low frequency weak electromagnetic fields in cell biology. Bioelectrochem. Bioenerg. 1995;38:153-9.
13. Berg H. Problems of weak electromagnetic field effects in cell biology. Bioelectrochem. Bioenerg. 1999;48:355-60.
14. Fiedler U, Grubner U, Berg H. Electrostimulation of yeast proliferation, Bielectrochem. Bioenerg. 1995;38:423-5.
15. Hones I, Pospichil A, Berg H. Electrostimulation of proliferation of the denitrifying bacterium Pseudomonas stutzeri. Bioelectrochem. Bioenerg. 1998;44:275-7.
16. Bru A, Pastor JM, Fernaud I, Bru I, Melle S, Berenguer C. Super-rough dynamics on tumour growth. Phys. Rev. Lett. 1998;81:4008-11.
17. Freshney RI. Animal Cell Culture. Oxford: IRL Press; 1986.
18. Babincova M, Leszczynska D, Sourivong P, Babinec P. Influence of alternating magnetic field on two-dimensional tumour growth, Electro- and Magnetobiology, 2000;19:351-6.
19. Benda P, Lightbody J, Sato G, Levine L, Sweet, W. Differentiated rat glial cell strain in tissue culture. Science 1968;161:370-2.
20. HarFA, Harmonic and Fractal Image Analyser. Software for determination of fractal dimension (2001). Available at www.fch.vutbr.cz/lectures/imagesci

Application of Fractal Dimension in Evaluation of Cranial Suture Complexity

Janusz Skrzat, Jerzy Walocha

Department of Anatomy, Collegium Medicum, Jagiellonian University
Kopernika 12
31-034 Cracow, Poland
jskrzat@poczta.onet.pl

1. Introduction

Cranial sutures as the growth sites and articulations between bones of the skull resemble curve lines, which present vast range of morphological variation [7, 8]. Interparietal sutures vary distinctly among individuals and evaluation of their morphology has always been problematic, especially of those with intricate pattern. For a long time, scientists who studied sutural morphology used visual inspection to categorize appearance of cranial sutures and they tried to measure the length of cranial suture following the curves of the suture or simply to measure distance from the beginning to the end of the suture [1, 3]. These two parameters if divided by each other serve the index, which express sutural complexity. For the last decade fractal dimension has been also applied to measure complexity of cranial sutures as these structures can be treated as fractals because of their intricate contour, which if magnified reveals details in form of subtle projections [6].

Complexity of cranial sutures depends on the degree of interdigitations of the spicules, which are present on the edges of two opposing bones. These bony spicules are precisely interlocked and it provides for a solid connection between cranial bones but allowing small amount of movement.

The goal of this paper is to analyze frequency of the fractal dimension of the set of interparietal sutures, which in this case serve as example of biological fractal patterns.

Figure 1. Examples of the interparietal sutures as fractal curves

2. Material and method

We analyzed complexity of 40 interparietal sutures of the external surface of the cranial vault. The specimens were taken from the skulls which belong to the collection of the Anatomical Museum of the Jagiellonian University in Cracow. The images of these sutures were acquired in the following manner. A transparent tape had been placed on the external surface of the skull along the analyzed suture and its contour was traced with a marker that drew a thin line. Traced silhouettes of the sutures were scanned with a flat bat scanner and the digitized images were skeletonized to obtain a line wide of 1 pixel. Such obtained images of cranial sutures silhouettes were subjected to the HarFa software, which measured fractal dimension of the sutural images using the box-counting algorithm.

3. Results

The estimated fractal dimension of the contours of the interparietal sutures ranges from 1.1 to 1.59 and mean value equals 1.34 (std dev. = 0.114). Frequency of the fractal dimension in the analyzed sample is presented on *Figure 2*.

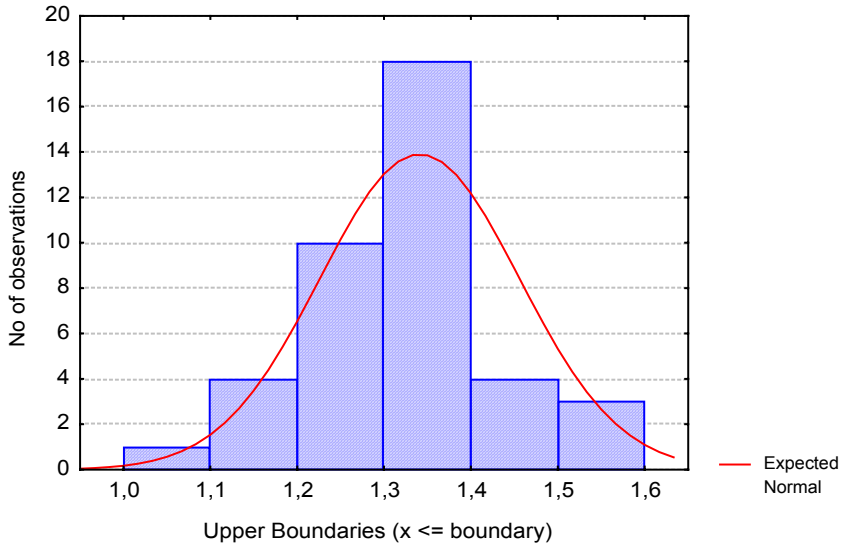

Figure 2. Frequency histogram of the fractal dimension of the analyzed interparietal sutures

Fractal dimension of the range 1.3 – 1.4 is the most representative for the studied sutures and it constitutes 45 %, whereas the lowest values (1.0 -1.1) are rare (2.5 %) and contrast to the highest values (1.5 – 1.6) of fractal dimension, which contribute three times more (7.5 %). More than half of the analyzed sutures yielded fractal dimension higher than median value (1.35) of the range of variation. It indicates that interparietal sutures appear more frequently as complicated patterns than simply convoluted lines.

4. Discussion

Fractal dimension seems to be a proper and objective descriptor of cranial suture complexity and it is more valid if the sutures are more intricate because than they show higher level of self-similarity. It proves that fractal geometry cope better with biological irregular patterns than classic methods of Euclidean geometry, which in this case would only approximate real features of the analyzed object [2]. There is considerable diversity in the patterns of cranial sutures; nevertheless they can be classified as curves which resemble fractals, eg. Koch's curve. Intricate interparietal suture shows 2-3 orders of scaling and yield fractal dimension about 1.3 - 1.4 [6].

Fractal dimension as a quantitative measure of sutural complexity enables to categorize sutural complexity. According to my previous studies, the analyzed set of interparietal sutures can be

regarded as considerably complicated [9]. Moreover fractal dimension becomes a helpful parameter which can be easily compared or correlated to other metrical characteristics of the skull or selected cranial bone. Sutural complexity is strictly related to amount of interdigitations of the edges of the linked bones. As it was reported by Jaslow increase energy absorption was correlated with increased sutural interdigitations [5]. The sutures between cranial bones provide for not only interstitial growth of the cranium, but they also alter the transmission of stress and strain through the skull [4].

Measurements of cranial suture complexity seem to be important in a case of considerations of mechanical properties of the articulations between cranial bones, their function and stability in the entire skull. Because of important role which sutures play in the skull a thorough investigation of these structures is essential for better understanding functional aspects of the skull. We presume that fractal approach to cranial suture morphology may be crucial in mentioned problems.

5. Literature

1. Anton SC, Jaslow CR, Swartz SM. *Sutural complexity in artificial deformed human (Homo sapiens) crania*. J Morphol, 214: 321-332, 1992.
2. Hartwig WC. *Fractal analysis of sagittal suture morphology*. J Morphol, 210: 289-298, 1991.
3. Hauser G, Manzi G, Vienna A, De Stefano GF. *Size and shape of human cranial sutures – a new scoring method*. Amer J Anat, 190 (3), 231-244, 1991
4. Herring SW, Teng S. *Strain in the braincase and its sutures during function*. Am J Phys Anthrop, 112: 575-593, 2000.
5. Jaslow CR. *Mechanical properties of cranial sutures*. J Biomech, 23(4): 313-321, 1990.
6. Long CA, Long JE. *Fractal dimensions of cranial sutures and waveforms*. Acta Anat, 145 (3): 201-206, 1992.
7. Opperman LA. *Cranial sutures as intramembranous bone growth sites*. Dev Dyn, 219: 472-485, 2000.
8. Persson M. *The role of the sutures in normal and abnormal craniofacial growth*. Acta Odontol Scand, 53:152-161, 1995.
9. Skrzat J, Chmiel D, Usarz M. *Fractal complexity as a new measure of the cranial suture complexity*. Medical Review - Scripta Periodica, 3 (3): 418-422, 2000.

Fractal Dimension Based on Box Counting: A New Parameter for the Quantification of Dynamic PET Studies

Antonia Dimitrakopoulou-Strauss, Ludwig G. Strauss

Medical PET Group - Biological Imaging
Clinical Cooperation Unit Nuclear Medicine
German Cancer Research Center, Heidelberg, Germany
ads@ads-lgs.com

1. Introduction

Positron emission tomography (PET) provides the possibility to measure accurately radioactivity concentrations. Standardised uptake values (SUV) have found widespread use since the introduction more than 10 years ago, because it is a fast and reproducible semiquantitative parameter. Some investigators proposed the use of compartimental approaches to obtain more detailed information about the radiopharmaceutical kinetics. However, the application of a two compartment model for the F-18-Deoxyglucose (FDG) kinetics may be limited in some patients, e.g. if the input function is not available or the dynamic data are too noisy. We implemented a non-compartmental method, the fractal dimension, for the analysis of dynamic PET data. In contrast to the two-compartment model, no input function is required. The fractal dimension (FD) is based on the chaos theory and provides information about the "deterministic" or more "chaotic" distribution of uptake values. It is a new method, which may be interesting for the evaluation of dynamic data sets like the tracer uptake in an organ as a function of time. While some authors have calculated the FD of an image to assess the bone structure or the distribution of lung ventilation, we applied the FD in the time direction to quantify the FD for each voxel of a dynamic PET study. Purpose of this study was to assess the feasibility and the diagnostic value of the fractal dimension for oncological patient studies, especially in patients following treatment.

2. Material and Methods

Patients: The evaluation includes 200 tumor lesions (from 159 patients) as well as 57 benign lesions (57 patients). Histologies: 22 metastases from malignant melanoma (17 pretreated patients); four liver metastases from carcinoid tumors (two patients); 29 malignant breast tumors (29 patients); 14 metastases from malignant lymphoma (6 pts with Hodgkin´s disease and one patient with Non-Hodgkin´s disease, following first line treatment); 56 liver metastases (29 patients with metastatic colorectal carcinoma, following first line chemotherapy); 31 malignant bone tumors (10 osteosarcomas, 2 Ewing`s sarcomas, 7 giant cell tumors, one intraosseous hemangiosarcoma, two plasmocytomas, 5 bone metastases, two neuroectodermal tumors, one Non- Hodgkin lymphoma of the bone and one perspiration gland carcinoma); 44 mal. soft tissue tumors (29 liposarcomas, 3 haemangiosarcomas, 6 leiomyosarcomas, 6 mal. fibrous histiocytomas). 101/200 tumors were treated with chemotherapy within the last six months prior to PET.

Benign lesions: 2 scars (3 pts) with primary lymphomas, 4 benign breast lesions, 36 benign bone lesions (10 enchondromas, 7 scars, 3 osteomyelitis, 4 bone cysts, two fibromas, two ganglions, one osteitis, one bone necrosis, one bone hematoma, one eosinophilic granuloma, two osteochondroma, one bone edema, one Paget) and 15 benign lesions arising from the soft tissue (7 scars, 5 lipomas, one hemangioma and two inflammatory lesions).

The final diagnosis included the histological data obtained from surgical specimens for the lesions of the musculosceletal system and the breast lesions, while the clinical follow-up data for at least six months after the FDG study was used for the other patients.

Data acquisition: Dynamic PET studies were performed following the application of 300-370 MBq FDG for 60 min. All patients were in fasting state and blood glucose level was measured prior to PET.

A dedicated PET system with a craniocaudal field of view of 15.3 cm was used (theoretical slice thickness 2.4 mm). All PET images were attenuation corrected and reconstructed with a dedicated software package on PC systems using an iterative reconstruction algorithm (weighted least square, ordered subsets).

Data analysis: The evaluation of the dynamic PET data was performed using the software package PMod, provided by a cooperation with C. Burger, Univ. of Zuerich, Switzerland. Time-activity curves were created using Volumes of Interest (VOIs). Irregular ROIs were drawn manually. To compensate for possible patient motion during the acquisition time, the original ROIs were visually repositioned, but not redrawn. We used for the basic analysis the semiquantitative approach based on the calculation of a distribution value, for which the term "standardised uptake value" (SUV) was introduced by Strauss and Conti (*The application of PET in oncology. Strauss LG, Conti PS. J Nucl Med 1991;32:623-648*): SUV = tissue concentration (MBq/g) / (injected dose (MBq) / body weight (g)). The 55-60 minute uptake value was used for the quantification of the data. A non-compartment model based on the fractal dimension was used for the data evaluation. As already shown by other investigators, the fractal dimension is a parameter for the heterogeneity. A Java-based module was implemented in the PMod software to calculate the fractal dimension for the time-activity data. The program is based on the box counting method. Besides the calculation of the FD for VOIs, parametric images of the FD were generated from the dynamic PET data. The statistical evaluation of the data was performed using the Statistica software package (Version 6.0, Stat- Soft Co, Hamburg, Germany). Descriptive statistics and Box- Whiskers plots were used for the analysis of the data. Discriminant analysis was used to determine the diagnostic accuracy using both SUV and fractal dimension with regard to the final histological diagnosis.

3. Discussion

PET with FDG is generally used for both the primary diagnosis and staging as well as for follow up in patients after treatment to assess the effect of therapy and/or detect recurrences. Several authors have reported a high sensitivity of FDG PET in untreated patients. We evaluated PET studies in both treated and untreated patients and the quantitative data demonstrated an overlap of the SUV and FD in these patients. Discriminant analysis revealed a low sensitivity of 61% for all lesions, with a sensitivity of 55.6 % for the untreated and 63.4 % for the treated subgroup when the SUV were used to differentiate benign and malignant lesions. The specificity of SUV was high at the level of 91 % for both subgroups. We noted for FD an overall sensitivity of 78 %, with 70.7 % for the untreated and 84.2 % for the treated lesions. The specificity of FD was 72 % for all lesions, 62.5 % for the untreated lesions and 82.1 % for the treated lesions, when FD was used to differentiate benign and malignant lesions. The decision level to discriminate the benign and malignant lesions (calculated by the software) was 2.3SUV (tu.:>2.3SUV) and 1.145FD (tu.:>1.145 FD).

FD was superior to SUV, but the best diagnostic accuracy was achieved when both parameters were used. Interestingly, both SUV and FD had a higher accuracy in treated lesions.

Conclusions: The use of FD is a reliable method for the quantification of dynamic PET studies and seems to be more robust than the SUV in particular for the evaluation of treated lesions. It is a fast procedure, which does not demand any input function as compared to compartment methods.

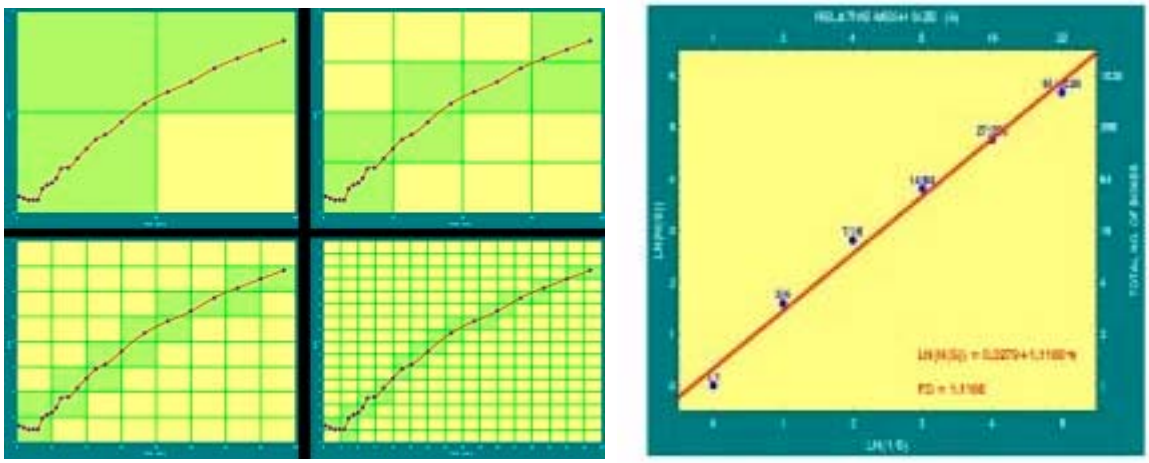

Fig. 1: Calculation of the FD based on box counting method in a time activity curve (TAC) of a giant cell tumor. The TAC of VOI is overlaid with a sequence of rectangular grids. The boxes containing some of the structure of the TAC are highlighted with transparent green.
A log-log plot is generated (number of grid segments, which intersect an object of interest versus the inverse of the grid side length). The slope of a line fitted to the data is used as an estimate of FD (right).

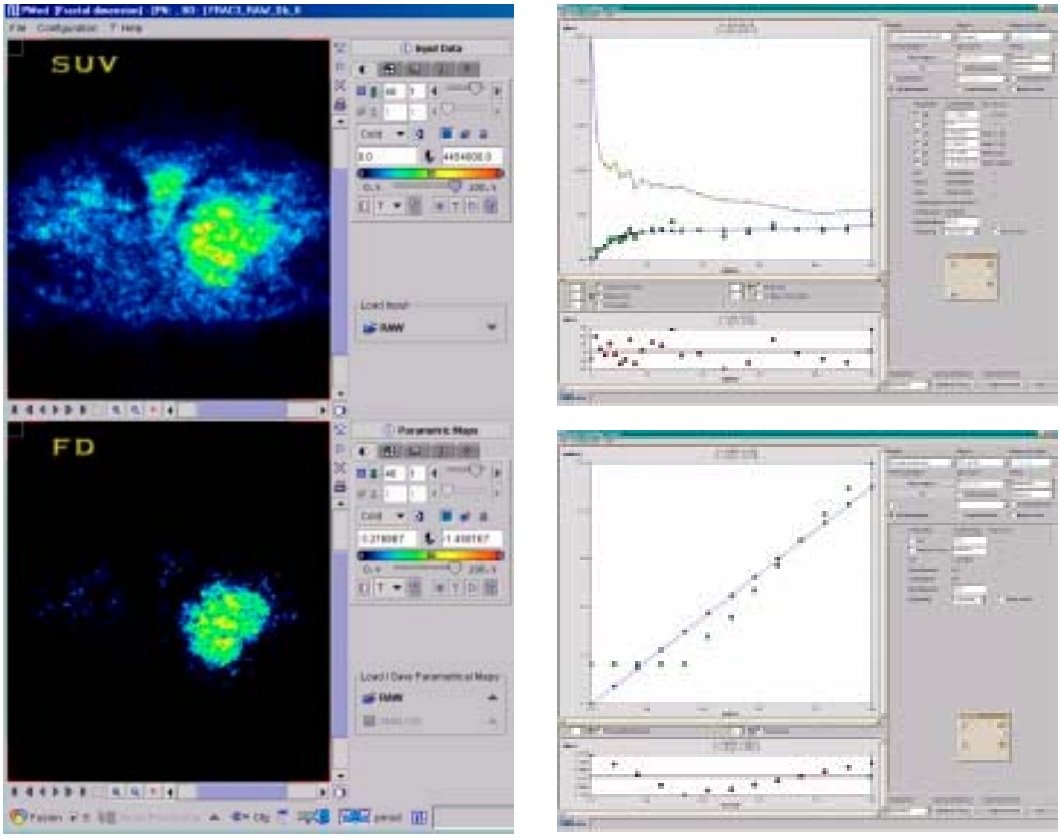

Fig. 2: FDG study of a patient with a soft tissue sarcoma (G I). The SUV image (upper left, SUV) demonstrates tracer uptake in both the tumor and normal structures, while the parametric image of the fractal dimension (lower left, FD) shows only the tumor area. The del ineat ion of the mal ignant l esion is superior as compared to the SUV image. Upper right: kinetic data for the tumor. Low K1 and k3, resulting in a low tracer uptake. Lower right: calculation of the fractal dimension for the tumor (FD=1.41). No input function is needed.

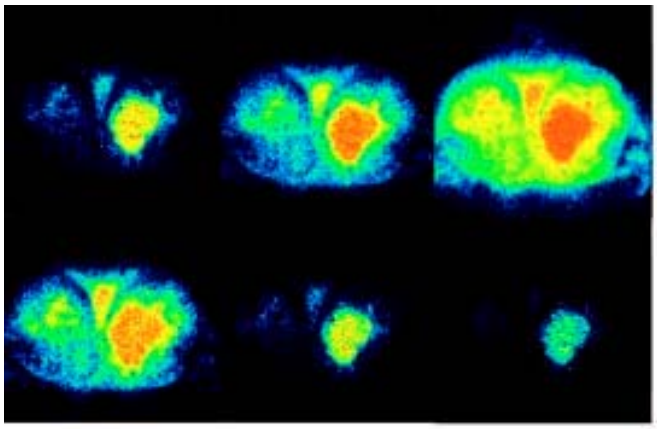

Fig. 3: Pixelwise parametric FD images of the patient in Fig. 2 using different parameters for the FD images. Upper row: the total no. of subdivisions was variied from 8 × 8 (left), to 32 × 32 (middle) to 128 × 128 (right), while the max. was kept constant at 20 SUV. Lower row: constant no. of subdivisions (8 × 8), variation of the max. cutoff SUV from 5 (left) to 30 (middle) to 55 (right).

Tab. 1: Effect of the variation of the number of subdivisions and the cutoff values for the upper threshold on the Minimum and Maximum estimates of FD.

TOTAL NO. BOXES	MAXIMUM (SUV)	MIN FD	MAX FD
8 × 8	**20**	**0.017**	**0.827**
32 × 32	**20**	**0.008**	**1.084**
128 × 128	**20**	**0.005**	**1.321**
8 × 8	**50**	**0.017**	**1.100**
8 × 8	**30**	**0.017**	**0.629**
8 × 8	**55**	**0.017**	**0.390**

Tab. 2: Discriminant analysis for all untreated lesions (99/200) with respect to malignant and benign lesions.

	SUV	FD	SUV, FD
sensitivity	55.55% (55/99)	70.71% (70/99)	58.59% (58/99)
specificity	91.07% (51/56)	62.50% (35/56)	91.07% (51/56)
accuracy	68.39% (106/155)	67.74% (105/155)	70.32% (109/155)
PPV TP	91.66% (55/60)	76.92% (70/91)	92.06% (58/63)
PPV TN	53.68% (51/95)	54.69% (35/64)	55.43% (51/92)

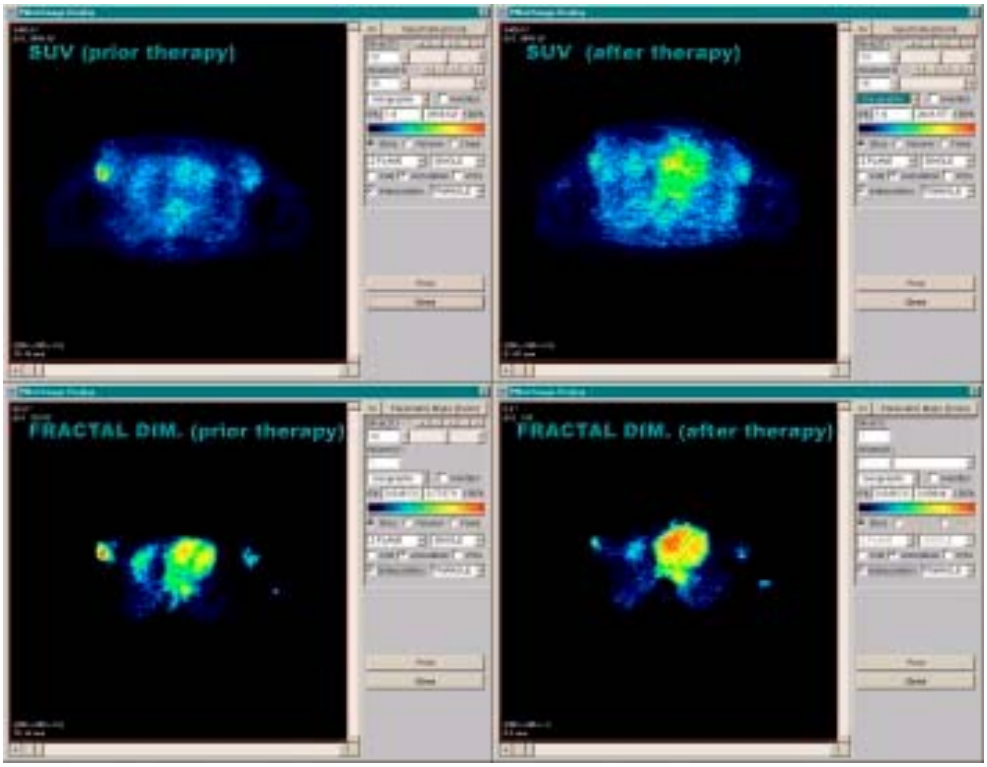

Fig. 4: FDG studies in a patient with a carcinoma of the left and right breast as well as small lung metastases on the right side. The FDG study was performed prior to therapy and one week following high dose chemotherapy. The FDG uptake prior to therapy was highest for the tumor in the right breast (image, upper left). Following treatment we noted a decrease of the tracer uptake (image upper, right; both images are scaled from 0-100 %). The parametric images of the fractal dimension (lower images) delineate both tumors as well as the lung metastases prior and after treatment with high contrast. The fractal dimension was lower following therapy.

Tab. 3: Discriminant analysis for all treated lesions (101/200) with respect to malignant and benign lesions.

	SUV	FD	SUV, FD
sensitivity	63.37% (64/101)	84.16% (85/101)	79.21% (80/101)
specificity	91.07% (51/56)	82.14% (46/56)	83.93% (47/56)
accuracy	73.25% (115/157)	83.44% (131/157)	80.89% (127/157)
PPV TP	92.75% (64/69)	89.47% (85/95)	80.80% (80/99)
PPV TN	57.95% (51/88)	74.19% (46/62)	69.12% (47/68)

Fractality in the *Nautilus Pompilius* Shell

text from Fractals 11, 3 (2003)

A. A. Castrejón Pita[1], J. R. Castrejón Pita[1], A. Sarmiento Galán[2] and R. Castrejón García[3]

[1]Centro de Investigación en Energía, UNAM A. P. 34,
62580 Temixco, Morelos, México.
aacp@mazatl.cie.unam.mx
[2]Instituto de Matemáticas, UNAM, Ave. Universidad s/n,
62200 Chamilpa, Morelos, México.
ansar@matcuer.unam.mx and
[3]Instituto de Investigaciones Eléctricas, Ave. Reforma 113,
62490 Temixco, Morelos, México.
rcg@iie.org.mx

The complexity of the *Nautilus Pompilius* shell is analysed in terms of its fractal dimension and its equiangular spiral form. Our findings assert that the shell is fractal from its birth and that its growth is dictated by a self-similar criterion (we obtain the fractal dimension of the shell as a function of time).

1. Introduction

Fractal analysis is being applied with increasing frequency to living organisms, trying to explain some of the complex forms found in nature. An astonishing example reveals that *Ammonites* continuously increased their complexity up to the point in which they became extinct [1]. It is our purpose to study in this paper the amazing complexity of a close relative of the *Ammonites*, the *Nautilus pompilius.*

This pelagic species is a native of the western Indopacific ocean (30° N lat. to 30° S lat. and 90° to 185° W long. [2]), and usually lives at a depth that varies from 50 to 480 meters (temperature ranges from 24 to 8 Celsius degrees).

The shell is mother-of-pearl lined and pressure resistant (it implodes at approximately 800 m); its hardness has been the basis of various ornamental handicrafts [3]. But the most striking characteristic of this thin, two layered, and spirally coiled shell is its internal subdivision in a series of successive chambers (phragmocone), starting from the very moment of hatching when there are already seven chambers present in the shell. As the cephalopod grows and requires more space, it creates a new chamber by sealing the space behind it with a calcareous septum and moves to live at the open, bigger end of the shell. The rate at which a new chamber is created varies, at the beginning it seems to take longer for the mollusc to seal the 8th chamber but later on, the process takes from 43 to 77 days per chamber [4] and lasts up to the completion of approximately 39 sealed chambers [5] plus the open space where the mollusc lives [6]; these changes in the growth rate are easily understood in terms of the food availability and other environmental variables. The sealing of the chambers however, is not complete, there is a small duct in the center of each wall, called siphuncle, that allows the living fossil to keep control of the pressure inside every previous chamber and thus to regulate its buoyancy [7], [8]; the heyday of the nautiluses is estimated to be around 500 million years ago.

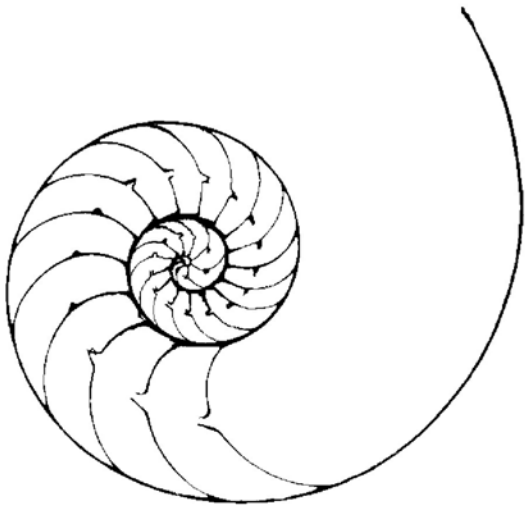

Fig. 1 Black and white image of a transversal cut of a Nautilus pompilius *shell.*

A transversal cut of the shell, *Fig. 1*, shows a perplexing spiral geometry, not found in any other natural object; this is a black & white image where the borders have been prepared to facilitate the box-counting analysis. The hemishell is 96.1×106.2 mm and 32.2 mm wide; the number of chambers is 30. Most amazing is the fact that its growth appears to be self-similar, and thus for the shell to possess a fractal dimension. We now proceed to confirm that this is indeed so.

2. Method

The digital image in Fig. 1 was obtained by placing half of the shell directly on a scanner bed; the cutting 2 was performed going through half of the shell as accurately as possible. All measurements are performed on the digital images, in pixel units, and the conversion factor is given by the scanner resolution (72 pixels per inch). The borders of the edges in the hemishell were previously tinted to gain contrast and improve definition, and thus, making the contour threshold treatment unnecessary.

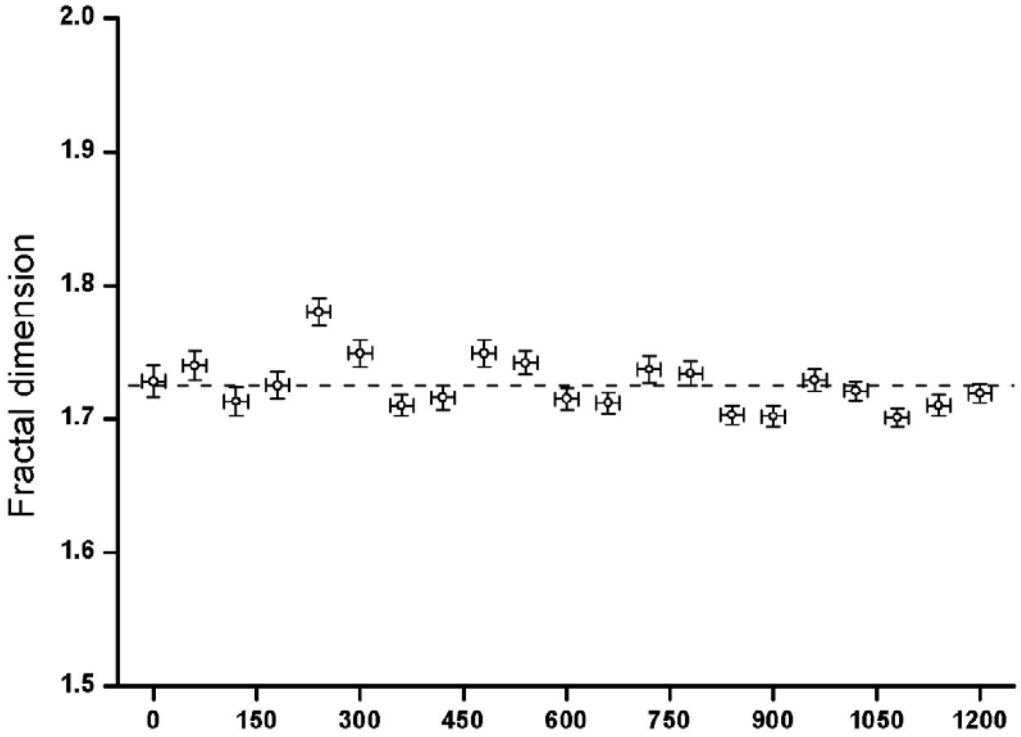

Fig. 2 Fractal dimension of the shell as a function of time, the age is measured in days after hatching, starting with the 8th chamber

The box counting method (with HarFA) is applied to the original image and the fractal dimension of the whole shell is obtained via a linear fit to the data [9]. In order to test the observed self-similarity, we analyse the fractal dimension of smaller fragments of the image, that is, if we check that its complex structure is the same regardless of the scale used to measure it. To accomplish this test, we proceeded as follows; once the box-counting method had been applied to the whole, bigger image, the last chamber was digitally eliminated from the initial image and the method reapplied to the new image after adjusting the maximum possible size to the new, smaller image size. This procedure was repeated up to the point in which there were only the original seven chambers in the shell. We have also used an average value for the time required for the construction of a new chamber in order to obtain the fractal dimension of the shell as a function of time, *Fig. 2*, this average value is 60 ± 17 days per chamber.

3. Results

The fractal (box-counting) dimension of the original *Nautilus* shell shown in *Fig. 1* is 1.635 ± 0.006; the average of the self-similar fractal dimension of the shell (*Fig. 2*) is 1.730 ± 0.019; this is an average over the life of the particular *Nautilus* and clearly depends on the accuracy of the available data on the shell growth. The lower value for fractal dimension of the original shell with respect to the average, is due to the fact that the shell extension where the mollusc lives is included in the original image (*Fig. 1*)

4. Conclusions

In the previous analysis, we have shown that the shell of the *Nautilus pompilius* that we have analysed, possesses a fractal dimension, that its value is 1.635 ± 0.006 (1.730 ± 0.019 on average), and that it does not depend on the number of chambers (or, equivalently, the age) used to calculate it. This establishes the self-similar structure of the shell at any scale/time, and how its growth follows the same self-similar criterion.

5. References

[1] G. Boyajian and T. Lutz, *Geology,* 20, 1992.
[2] W. B. Saunders in *Nautilus, The Biology and Paleobiology of a Living Fossil*, W. B. Saunders and N. H. Landman, eds. (Plenum Press, New York, 1987).
[3] H. Stix, M. Stix, and R. Tucker Abbott, *The Shell, Five Hundred Million Years of Inspired Design*, (H. N. Abrams, Inc., New York, 1968).
[4] N. H. Landman, J. K. Cochran, J. A. Chamberlain Jr., and D. J. Hirschberg, *Marine Biology*, 102, 65 (1989).
[5] *The New Encyclopaedia Britannica*, (Encyclopaedia Britannica Inc., 15th edition, Chicago, 1979).
[6] P. Hall, *Pearly or Chambered Nautilus*, 1997 Journal of The Marine Life Society of South Australia Inc., http://www.mlssa.asn.au/
[7] S. Bruno, *Guía de Moluscos*, (Ed. Grijalbo, Madrid, Spain, First edition, 1982).
[8] J. Parker and W. A. Haswell, *A Text-book of Zoology*, (Mac Millan and Co., London, 6th edition, 1940).
[9] M. Nezadal and O. Zmeskal, *Harmonic and Fractal Image Analyser*, webpage: http://www.fch.vutbr.cz/lectures/imagesci, 2001.

Quantitative Comparison of Lineal Analysis to Box Counting Analysis of a Real Microstructure

Rand Dannenberg

Chahaya Optronics, 94954 Fremont, USA

Summary – Expressions relating box counting and lineal analysis are developed. Both methods are used for fitting the spacing distribution of a real microstructure. The relation to grain size distribution is discussed.

1. Conversion of HarFA spectrum into an Areal Size Distribution.

HarFA (Harmonic Fractal Analyzer) will generate a plot of the fractal dimension D vs. the ln(s) where s is the box size. The fractal dimension is defined as

$$D(s) = -\,\mathrm{dln}(N)/\mathrm{dln}(s),$$

where N is the number of boxes that contain a black pixel when a grid of size s is overlayed on the image. If the image is a fractal and self-similar, the D is independent of s

$$\int_{\ln(N1)}^{\ln(N2)} d\ln N = -\int_{\ln(s1)}^{\ln(s2)} D(s)\, d\ln(s)\ .$$

So that for a real fractal

$$N2 = N1\left(\frac{s2}{s1}\right)^{-D},$$

where $N2$ is the number of boxes of side $s2$ and $N1$ is the number of side $s1$.

If the microstructure is not self-similar, then D varies with s. In that case, we can treat the right hand side as a differential and integrate the small change with the trapezoidal rule to obtain

$$\ln(N2/N1) \approx -(D2+D1)[\ln(s2) - \ln(s1)]/2$$

and

$$N2 \approx N1\left(\frac{s2}{s1}\right)^{-\{D2+D1)/2}$$

where $D2$ and $D1$ are the D's at $s1$ and $s2$. Note that this is only true if $s1$ and $s2$ are close together and D changes slowly over that range.

The number of boxes we would predict to find at $s2$ if the system remained self-similar from $s1$ on is

$$N2_{SS} = N1\left(\frac{s2}{s1}\right)^{-D1}.$$

Microstructures are not fractals and are not expected to be self-similar. As the box size decreases, the rate of "all white box" generation will increase faster than the self-similar case. That loss can be equated to an areal change which is the largest for the box sizes closest to important spacing in the image.

The area reductions between $s1$ and $s2$ are

$$A = (N2_{SS} - N_2)s2^2.$$

Writing $s2 = s1+\Delta s$ and using $(1+\Delta s/s1)^{-D} \approx 1-D\Delta s/s1$ for small Δs, after some algebra one finds

$$\Delta A = (1/2)\ N1\ (\Delta s/s1)\ (D2 - D1)\ s2^2.$$

Since $s1 \approx s2$ we can drop the subscripts, and replace $N1$ by $N(s)$. By multiplying by $\Delta s/\Delta s$ we can treat $(D2-D1)/\Delta s \approx dD/ds$, and rewrite,

$$\Delta A(s) = s\, N(s)\, \Delta s^2\, (dD/ds)/2.$$

This is a distribution that can be normalized by dividing by

$$\int \Delta A(s) ds/\Delta s.$$

The number of boxes is found by dividing $\Delta A(s)$ by s^2,

$$\Delta N(s) = s^{-1}\, N(s)\, \Delta s^2\, (dD/ds)/2.$$

For image analysis, Δs is a constant, and is equal to the scaled width of a pixel. This expression gives a relationship between the area lost at important spacings in the spacing distribution, and the rate of change of the fractal dimension. For perfectly self-similar images, $\Delta A(s) = 0$ and $\Delta N(s) = 0$.

$\Delta A(s)$ and $\Delta N(s)$ might be related to a grain size distribution through modeling assumptions. However, that is difficult to do. The important point to be taken from this analysis is that the size of the activity is proportional to dD/ds. The peaks in the derivative are useful for identifying feature sizes of activity and verifying intuition about important grain size distributions in a microstructure.

2. Quantification of a Variation of the Secant Method

The secant method is a fast manual method in which a line of length S is drawn over a microstructure and the number of intersections is counted. Many secants are drawn with the number of intersections counted then averaged. It is easy to show that the average grain size returned by this method is $D_{sec} = S\langle 1/n\rangle_{ave}$; averaging S/n on each secant, the average grain size per secant. Also, $D'_{sec} = S/n_{ave}$; averaging n/S on each secant then inverting the average.

The latter can be very easily shown to be much quieter and accurate than the former.

A variation on the secant method is to record the intersection length for every intersection on every secant and average the intersection length values. When this is done, the average grain size determined by the variation of the method is

$$D_{int} = \Sigma\, l/N = TS/\Sigma\, n = S/(1/T)\Sigma\, n = S/n_{ave} = D'_{sec}.$$

where l is an intersection length, N is the total number of intersections, n is the number of intersections on a secant, and T is the total number of secants.

More information is available in the method that produced D_{int}. Suppose we make a histogram of the number of intersections that fall between l and $l+\Delta l$, using parallel secant lines that "scan" in a direction perpendicular to the lines, with the spacing between secants Δl. Now consider an image of a microstructure, and let Δl be the width of a single pixel. The length distribution would be the sum over all the *individual* grains of the number of times the spacing l occurred in each grain,

$$f(l,O) = \sum_G \eta_G(l,O).$$

The O designates the orientation to which the secant lines are perpendicular. G designates a grain.

This is a very simple expression. In order to relate it to a grain size distribution some assumptions about the make-up of the microstructure need to be made. Let us assume the following:

1. There is a number distribution of grain sizes in the microstructure, $n(g)$, where g is a grain size.
2. The grains have the same shape.
3. There is a function that tells us the number of times a length l occurs in a grain of size g. $q(l/g,O) = q(\beta,O)$, where the length parameter $\beta = l/g$.
4. The secant will move parallel to the largest length in the grains.

As an example, suppose there was a microstructure that was made up of all square shaped "grains" of different sizes filling space, and the secant line moves parallel to the diagonals. In that case, *q(unity,diag)* = 1 and *q(all others,diag)*=2. In grain of regular shape one would expect to find in a real microstructure the rate of change of q with respect to β is expected to be small. By assumption #4, we are defining the grain size to be the largest length in the grains. In the limit if circular grains, the secant lines will always be parallel to the length that defines the grain size. The latter also implies that $q(l/g) = 0$ for $g < 1$.

In reviewing these assumptions, it should be remembered that a large body of work exists on the characterization of grain size distributions in metals, where it is assumed that all grains are either circular or square, without considering the implications for the space-filling requirements.

The sum can now be taken over the grain sizes instead of individual grains, and written as

$$f(l,O) = \sum_{g\geq l}^{\infty} q(l/g,O)n(g) \cong \int_{l}^{\infty} q(l/g,O)n(g)\frac{1}{\Delta g}dg\,, \qquad (1)$$

where the Δg comes from passing the sum to an integral. The limits of the integration (or range of the sum) come from $g(l/g) = 0$ for $g < l$, since there can be no lengths in a grain that are greater than the grain size (by assumption #4). Equation 1 tells us that $f(l)$ is a *cumulative distribution*, most notably from the integral form.

To arrive at a relationship between $f(l)$ and $n(g)$ that might be extracted directly from data, consider from the summation that

$$f(l) - f(l+\Delta l) = \sum_{g\geq l}^{\infty} q(l/g)n(g) - \sum_{g\geq l+\Delta l}^{\infty} q(l+\Delta l/g)n(g).$$

The right hand side equals

$$q(\tfrac{l}{l})n(l) + q(\tfrac{l}{l+\Delta l})n(l+\Delta l) + q(\tfrac{l}{l+2\Delta l})n(l+2\Delta l) + \ldots - q(\tfrac{l+\Delta l}{l+\Delta l})n(l+\Delta l) + q(\tfrac{l+\Delta l}{l+2\Delta l})n(l+2\Delta l) + \ldots .$$

If q is constant or changes slowly such that

$$|\, q(\tfrac{l+\Delta l}{l+p\Delta l}) - q(\tfrac{l}{l+p\Delta l})\,| \,/\, q(\tfrac{l}{l+p\Delta l}) << |\, n(l+p\Delta l) - n(l+(p-1)\Delta l)\,| \,/\, n(l+p\Delta l)\,,$$

then terms containing $n(l+p\Delta l)$ are equal and only the very first term in the series remains in the difference, so that

$$n(l) \cong -\frac{\Delta g}{q(1)}\frac{\mathrm{d}f}{\mathrm{d}l} \quad \text{or} \quad n(l) \propto -\Delta g\frac{\mathrm{d}f}{\mathrm{d}l}. \qquad (2)$$

An alternative way of arriving at equation 2 is to rewrite equation 1 as the anti-derivative difference

$$f(l) = F(\infty) - F(l).$$

Differentiating both sides gives

$$\frac{\mathrm{d}f(l)}{\mathrm{d}l} = \frac{\mathrm{d}F(g=\infty)}{\mathrm{d}l} - \frac{\mathrm{d}F(g=l)}{\mathrm{d}l}.$$

The first term is zero, because $n(g) = 0$ for g significantly less than ∞, therefore, the anti-derivative at infinity must be equal to a constant. As for the second term, it must have the same functional form as the integrand of equation 1, resulting in

$$\frac{\mathrm{d}f(l)}{\mathrm{d}l} = -\frac{q(1)n(g)}{\Delta g},$$

which leads back to equation 2. Therefore, the assumptions about the slow rate of change of q are built into the conversion from sum to integral.

Consider that $F(g)$ is the anti-derivative of a distribution. $I = F(\infty) - F(0)$ is the total area beneath that distribution, in this case, the total number of intersections in the image. Unless the distribution is weighted very close to $g = 0$, $I \cong F(\infty)$.

Note that the O has been dropped, but the orientation dependence is implicit. The proportionality in Equation 2 is there since $q(l)$ is constant. Both derivations lead to the constant of proportionality $q(l)$, thus in grains of all the same shape, the only remaining influence from the shape function is the number of times the largest length g appears in the grains of size g.

The total area of the grains of size between l and $l+\Delta l$ is

$$\Delta A(l) \propto n(l) l^2. \tag{3}$$

In the above derivations, it is to be understood that the *l's* and *g's* and *s's* are equivalent as far as the histogram is concerned.

Grains are not square, nor do they have the same shape, so there is much uncertainty surrounding the entity $q(l/g)$. Given the wealth of work in which microstructures have been treated as though all the grains are squares or circles and the common equating of average secant intercept length to average grain size, we argue that $q(l/g) = constant$ will put this method on similar footing with more standard methods. Using $q=2$ seems reasonable for circles or diamond shaped grains.

It should be remembered that $f(l,O)$ is actually convolution of number of grains of size l and grain shape.

3. Application to a complicated microstructure

The assumptions made above are never going to be strictly true, but if they are good enough, then they would provide functional forms that would be useful for fitting data to real microstructures, and that is the most important test.

An example will be shown for a microstructure that is very complex. The figure below shows a microstructure that has either grain size gradients and/or overlapping grain size distributions. To make matters more complicated, the image does not show the full microstructure, which enhances gradients in the data.

Our image is of a specimen of cryomilled $Ni_{20}Cr$. It is smoothed in Scion Image, and converted to an edge image in the same program. To generate $D(l)$ and dD/dl it is analyzed in HarFA.

Using the intersection analyzer code called DA written at Rockwell, a histogram of 23,000 intersection lengths is created, $f(l)$. The data is then differentiated as per *Eqn. 1*.

Peaks are observed in dD/dl *vs.* $\sqrt{2}\,l$ and also df/dl *vs. 1*. These peak positions and widths are then combined to fit gaussian forms for *n(g)* that are integrated in *Eqn. 2* in order to fit $f(l)$. The gaussians are then differentiated, and the fit is compared to the df/dl data. As will be seen, the fits are reasonable. Fitting of the gaussians is done on $f(l)$ since differentiating produces noise.

Two additional ideas are incorporated. First, in the peak identification from dD/dl, the *l's* of the peaks are multiplied by $\sqrt{2}$ for the centers of the gaussians. This is because we believe the area is lost due to shrinking of the box *diagnols* below the spacing between grain boundaries. This correction does not have to be applied to the intersection spacings. Second, in Eqns. 1–3, we assume that $q(l/g) = 2$ for all l/g since it will be equal to two for the overwhelming majority of *l's* for space filling grains in the simple case where their shape is square.

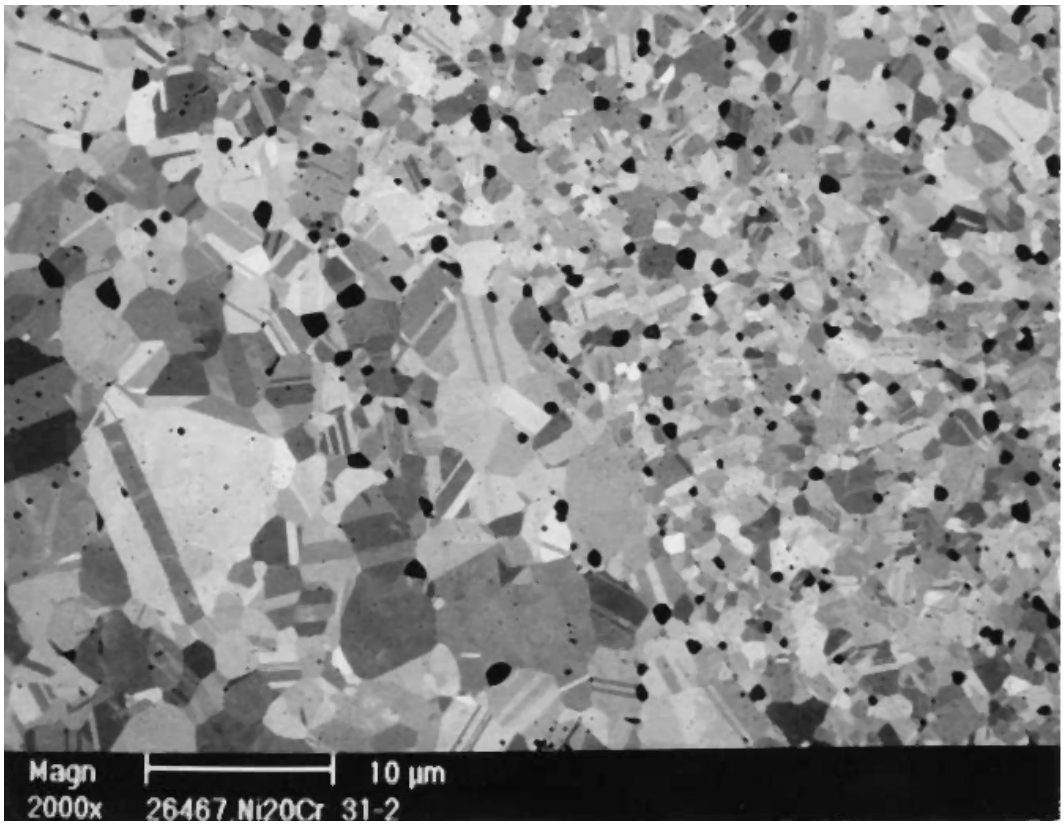

Original Image

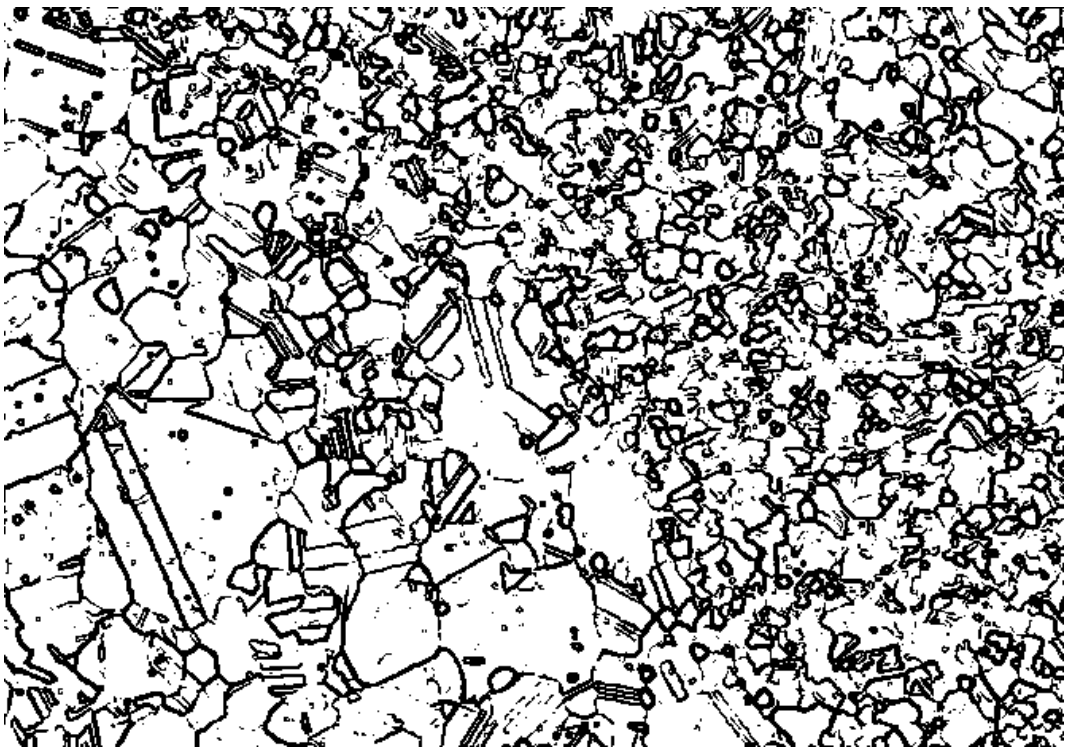

After Conversion to an Edge Image

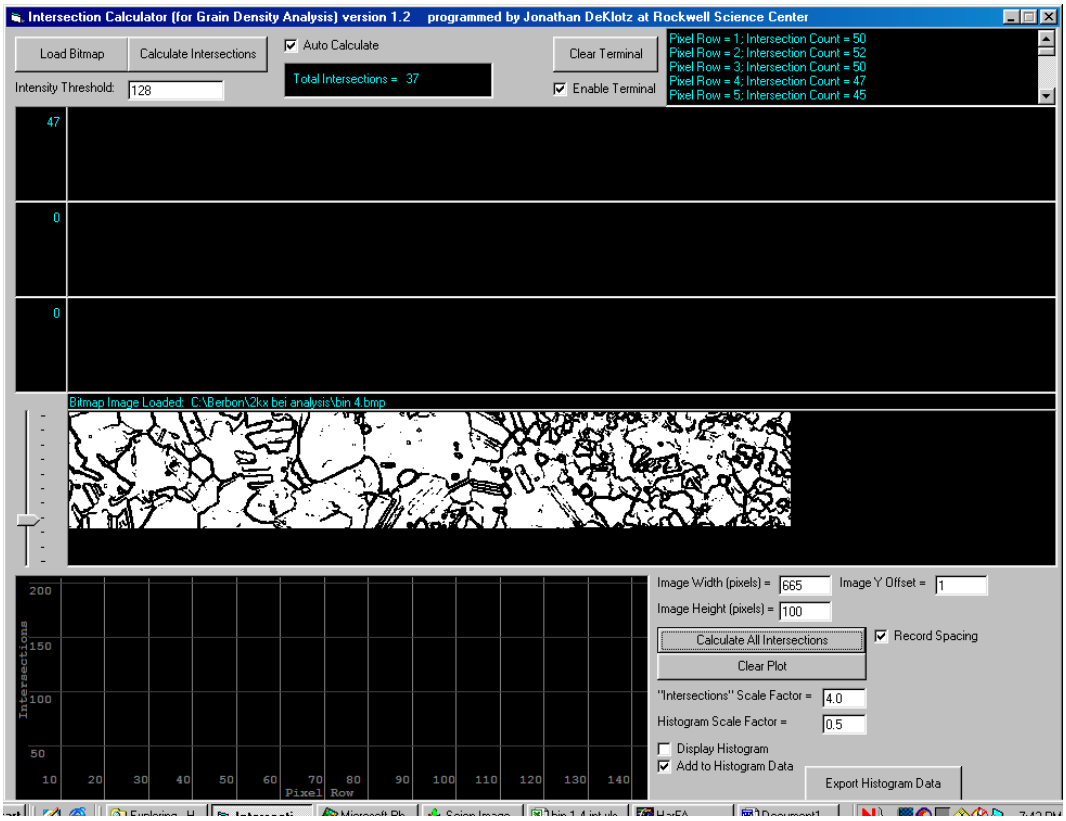

Figure 1 *Analyzing the image in the intersection analyzer to generate f(l).*

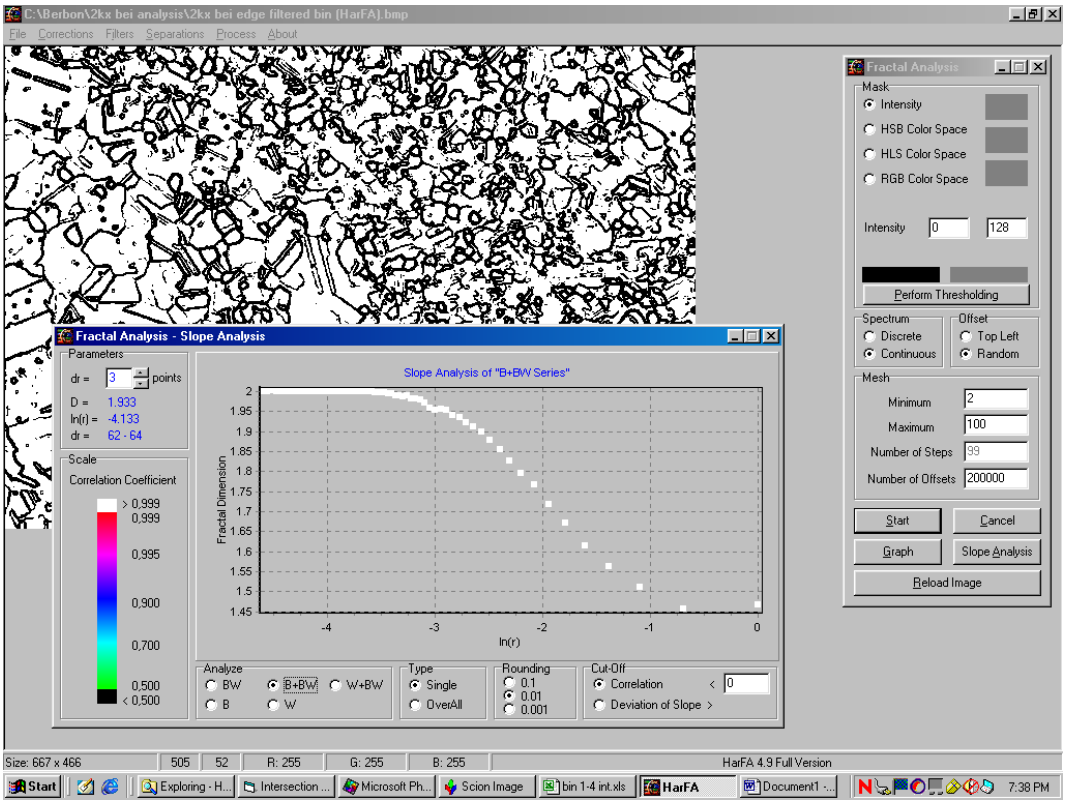

Figure 2 *Analyzing the image in HarFA to extract D(s) and* d*D*/d*s.*

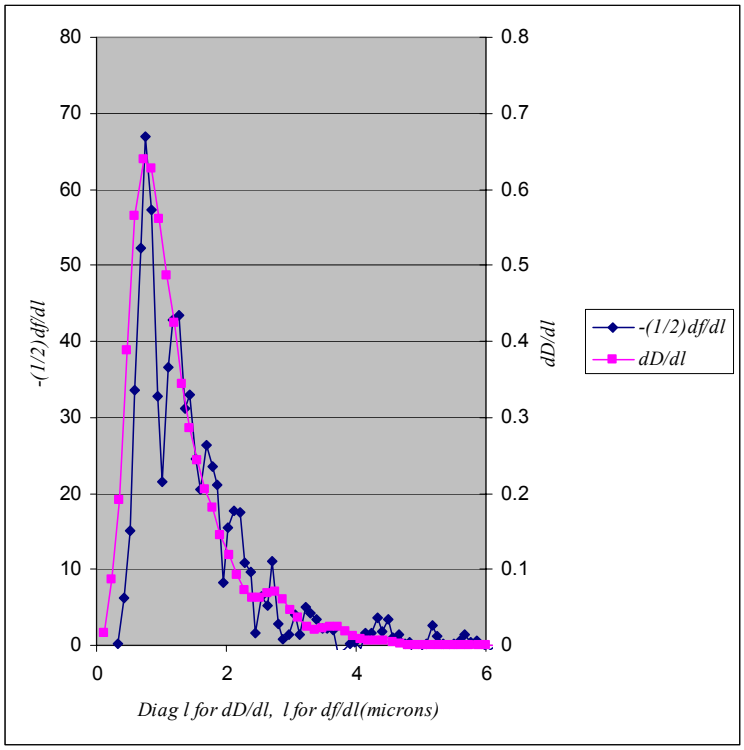

Figure 3 *Comparison of* d*D*/d*l and* d*f*/d*l showing the qualitative agreement. In both, the peaks at 0.76 microns and 2.76 microns match. The df/dl suggests activity at 1.27 microns as well. Those three, and no others, were used to fit gaussians to f(l) using Eqn. 2. Recall from Eqn. 1 that the grain size distribution n(g) = –*Δ*g/q(1) ×* d*f*/d*l.*

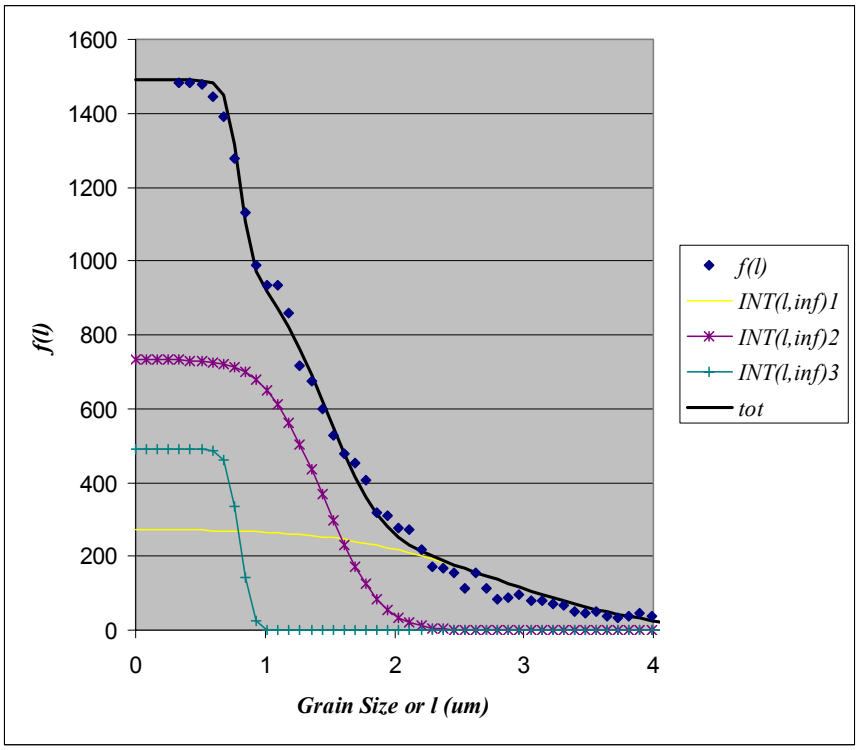

Figure 4 *Fit #1 to the data using Equation 2 and gaussians with peaks from the aforementioned dD/dl and* d*f*/d*l plots.*

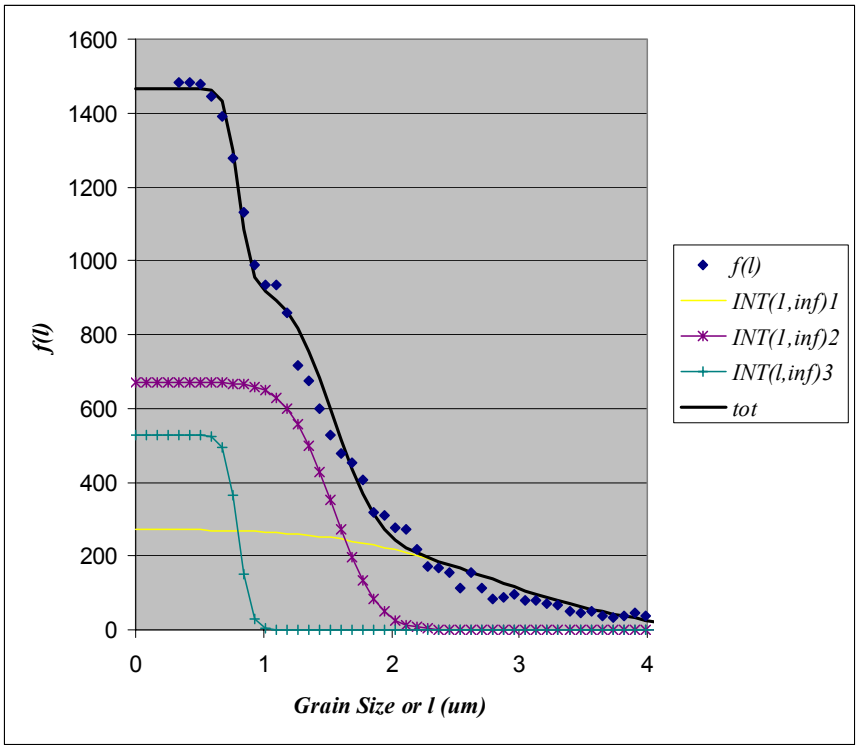

Figure 5 *Fit #2 to the data using Equation 2 and gaussians with peaks from the aforementioned* d*D*/d*l and* d*f*/d*l plots.*

Table 1 *The two sets of gaussians used on the fits.*

Gaussians	*1-#1*	*2-#1*	*3-#1*	*1-#2*	*2-#2*	*3-#2*
$2N_o$	10	70	195	10	80	210
l_o *(um)*	2.756	1.4	.76	2.756	1.5	.76
σ*(um)*	1.3	.5	.12	1.3	.4	.12

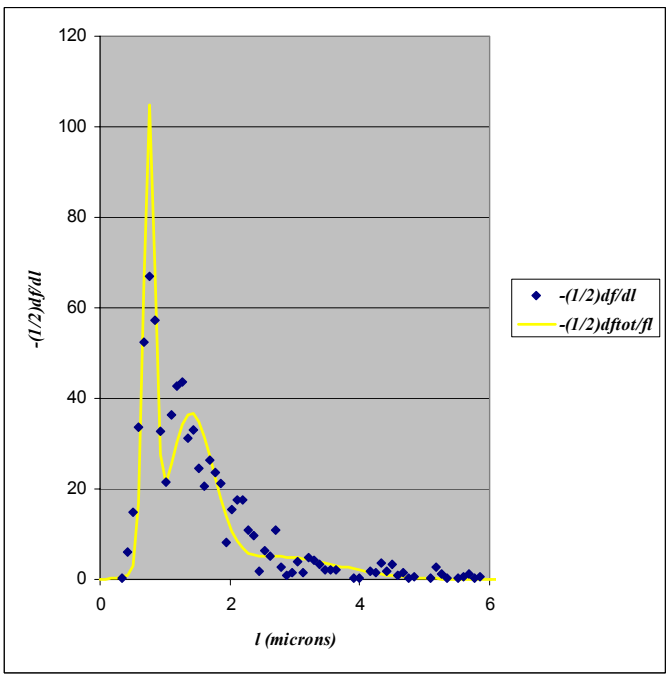

Figure 6 *The yellow line is the derivative of the fit to f*(*l*) *from Eqn 2, gaussian set #1.*

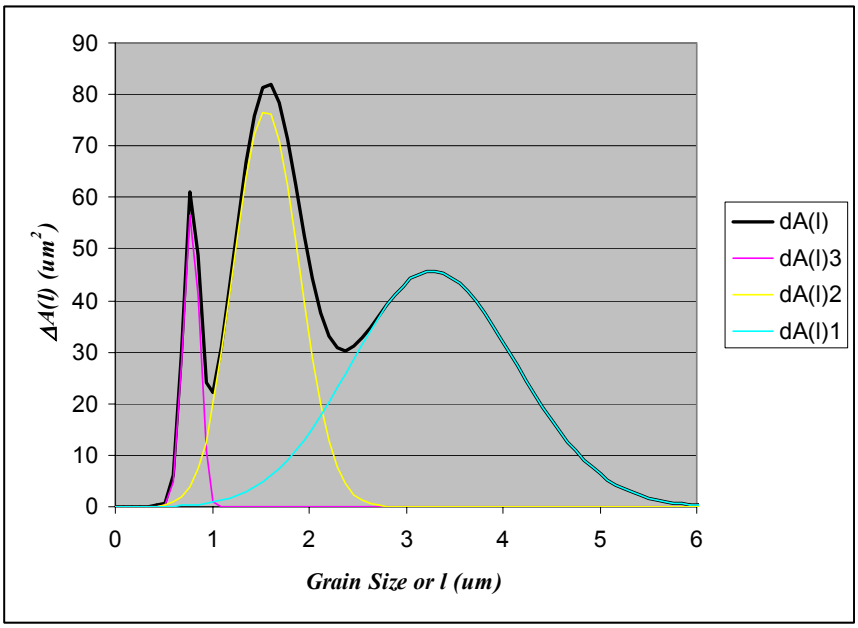

Figure 7 *The gaussians are multiplied by l^2 as per Eqn. 3 to get the areal distribution.*

Table 2 *Relative Areas of Grains in Distribution.*

	gauss#1	*gauss #2*	*gauss #3*
% Area	55.87	37.15	6.96
l_o*(um)*	2.756	1.4	0.76

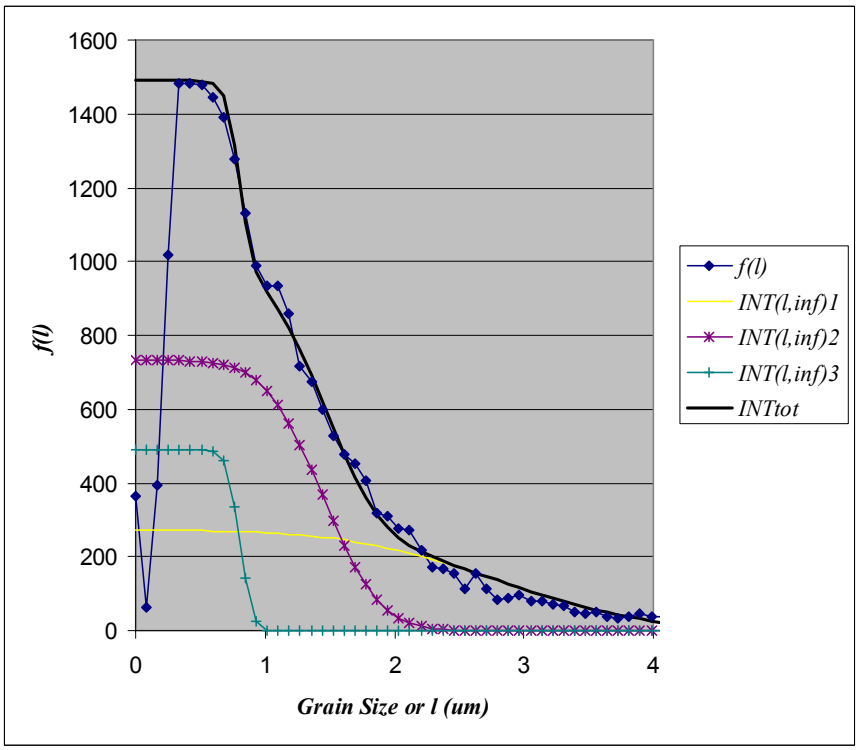

Figure 8 *This chart is a reminder that f(l,O) has grain shape dependence. Note that in the context of Eqn. 1, q(l/g,O)→ 0 for l < 0.25 microns.*

4. Discussion.

We are able to relate the fractal dimension derivative to length spectra from a variation on the secant method. The assumptions to relate the information to grain size distributions (Eqn. 1) are in need of comment, and though they are somewhat artificial, they are very similar to the assumptions that have been used to deal with grain shape in a large body of work on metals. The transformations on *f(l)* are performed to convert it into a representation of a grain size distribution, but it should be understood there are inherent errors. Good fitting to data *f(l)* and *df/dl* is possible from observations on the combined methods.

Consider the following perspective: it is often the case that the only information reported regarding the microstructure of a material is average grain size, sometimes with no mention of how it was determined. The figure actually reported may be the average of gradients or multiple distributions, and the omission of distribution information means that there is a gap in the literature relating material properties to size distributions (note the use of the words *size distributions* in general).

Also, note that emphasis is being put on fitting the *f(l)* with gaussians, with clues about where the gaussians are placed coming from the derivatives of *f(l)* and *D(s)*. This is because there is a lot of existing work on normal microstructures in which the distributions of secant intersection lengths and the average lengths in those studies are referred to as grain size distribution and average grain size.

Although the information generated by the methods in this paper may not be directly relatable to the usual definition of a grain size distribution, what is certain is that as the length scales of interfaces in materials fall through the nanoscale regime, all the intersection lengths in images will fall as well, along with average grain size. The distributions and fitting functions generated in this method offer additional means for standardizing reporting on the structure of polycrystalline materials. The method is fast and can be automated. The distributions derived can be just as easily correlated to physical properties of materials as average grain size.

The two methods under consideration do not show all of the same peaks. The d*D*/d*s* does not have the peak at 1.4 microns, but the d*f*/d*l* does. It is interesting to envision what the specific cases are that could describe the situation when there are fewer intersection lengths *l* counted in the image, yet there can be large amounts of all white box generation of side *l*. The case of harmonics is pictured below, in which boxes of size $s_o/2^m$ are shown for $m = 0$ and $m = 1$. For $s_o/2$ there are no lines of length $s_o/2$ directly associated with the white box generation, as there are for s_o.

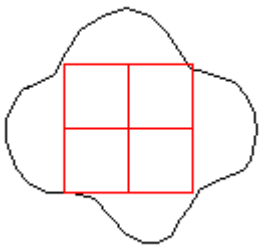

Figure 9 *Haromincs* s_o *(the large box) and* $s_o/2$ *(the quarters).*

The latter is not the case in our image, since the positions of the peaks of the fractal dimension do not follow a harmonic trend, $s = X_o/2^m$.

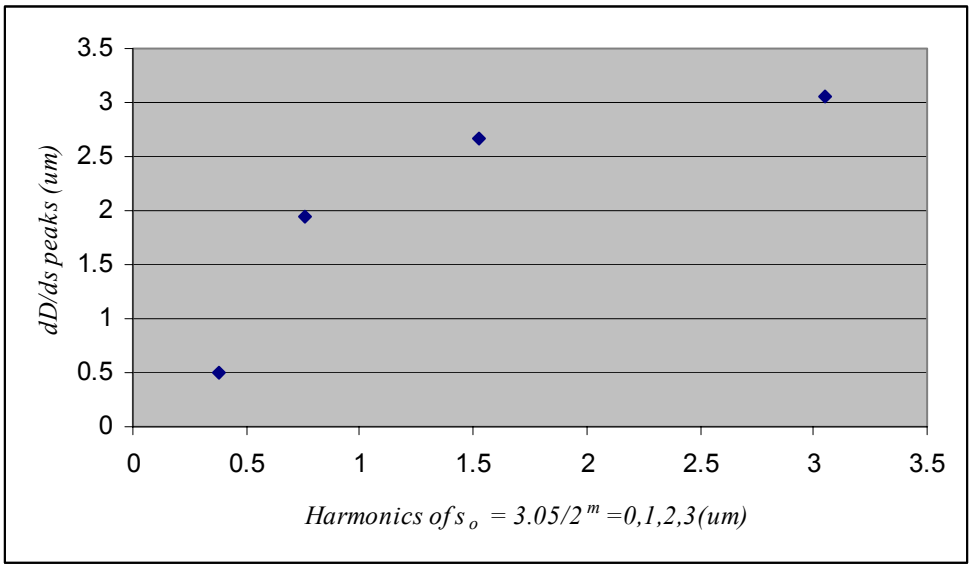

Figure 10 *No harmonic trend is seen for any value of X_o or progression of m, that is, a straight line of a slope of unity is not possible.*

5. Conclusions.

The lineal analysis produces *f*(*l*) which is a cumulative size distribution. The fractal analysis produces *D*(*s*). The positions of peaks in d*f*/d*l*, and d*D*/d*s* corresponding box diagonals give clues about where to place gaussians or other distributions shapes. Using the methods together is necessary, as the peaks in both methods do not always match.

Evaluation of trabecular bone texture changes attributed to aging on the plain radiograph of calcaneus using fractal analysis

Ion Stefan [1], Andrei Prie [1], Radu Badea [2], Constantin Vertan [3]

[1] Emergency Hospital Baia Mare, Traumatology Department, Baia Mare
[2]University of Medicine and Pharmacy "Iuliu Hatieganu" Cluj-Napoca, Medical Imagery
[3]Image Processing and Analysis Laboratory, "Politehnica" University, Bucharest
Corresponding author: Ion Stefan. E-mail: IonStefan@gmx.net

The aim of the study was to determine if fractal analysis of the trabecular structure of the calcaneus, as it appears on the plain lateral radiograph, can detect alterations attributed to aging. Aging is accompanied by changes of trabecular bone structure due to the remodeling process. This process is accelerated in the group of postmenopausal women.

1. Materials and Methods

We analyzed 2 sets of 12 radiographs from two groups of women. The first group with ages between 26 and 38 years (mean age = 33 years), the second with ages between 48 and 65 years (mean age = 56 years)

Radiographs were digitized using a Fujifilm FinePix 2600 Zoom digital camera. The colored images were transformed to grayscale images.

Three ROI were selected on each radiograph. Selection and saving of ROI was done with software CalcaneuPrj (author: Bogdan Ionescu). ROI 1 corresponds to the thalamic region, ROI 2 to Ward's triangle and ROI 3 to the region where the posterior plantar group of trabeculae intersects the thalamic group (*Fig. 1*).

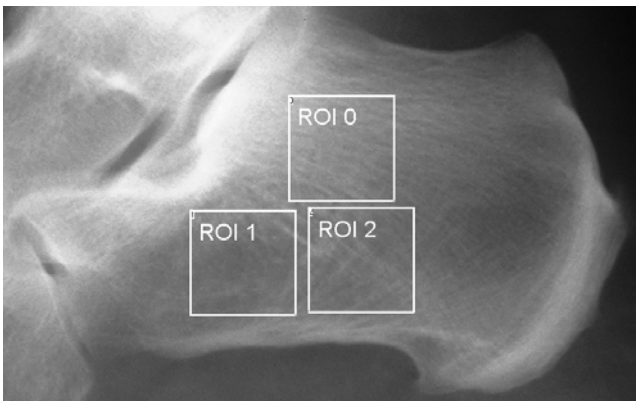

Figure 1 Position of the three ROI

Because there is a brightness gradient due to thickness difference of bone and soft tissue, a dynamic thresholding technique (software: ImageJ; plugin's author: Gary Chinga) was used to segment the images (*Fig. 2,3,4*).

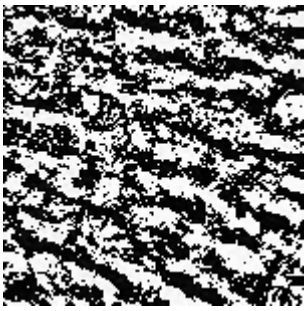

Fig. 2 Segmented ROI 0.

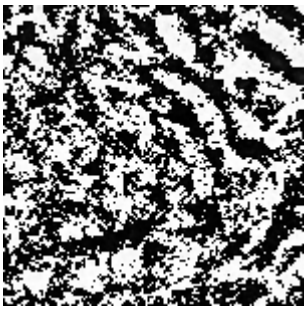

Fig. 3 Segmented ROI 1

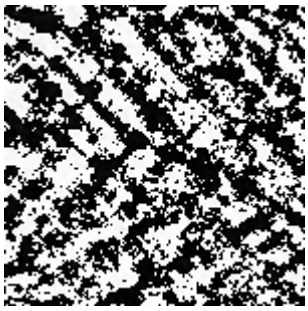

Fig. 4 Segmented ROI 2

The box-counting fractal dimension (BCFD) of each ROI was determined using HarFA 4.9 (authors: Martin Nezadal and Oldrich Zmeskal). Each radiograph was characterized successively by pairs of the 3 parameters. The results for the two sets were represented graphically. The spatial distribution of the points on the graphs was evaluated using a nearest neighbour approach.

2. Results

Table 1 contains BCFD values for the 26-38 years group. Table 2 contains BCFD values for the 48-65 years group

Table 1 BCFD values for the 26-38 years group

Case no.	1	2	3	4	5	6	7	8	9	10	11	12
ROI 0	1,868	1,841	1,871	1,875	1,843	1,863	1,858	1,894	1,866	1,865	1,865	1,870
ROI 1	1,863	1,795	1,869	1,873	1,845	1,858	1,858	1,886	1,887	1,865	1,889	1,876
ROI 2	1,865	1,849	1,882	1,882	1,844	1,865	1,866	1,882	1,875	1,867	1,872	1,886

Table 2 BCFD values for the 48-65 years group

Case no.	13	14	15	16	17	18	19	20	21	22	23	24
ROI 0	1,882	1,885	1,873	1,880	1,904	1,878	1,876	1,899	1,895	1,893	1,894	1,872
ROI 1	1,888	1,898	1,876	1,871	1,899	1,879	1,865	1,898	1,898	1,904	1,903	1,873
ROI 2	1,865	1,887	1,864	1,869	1,881	1,879	1,884	1,892	1,902	1,899	1,905	1,888

The following graphs resulted by plotting BCFD of one ROI against BCFD from another ROI of the same radiograph (*Fig. 5,6,7*).

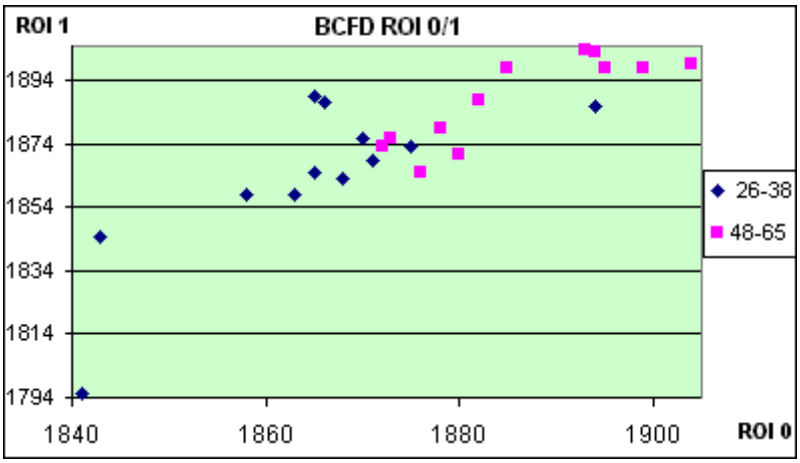

Figure 5 BCFD of ROI 0 plotted against BCFD of ROI 1

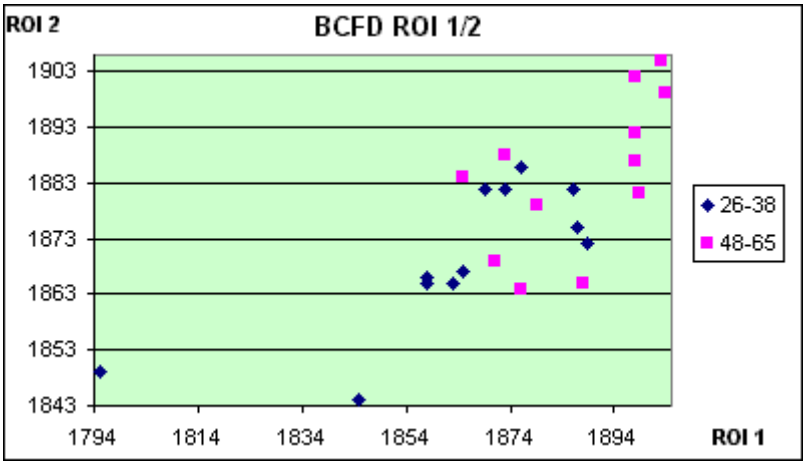

Figure 6 BCFD of ROI 1 plotted against BCFD of ROI 2

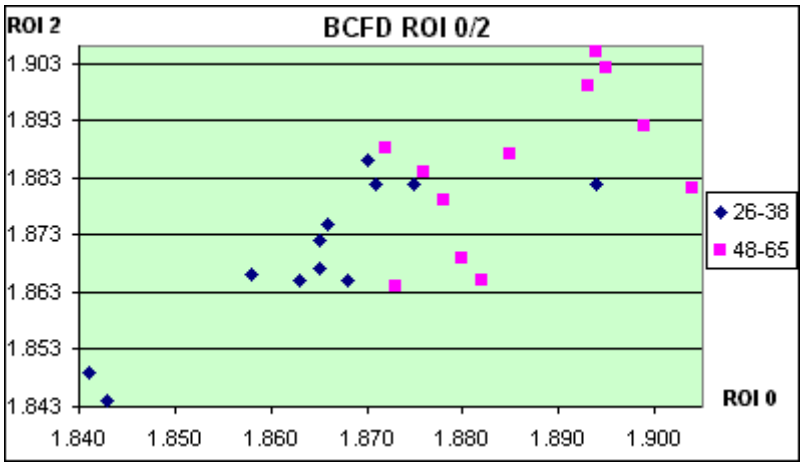

Figure 7 BCFD of ROI 0 plotted against BCFD of ROI 2

Examining these charts it is obvious that for all regions of interest BCFD is higher for the 48-65 group(Fig. 8). A tendency for spatial separation of the points from the two sets is also apparent.

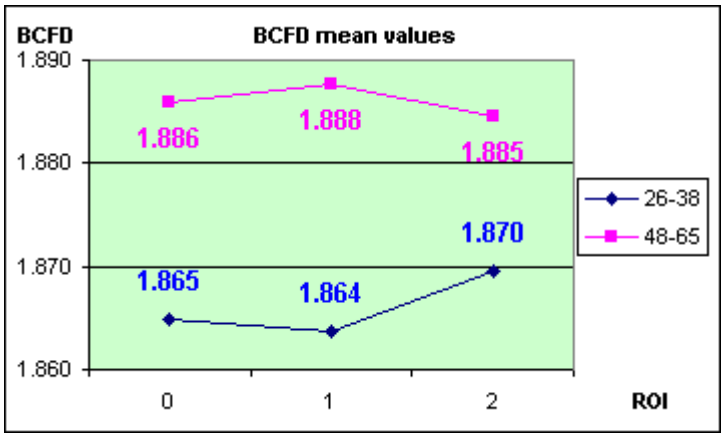

Figure 8 Mean values of BCFD for each ROI and the 2

We tried to quantify the apparent spatial separation of the points corresponding to the two sets of radiographs using a nearest neighbor method. Tesselations of Voronoi were drawn (software: VoronoiPainter; author: Marko Krajnc) (*Fig. 9,10,11*).

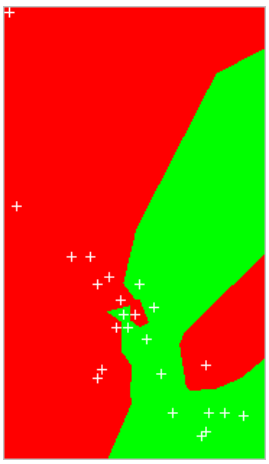

Figure 9 Tesselations of BCFD for ROI 0 plotted against BCFD for ROI 1. Red = 26-38 years

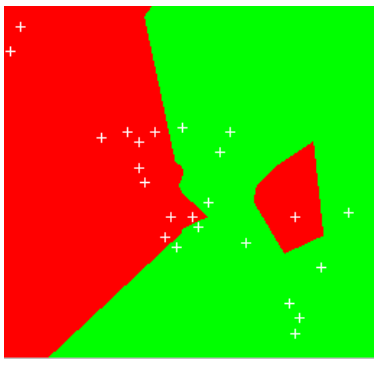

Figure 10 Tesselations of BCFD for ROI 0 plotted against BCFD for ROI 2. Red = 26-38 years group; green = 48-65 years group.

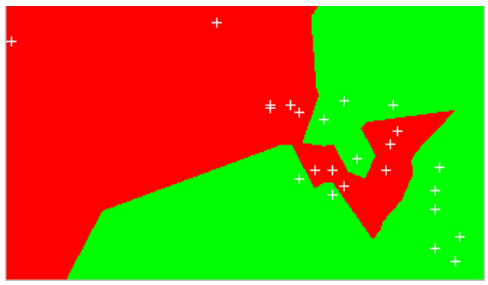

Figure 11 Tesselations of BCFD for ROI 1 plotted against BCFD for ROI 2. Red = 26-38 years group; green = 48-65 years group.

Each point was withdrawn and reintroduced in the tesselation determined by the rest of the points. This operation allowed to categorize a "correct" or "incorrect " positioning of each point (*Fig.12,13*).

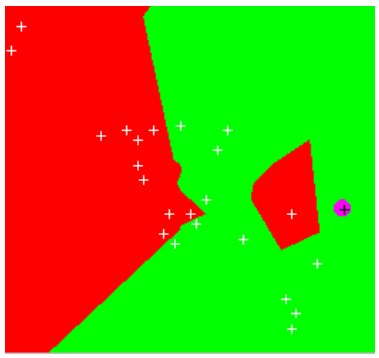

Fig. 12 Marked point will be withdrawn.

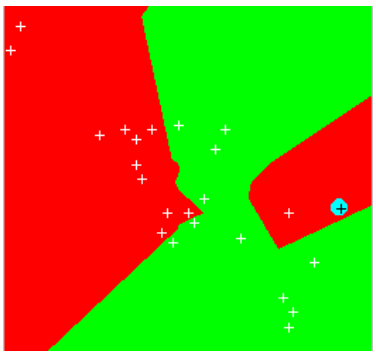

Fig. 13 Aspect of the tesselation after withdrawal of the point. If reintroduced, the point falls into the wrong region.

The correct and incorrect decisions are presented in the tables 3, 4, 5.

Table 3

1	2	3	4	5	6	7	8	9	10	11	12
right	right	wrong	wrong	right	right	right	wrong	right	right	right	wrong
13	14	15	16	17	18	19	20	21	22	23	24
right	right	wrong	wrong	right	right	wrong	right	right	right	right	wrong

Decisions for BCFD of ROI 0 plotted against BCFD of ROI 1: 8 wrong decisions out of 24.

Table 4

1	2	3	4	5	6	7	8	9	10	11	12
right	right	right	wrong	right	right	right	wrong	right	right	right	wrong
13	14	15	16	17	18	19	20	21	22	23	24
right	right	wrong	right	wrong	wrong	wrong	right	right	right	right	wrong

Decisions for BCFD of ROI 0 plotted against BCFD of ROI 2: 8 wrong decisions out of 24.

Table 5

1	2	3	4	5	6	7	8	9	10	11	12
right	right	right	right	right	right	right	right	right	right	right	wrong
13	14	15	16	17	18	19	20	21	22	23	24
wrong	right	right	wrong	right	wrong	wrong	right	right	right	right	wrong

Decisions for BCFD of ROI 1 plotted against BCFD of ROI 2: 7 wrong decisions out of 24.

3. Discussion and conclusions

A radiograph of the calcaneus is very often solicited in outpatient practice for various reasons. It would be very challenging to try to extract as much information as possible from this acquisition.

Fractal analysis of radiographs of calcaneus offers information about the complexity of the trabecular pattern. In this study we tried to find out, to what extent, fractal analysis alone can distinguish changes of the trabecular pattern between two groups separated by a single criterion – age. We assumed that analysing more regions of interest and correlating the results would enhance the possibility to separate the two groups. It would add probably information related to the heterogenity of

trabecular structure. We proposed also a nearest neighbor classification algorithm. The results we obtained may represent the training examples for further query instances.

Our study shows that fractal dimension of the trabecular bone increases with age. Similar result are reported by Lespessailles et al., 2002. Other studies concluded that FD is higher in subjects with lower bone mass, history of osteoporotic fractures (Bollen et al.,2001). Subjecting a radiograph to the described algorithm, we have 2/3-3/4 chances to find the correct answer about age group. Errors are more often in the elderly group, probably due to more dispersed values of BCFD.

4. References

[1] Bollen A-M, Taguchi A, Hujoel PP,Hollender LG, Fractal dimension on dental radiographs, Dentomaxillofac Radiol (2001) 30, 270 – 275

[2] Lespessailles E, Poupon S, Niamane R, Loiseau-Peres S, Derommelaere G, Harba R, Courteix D, Benhamou CL., Fractal analysis of trabecular bone texture on calcaneus radiographs: effects of age, time since menopause and hormone replacement therapy.Osteoporos Int 2002 May;13(5):366-72

Cranial Sutures as the Fractal Coastlines

Janusz Skrzat, Jerzy Walocha

Department of Anatomy, Collegium Medicum, Jagiellonian University
Kopernika 12
31-034 Cracow, Poland
jskrzat@poczta.onet.pl

The cranial bones are usually joined by complex osseous projections, which precisely interlock. The image of such connections between two cranial bones resembles outline of the coastline with many bays. The contour of these lines may vary from slightly convoluted lines to complex patterns that resemble coastlines with many peninsulas and bays [4]. When a selected segment of cranial suture is analyzed, one may perceive similar property of curviness. This character is typical for fractal structures and it is termed as self-similarity. However, the cranial sutures are not typical fractals and self-similar properties are limited to 2-3 orders of scaling but they yield fractal dimension, which differs with kinds of suture-lines [5]. In this respect fractal dimension becomes a useful index for determining sutural morphology in terms of its complexity.

The cranial sutures can be modeled as lines that have been deformed in a particular way, demonstrating interfingering and lateral excursions [3]. Possible formation of cranial suture contour could be explained by the random midpoint displacement, which is widely used to depict fractal coastlines or fractal landscapes [6, 9]. Here are the rules of this algorithm and its initial steps are presented in the *figure 1*.

1. Make a straight line
2. Grab the middle of the line and move to one of the side (eg. right or left) by a random amount.
3. Then take one of the two new segments and drag the middle point toward the right or left side
4. Recursively repeat this process with smaller segments
5. Stop the process when the individual segments are too short to be worth to be splitting.

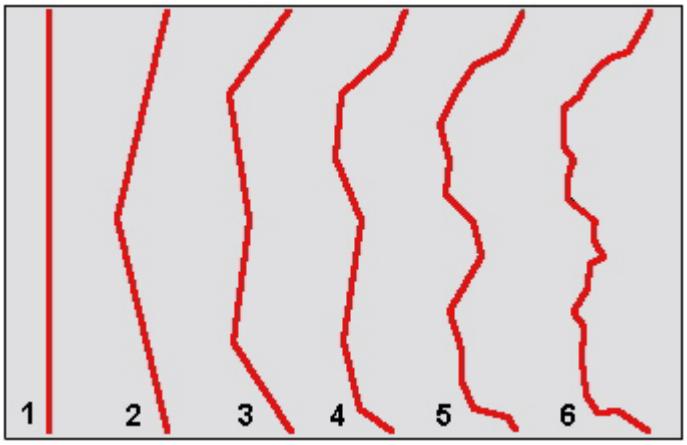

Figure 1 Six steps of the random midpoint displacement method applied to the line

The method starts with a simple line and recursively adds random details, which number of elements is equal 2^n, where n is the step number. Each step produces twice as many segments of the line with random displacement as the step before. A brief mathematical description of the random midpoint displacement algorithm can be formulated in the following way:

Assume that values $X(0) = 0$ and $X(1)$ are given. $X(1)$ is obtained as a Gausian random number. The next step refers to the partition the interval [0,1] into two subintervals: [0, 1/2], [1/2, 1], and the $X(1/2)$ is defined as the mean of $X(0)$ + i(1) plus a displacement D as the Gaussian. The big subdivision gets a big displacement, while the smaller subdivisions get smaller displacement, what makes the line fractally. The initial three steps of the midpoint displacement algorithm are presented as:

$$X(1/2) = [X(0) + X(1)]/2 + D_1$$
$$X(1/4) = [X(0) + X(1/2)]/2 + D_2$$
$$X(3/4) = [X(1/2) + X(1)]/2 + D_3$$

This process is continued with displacements D_n having variance Δ_n^2. In the result, the baseline is displaced by the fractal line, which looks like a silhouette of the coastline [8].

The entire process of the random midpoint displacement is based on randomly generated numbers and usually controlled by three variables: the number of iterations, roughness and the number of initial points. Here are the definitions of these variables [1, 10]:

- Random Number – are generated by the computer uses a function called "random number generator." The random number generator follows a normal random distribution function, with mean $\mu = 0$ and variance $\sigma^2 = 1$. A different distribution function, or a different mean or variance would generate different random numbers, and thus different coastlines.
- Roughness – is the factor by which the perturbations are reduced on each iteration. Higher values result in a smoother surface while lower values result in a rougher surface. Roughness (R) is also related to scale (S) by the exponential relationship: $S = (1/2)^R$. Thus, a larger scale means a smaller roughness value, and a rougher landscape.
- Initial points – points where the coastline is broken during its formation. They are specified to provide some degree of control over the appearance of the coastline. Usually, the number of initial points may very from 2 to 5.
- Number of iterations – indicate how many times the process of the midpoint displacement is repeated. At n iterations, there will be 2^n segments of the line. The larger number of iterations means the smaller parts on the initial line and it results in the increase of the polyline segments.

The procedure of random midpoint displacement can be performed by software and the results are visible on the computer screen. The example of such software can be found in the web [2, 6,10].

The appearance of the generated coastlines resembles the outlines of the cranial bones, which are joined by the sutures. In other words, the algorithm of random midpoint displacement becomes a model of sutural pattern formation (compare *figure 2*, *figure 3* and *figure 4*).

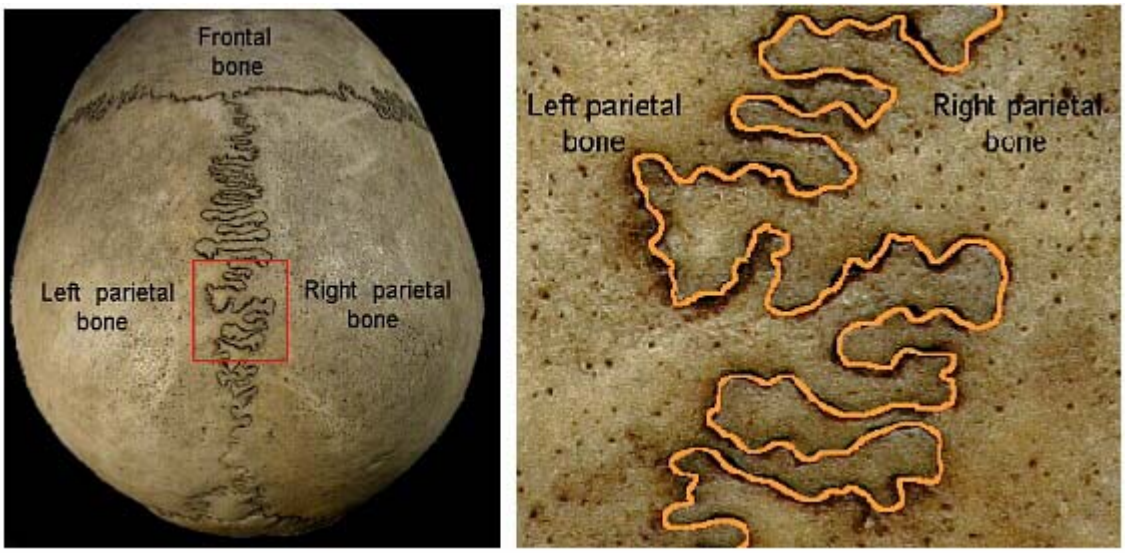

Figure 2 Image of the cranial vault with demarcated sagittal suture that joins two parietal bones. Red rectangle marks the region of interest (ROI), which is magnified in the opposite picture. The orange line represents suture contour or the border between two parietal bones joined by the suture.

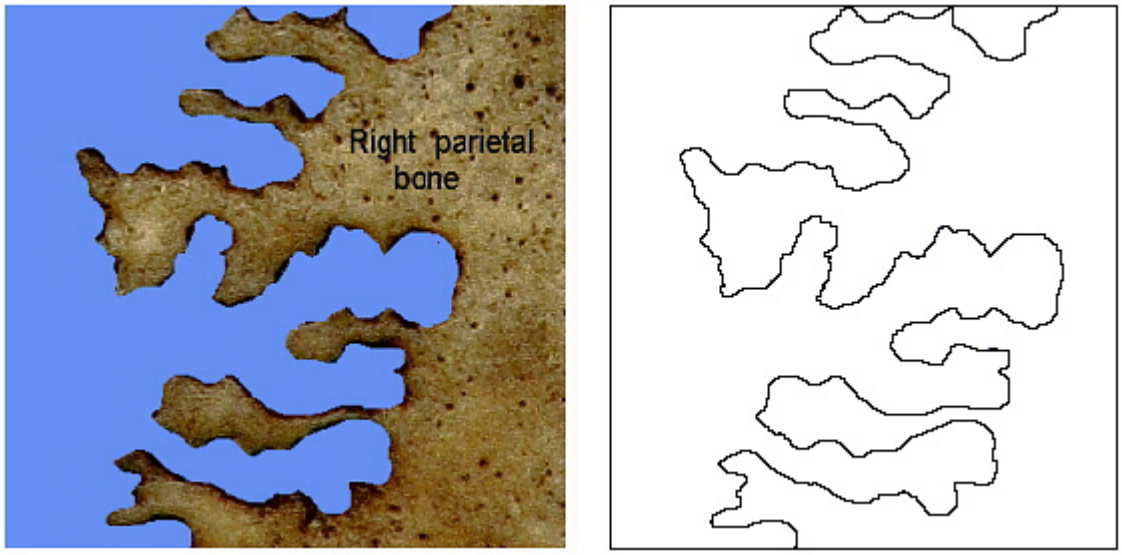

Figure 3. The edge of the right parietal bone within the ROI, (left parietal bone is removed). The isolated one pixel line as a coastline represents pattern of cranial suture

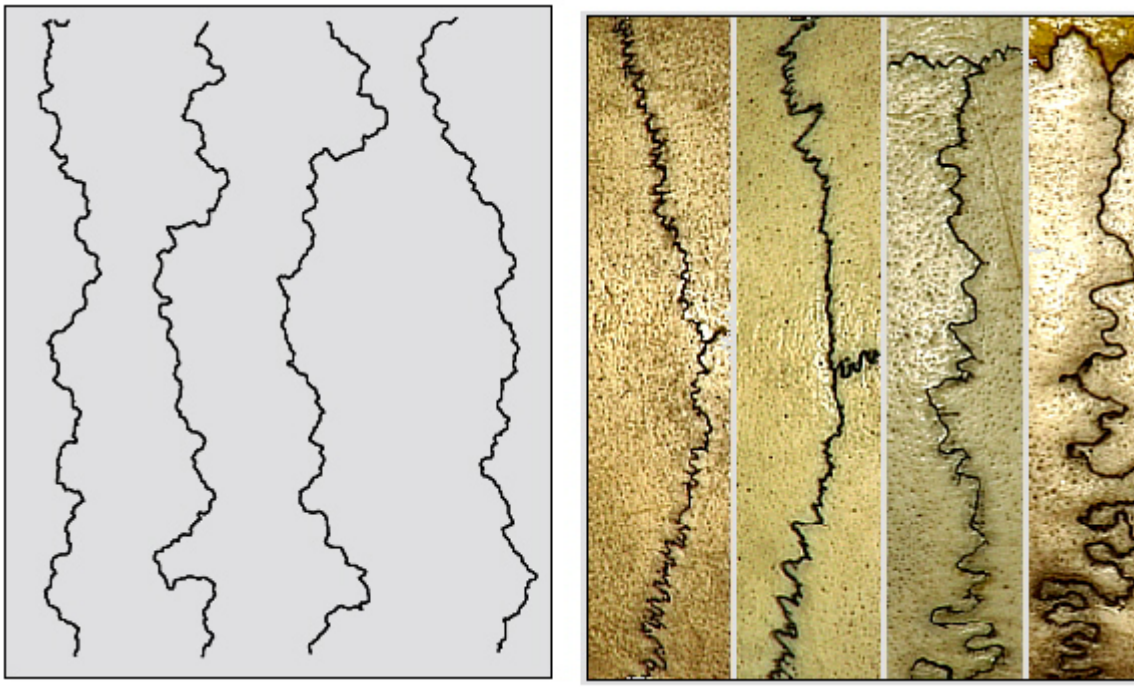

a *b*

Figure 4. Examples of computer generated coastlines (a) using random midpoint displacement algorithm and natural patterns of cranial sutures (b)

Computer generated curves were compared to the curves of real cranial sutures by means of fractal dimension, which was measured as the box-counting dimension with implementation the HarFA software [7]. The box-counting dimension (D_F) is defined as:

$$D_F = \lim_{\varepsilon \to 0} \frac{\log N(\varepsilon)}{\log (1/\varepsilon)},$$

where: $N(\varepsilon)$ is the number of boxes of side-length ε needed to cover the analysed object.

The box-counting dimensions of the computer-generated coastlines were compared to the fractal dimensions of the natural cranial sutures. As the result we got similar values of fractal dimensions ranging from 1.10 – 1.40 and moreover these values remain consistent with the fractal dimensions calculated by other researchers [3, 5, 11]. This indicates those computer-generated patterns and cranial sutures show similar complexity and because of their appearance and character they were regarded to belong to the same class of geometrical objects termed as fractal structures.

The proposed coastline model of the cranial suture is a simplification as it represents only the outline of the edge of the cranial bone and not entire surface, which faces with the opposing bone. However, this algorithm can be extended into 2D structures and then it will become more appropriate for modeling surfaces of the cranial bones, which contact within the suture. Moreover, such mechanism of structure formation, in the case of cranial suture might be possible in certain range of scale and it does not have to be universal for all sutures. Certainly, the suture morphogenesis is highly complex process, which is dictated by various factors and their interactions are not based on singular algorithm. The midpoint displacement method produces natural-like object patterns, which appearance corresponds to cranial suture morphology. However, sutures, which are obtained with random midpoint displacement algorithm sometimes, are not ideal representations of the real cranial suture because of produced unnatural features. Therefore their appearance depends significantly on relationship between values of three parameters: roughness, the number of initial points and the number of iterations. Nevertheless, this method models geometrical construction, which might be attributed to the cranial sutures. Such a model may help to understand mechanisms of changes in the bone edges configuration when they form suture during skull development. This algorithm shows also clearly the idea around implication of fractal geometry not only to describe contours of the cranial sutures but also to explain hypothetical mechanism that may be engaged in suture morphogenesis.

References

[1] Bourke P. Fractal Landscapes, 1991. http://astronomy.swim.edu.au/~pbourke/terrain/frachill
[2] Hahn P. Random Midpoint Displacement Algorithm, 1997. http://www2.vo.lu/homepages/phahn/fractals/program2.htm
[3] Hartwig W.C. Fractal analysis of sagittal suture morphology. J Morphol, 210: 289-290. 1991
[4] Long C.A. Intricate sutures as fractal curves. J. Morphol. 185: 285–295. 1985
[5] Long C.A., Long JE. Fractal dimensions of cranial sutures and waveforms. Acta Anat. 145(3): 201–206. 1992
[6] Martz P. Generating Random Fractal Terrain, 1987 http://www.gameprogrammer.com/fractal.html#midpoint
[7] Nezadal M, Zmeskal O. HarFA, Harmonic and Fractal Image Analyser, webpage: http://www.fch.vutbr.cz/lectures/imagesci, 2001.
[8] Peitgen H.O., Jurgens H., Saupe D. Fractals for classroom. Part 1: Introduction to fractals and chaos. Springer-Verlag, New York. 1992.
[9] Saupe. D. Fractals. http://www.inf.uni-konstanz.de/cgip/bib/files/Saupe93.pdf
[10] Tsai M.G. Fractal Landscapes, 2003. http://www.math.toronto.edu/courses/335/projects/tsai/report1.htm
[11] Yu J.C., Wright R.L., Williamson M.A., Braselton J.P., Abell M. - A fractal analysis of human cranial sutures. Cleft Palate Craniofac J. 40(4): 409-415. 2003

The Use of Fractal Dimension in Arts Analysis

Peter Gerl, Carola Schönlieb, Kung Chieh Wang

Institut für Mathematik, Hellbrunnerstr. 34, A-5020 Salzburg, Austria
peter.gerl@sbg.ac.at, carola.schoenlieb@sbg.ac.at, kung.wang@sbg.ac.at

Abstract

The fractal dimension is a measure for the coarseness of objects and textures. This property can be assigned to graylevel images to get a measure for the coarseness of a texture in an image, [2]. The theme of this article is the application of fractal dimension to arts analysis. Considering 7 artists, everyone represented by about 18 images, we searched for qualified description parameters for the painters characteristics. We evaluated among other feature values 3 different types of fractal dimension, namely capacity (or box counting) dimension, information dimension and correlation dimension, [3]. With a special feature selection algorithm the best features for the classification of the images with respect to the painter were evaluated, [5]. The fractal dimension turned out to be under the best features. In the following the computation of the fractal dimension, our classification task and a few results are discussed.

1. Fractal Dimension

We want to define the notion of a dimension of an image. From the mathematical point of view the best way would be to take the Hausdorff dimension [1], since this exists for all (bounded) subsets of a metric space, and an image is a bounded subset of Euclidean 3–dimensional space (at least a graylevel image). But the Hausdorff dimension has a complicated definition and it is by no means easy to calculate it. Therefore simpler versions for the notion of a dimension were suggested. A very useful notion goes back to A. Renyi [4], the generalized q–dimension. We will start with one version of this q{dimension and will specialise then to its calculation for images.

1.1. The generalized *q*–dimension of A. Renyi

Let A be a bounded, measurable subset of the 3-dimensional space $\Re^3$. For $\varepsilon > 0$ we consider a lattice of cubes of side length ε in $\Re^3$ call these cubes C_1; C_2; .... Then let

$$p_i(\varepsilon) := \frac{measure(A \cap C_i)}{measure(A)},$$

(this gives a probability measure on A. To be more precise $p_i(\varepsilon) :=$ Prob (a point of A lies in C_i)).

Definition 1.1 *For $q \geq 0$ the generalized q–dimension of A is defined as*

$$D_q(A) := \lim_{\varepsilon \to 0} \frac{1}{q-1} \cdot \frac{\ln \sum_i p_i(\varepsilon)^q}{\ln \varepsilon},$$

(if the limit exists).

Remark 1.2 *It can be shown that $D_q(A)$ is well defined, i.e. independent of the choice of the cubic lattice (origin and direction of axes) and that $D_q(A)$ is a decreasing function with respect to q. Furthermore for $A \subset \Re^3$ one has $0 \leq D_q(A) \leq 3$.*

Important special cases are:

***q* = 0**: Here we use the convention that $0^0 = 0$. Then $\sum (p_i(\varepsilon))^0 =$ (number of cubes ofside length ε that contain a part of positive measure from A) $= N(A, \varepsilon)$.

So we get from the definition above

$$D_0(A) = \lim_{\varepsilon\to 0}\frac{1}{q-1}\cdot\frac{\ln\sum_i N(A,\varepsilon)}{\ln 1/\varepsilon} =: D_C(A),$$

which is usually called the *fractal dimension* of A (or also capacity dimension of A).

***q* = 2**: The definition gives

$$D_2(A) := \lim_{\varepsilon\to 0}\frac{\ln\sum_i p_i(\varepsilon)^2}{\ln\varepsilon} =: D_{corr}(A),$$

the so called *correlation dimension* of A. The expression in the nominator has a nice interpretation, namely $\sum(p_i(\varepsilon))^2$ =Prob (2 points of A lie in the same cube C_i).

***q* = 1**: In this case we have to be careful since for $q = 1$ the nominator and the denominator in the definition of $D_q(A)$ vanish (apply de l'Hospital).

$$D_1(A) := \lim_{\varepsilon\to 0}\frac{1}{\ln\varepsilon}\lim_{q\to 1}\frac{\ln\sum_i p_i(\varepsilon)^q}{q-1} = \lim_{\varepsilon\to 0}\frac{\ln\sum_i p_i(\varepsilon)\ln p_i(\varepsilon)}{\ln\varepsilon},$$

which is generally called the information dimension of A (since the nominator corresponds to the entropy, which is a measure for information).

1.2. Practical calculation of the dimension of an image

An image is a finite set of points (= pixels with certain grey values). Unfortunately one can easily show:

$$D_q(\text{finite set}) = 0,$$

So the above definitions cannot be applied directly, since the value 0 for a dimension is not very interesting. Taking another interpretation of a pixel as a square of side length 1 (say) then the limit $\varepsilon \to 0$ makes no sense (ε should be ≥ 1 in this case). Therefore we write the definition for $D_q(A)$ in the following way:

$$D_q = D_q(A) = \frac{1}{q-1}\frac{\ln\sum_i p_i(\varepsilon)^q}{\ln\varepsilon} + \frac{\ln(1/r)}{(q-1)\ln\varepsilon},$$

(where $r = r(A,\varepsilon)$ is an error term). Multiplying with the denominator gives

$$D_q(q-1)\ln\varepsilon = \ln\sum_i p_i(\varepsilon)^q + \ln(1/r),$$

or if we write $x_c = (q-1)\ln\varepsilon$; $y_c = \ln\sum_i p_i(\varepsilon)^q$, we get

$$y_c = D_q x_c + \ln r.$$

This is the equation of a straight line (in a logarithmic coordinate system) with respect to a fixed lattice of squares or cubes and we are interested into its slope D_q. Practically we choose several values for ε, calculate (from the image A) the probabilities

$$p_i(\varepsilon) = \frac{\#(\text{pixels of } A \text{ in } C_i)}{\#(\text{pixels of } A)},$$

and get for each $\varepsilon > 0$ a point $(x_\varepsilon, y_\varepsilon)$. The slope of the regression line defined by these points gives finally the q–dimension $D_q(A)$.

2. Results

In the following table 20 sample images of 5 different painters are shown and the respective fractal dimensions are listed. Values of the capacity dimension and information dimension of the graylevel version of the images (capdim gray, infdim gray) and the capacity dimension of the binary version (capdim bin) are presented. To obtain the anonymity of the artists, we used acronyms instead of their names.

painter bg			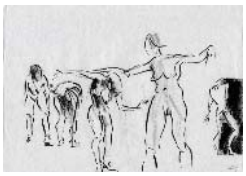	
capdim gray	2.246206	2.091211	2.270820	2.203044
infdim gray	2.281946	2.082100	2.278741	2.241939
capdim bin	1.525424	1.574814	1.674945	1.430831
painter mk			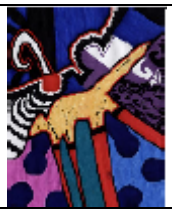	
capdim gray	2.227004	2.237732	2.250339	2.225809
infdim gray	2.182206	2.193382	2.214684	2.165344
capdim bin	1.990236	2.050675	2.012956	1.976064
painter if				
capdim gray	2.243127	2.234009	2.229157	2.221351
infdim gray	2.223151	2.205055	2.189209	2.198305
capdim bin	1.814990	1.797485	1.943745	1.705103
painter ve				
capdim gray	2.229848	2.284704	2.237109	2.283854
infdim gray	2.181884	2.264767	2.221189	2.266364
capdim bin	1.915681	1.850409	1.797892	1.910826
painter wi	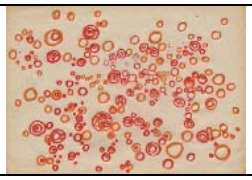	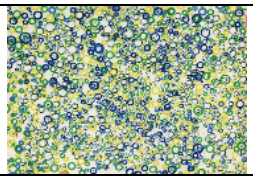		
capdim gray	2.299416	2.368323	2.327271	2.335588
infdim gray	2.272672	2.346169	2.290355	2.355060
capdim bin	1.799837	1.969536	1.983552	1.901535

3. Feature Selection and Image Classification

In our method we use first and second order statistical data to build a feature-space representation for various painters. We combined up to five features and obtained for each feature combination a feature-space which is divided into separate classes representing our painters. In order to extract the best feature combination, we computed the distances of the feature values of each image of a painter to

the mean values, the centre of each class. We chose the Mahalanobis distance as our probabilistic distance measure. Afterwards, we noticed the class to which each feature vector (representing an image) of a painter has minimal distance. Of course, the classification is correct if the feature vector, the image, has minimal distance to its painter. Thus we obtain the best feature combination for the maximum classification rate.

With these best features we try to identify the painter of an unseen image. To improve the classification results we cluster pictures of the painters before classification with respect to different styles, see [5].

For illustration we consider 7 painters. Every painter is represented by 16 to 20 images. As an example we tried to classify these images in a 4{dimensional feature space. In the following table a few results for the percentage of the correct classified pictures from a set of 128 pictures are shown. Values of the capacity dimension of the graylevel version of the images (capdim gray) and the capacity dimension of the binary version (capdim bin) are used as well as statistics, like entropy, mean and variance, of the graylevel distribution in the hue image (hue entropy, hue mean, hue variance).

feature1	feature2	feature3	feature4	percentage of correct classified pictures
capdim bin	capdim gray	hue entropy	hue variance	75 percent
capdim bin	capdim gray	hue mean	hue variance	80 percent
capdim bin	capdim gray	hue entropy	hue mean	70 percent

4. References

[1] Herbert Federer. Geometric measure theory. Repr. of the 1969 ed. Classics in Mathematics. Berlin: Springer-Verlag. xvi, 680 p. DM 59.00; S 430.70; sFr 57.00, 1996.

[2] J. M. Keller, S. Chen, and R. M. Crownover. Texture description and segmentation through fractal geometry. 45:150, 1989.

[3] Pentland. Fractal-based description of natural scenes. pages 661–674, 1984.

[4] A. Renyi. Wahrscheinlichkeitsrechnung. Mit einem Anhang über Informationstheorie. 5. Au. Hochschulbücher für Mathematik, Band 54. Berlin: VEB Deutscher Verlag der Wissenschaften. XI, 547 S., 26 Abb. M 64.00 , 1977.

[5] C. Schoenlieb and K. C. Wang. Feature selection and clustering in arts analysis. pages pp. 25–31, 2003.

Fractal Analysis in epigenetic differentiation of leukemic cells

Eduardo Tejera[1], Nayrim Brizuela[1], Jacques Rieumont[1], José M. Nieto-Villar[1,2]

[1]Department of Physical-Chemistry, Chemistry Faculty, Ave. Zapata & G, [2]"H. Poincaré" Complex Systems Division, Havana University, Havana 10400 Cuba,
nieto@fq.uh.cu

Keywords

fractal analysis, box counting dimension, epigenetic, differentiation, leukemic cells

1. Introduction

This communication describes the application of fractal analysis to epigenetic suppression of malignancy as a potential tool for diagnostic and prognostic purposes. Using the fractal dimension, we found that the complexity of malignant cells is lower in comparison with non-malignant ones.

Usually, the structure of an object can be described utilizing tools of common geometry. A square, for example, can be described by the measure of its sides. However, "complicated" objects, particularly naturally occurring objects such as clouds, mountains, and coastlines, do not apparently appear as a sum of triangles and lines. Such objects are better described using fractal geometry. Fractal geometry has been known as a mathematical concept for many years and was introduced by B. Mandelbrot [1]. Its tools were applied successfully to characterize irregularly shaped and complex figures by a mathematical value wherever Euclidean geometry fails. One of the advantages of fractal analysis is the ability to quantify the irregularity and complexity of objects with a measurable value, which is called the fractal dimension. The fractal dimension can be determined using the box-counting method [2]. Fractal analysis techniques are common tools in physics and image processing.

Fractal geometric analysis, using such tools as fractal dimensions, is thus a more valid method of quantification and is more likely to provide discrimination between different types of fractal objects. In the field of pathology [3], fractal geometry has proved its utility in particular in cancer research [4], such as in endometrial carcinoma [5], in breast cancer [6] and tumour growth [7]. In view of the amazing growth in the understanding of the fractal complexity of the cancer mechanisms, most researches are carried out by measuring the fractal dimension (FD) of different cancer cells or tumour growth. But nothing has been said in relation to the reverse processes, the epigenetic suppression of malignancy. Recently, Lotem and [8] have found that there are Myeloid leukemic cells that can be induced by adding different cytokines including IL-6 to differentiate to non-dividing mature granulocytes and/or macrophages.

2. Results

We applied a fractal dimension analysis, in particular box-counting dimension [9] to epigenetic differentiation of leukemic cells. We found that a significantly higher architecture complexity was noted for non-malignant cells during different stages in differentiation to granulocytes (FD = 1,332; 1,260; 1.209, *Figures 1b,c,d*) in comparison with myeloid leukemic cell, (FD = 1.018, *Figure 1a*).

As it is shown, the complexity of the non-malignant cells is higher than in the malignant one in epigenetic suppression of malignancy by inducing differentiation bypasses the genetic abnormalities in tumour cells. As a fact, this finding corresponds to a general regularity in the biological systems [10].

In summary, fractal analysis applied to epigenetic differentiation of leukemic cells show promise as useful measure of these complex processes. Furthermore, it may provide an additional tool to prognostic information as well as to shed light on the evolution of tumour cells toward the epigenetically reprogrammed to a non-malignant phenotype cells.

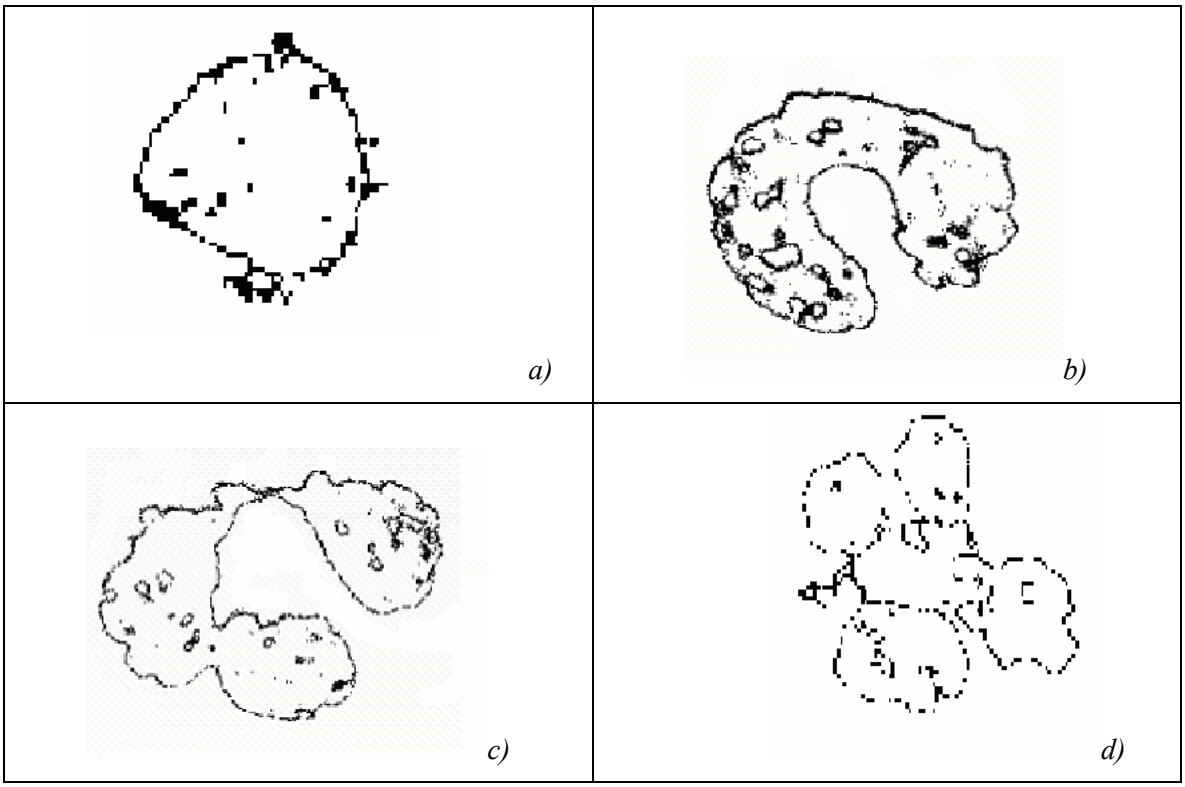

Figure 1 Epigenetic differentiation of genetically abnormal myeloid leukemic cells to non-malignant granulocytes by IL-6: Black/white representation of with a grey level threshold set at: (a) leukemic cell (50-100); stages in differentiation to granulocytes b (100-150), c (94-136), d (50-100).

3. Financial Disclosure

The authors have no connection to any companies or products mentioned in this letter.

4. References

[1] Mandelbrot BB: The Fractal Geometry of Nature, 3rd ed. New York, Freeman, 1983.

[2] Peitgen H-O, Jürgens H, Saupe D: Fractals for the Classroom, Parts 1 and 2, 1st ed. New York, Springer, 1992.

[3] Ary L. Goldberger, *et al.*, Fractal dynamics in physiology: Alterations with disease and aging PNAS, 2002; vol. 99, 2466–2472.

[4] Baish, J. W., and Jain, R. K. Fractals and cancer. Cancer Res., 2000; *60,* 3683–3688.

[5] Dey P, Rajesh L. Fractal dimension in endometrial carcinoma, Anal Quant Cytol Histol. 2004; 26(2):113-6.

[6] Sedivy, R., Thurner, S., *et al.* Short-term rhythmic proliferation of human breast cancer cell lines: surface effects and fractal growth patterns, J Pathol., 2002; **197**(2), 163-9.

[7] Bru´, A., Pastor, J. M., Fernaud, I., Melle, S., and Bru´, I., Super-rough dynamics on tumour growth. Phys. Rev. Lett., 1998; 81, 4008–4011.

[8] Lotem, J. and Sachs, L., Epigenetics wins over genetics: induction of differentiation in tumor cells *seminars in* CANCER BIOLOGY, 2002; Vol. 12, 339–346.

[9] Zmeskal. O., Nezadal. M., Buchnicek, M., **HarFA,** Harmonic and Fractal Image Analyzer, www.fch.vulbr.cz/lectures/imagesci (2004).

[10] Ehrenberger, K., and Svolzil, K., Aging and Complexity in Equilibrium Dynamics Chaos, Solitons & Fractals, 1999; Vol. 10, No. 6, 1085–1086.

The Natural Environment & Human Well-Being: Insights from Fractal Composition Analysis?

Kenneth C. Cheung[1,2] and Nancy M. Wells[1,3]

[1]Cornell University [2]College of Architecture, Art, and Planning; Department of Architecture
[3]College of Human Ecology; Department of Design and Environmental Analysis
kcc22@cornell.edu

Abstract

Some researchers have suggested that analysing the physical structure of environmental stimuli may provide insight regarding an underlying characteristic of nature that contributes to human functioning. Specifically, it has been proposed that visual scenes with particular fractal characteristics (i.e. mean fractal dimension, maximum fractal dimension) are preferred by humans and may enhance functioning. Moreover, these fractal characteristics appear to be particularly common in the natural environment. This suggests that the positive effects that are generally associated with exposure to nature may be at least partially explained by human response to the mathematical structure of the sensory stimulus. This study will investigate the hypothesis that fractal composition of images predicts human preference for (and benefits derived from) nature.

1. Introduction

The notion that exposure to the natural environment positively affects human well-being has been validated by studies showing measured cognitive, psychological, and physiological benefit. This article contains a brief review of the literature regarding human preference for natural environments, followed by a brief review of the literature regarding mathematical structure of stimuli. Then, preliminary results of an empirical study are presented. The study examines whether the mathematical properties of images may be predictors of human preference for those images. Further discussion of image analysis methods provides a theoretical link between these mathematical properties and human perception of the natural environment, and is followed by a more general review of restorative environment literature, with regard to this context. It is anticipated that use of the HarFA software will aid in timely completion of the experiments.

2. Human Preference for Natural Environments

Many studies have documented children's preference for natural green spaces. These studies show that children's favourite spaces are predominantly outdoors, in natural settings (eg. Department of the Environment, 1973; Korpela, 2002). A study by Sobel (1993) found that children generally preferred natural play spaces, when examining both British and Caribbean children. Lynch (1977) found that children universally appreciated vegetation, in an international study of the experience of growing up in cities. It has additionally been found that such natural settings, which are preferred by children, also have a beneficial effect on their well-being (Wells & Evans, 2003). This connection, between preference and well-being, will be discussed further, later in this article.

3. Mathematical Structure of Stimuli

Recent research has explored specific characteristics of the natural environment that may underlie its beneficial effect on humans. This work suggests mathematical explanations for the differing effects of natural and non-natural environments.

The work of Field (1987) demonstrates a possibility for statistically characterizing images that draws a general mathematical distinction between the visual environments of the natural and non-natural kind, with his finding that natural imagery possesses fractal-like properties. Taylor and his

colleagues (Taylor, Micolich, & Jonas, 1999; Taylor 2002) also report fractal properties, as a way of characterizing natural imagery, and as a predictor for appeal of (preference for) some types of artwork.

Furthermore, Olhausen and Field (2000) suggest that such properties may provide insight into the human neurological systems associated with sensory processing. Hughes (2001) similarly suggests a relationship between the mathematical structure of preferred and beneficial stimuli, to neurological and physiological function. His work, addressing the structure of auditory stimuli, also suggests the importance of fractal like traits (i.e. scale invariant repetition and periodicity), and the prevalence of these traits in the natural environment (Gray, Krause, Atema, Payne, Krumhansl, & Baptista 2001).

These studies suggest that the beneficial effects that are generally associated with exposure to nature may be more specifically associated with the mathematical structure of the sensory stimulus. Furthermore, distinct (fractal) characteristics of the natural image may be reflected in the neurological function of the human sensory system, resulting in a physiological basis for differing responses to natural and artificial environments.

The psychological and cognitive effects, which are evident as natural environment responses, provide a means of testing the relationship between image structure and the human natural environment response. This study specifically examines a hypothesized relationship between image structure and preference of children, through the examination of the effects of image structure on preference ratings, for a series of greyscale images. The main hypothesis is that human preference rating for the images will be predicted by their image structure; that greater preference will be observed for those images that have the most natural statistical characteristics, independent of whether or not they are natural, non-natural, or computer generated.

4. Participants

The participants were children of similar socioeconomic status and geographical position (mean age of approximately 11). Data on personal background, physical activity, and daily exposure to nature were also collected.

5. Independent Variables

The images were either photographs of the natural environment, the non-natural (manmade) environment, or computer generated patterns. The images were intentionally difficult to recognize (the participants were told beforehand that they were “just patterns”). There were six examples in each category, representing a range of image structure within each category. The image structure characteristics used are statistical measures obtained through brightness (intensity) analysis, fractal dimension analysis, and wavelet analysis.

6. Dependent Variable

Preference ratings were obtained, according to a five point Likert scale, for all nineteen images, through one-on-one verbal interviews.

7. Image analysis

The fractal dimension values, used in this study, were obtained through an adaptation of the traditional “box counting” method. Traditional box counting yields a fractal dimension score that characterizes the properties of, for instance, the black area of a binary (black & white) image. The adapted method used in this study instead characterizes the properties of the border (i.e. between the black and white).

Since the box counting method relies on binary (black and white) data, non-binary images must be converted through a technique known as thresholding. In this process, a threshold must be predetermined, as the intensity value (brightness) above which is essentially converted to white, and below which is converted to black, yielding a binary image. Since the images used in this study were

greyscale (non-binary) images with content across the complete range of intensity (brightness), fractal dimension values were obtained across the entire range of threshold values for each image, resulting in a fractal spectrum, with fractal dimension as a function of threshold value. It is characteristics of this spectrum that this study is concerned with; the mean, variance, and maximum of this spectrum was calculated for each image used in this study.

The software used to perform the fractal analyses was HarFA, made available by Image Science Fundamentals (Zmeškal, O., Nežádal, M., & Buchnícek, M., 1999).

Overall intensity (brightness) characteristics were also analysed, for each image. Mean intensity and intensity variance were calculated from the intensity histogram of each image. The composite intensity histograms for the images in all three categories showed similar statistical characteristics. Generally speaking, all images tended towards a relatively normal frequency distribution of intensity.

8. Preliminary Results

Significant correlation was found between mean preference rating and mean fractal dimension ($p = 0.049$). Significant correlation was found between mean preference rating and maximum fractal dimension ($p = 0.014$).

9. Discussion

The findings of this study may support the notion that preference for nature may be more specifically associated with the mathematical structure of the sensory stimulus. Further study should include specific measures of cognitive functioning employed in previous restorative environment studies, along with measures of personal affect and physiological stress.

There is prior evidence of a relationship between preference and the cognitive and physiological benefits. Many studies show the cognitive and physiological benefit of exposure to natural environment, in addition to psychological benefit described above (Ulrich et al 1990, 1991; Parsons et al 1998, Driver, 1976; Knopf, 1987; Schroeder, 1989). A study of unstressed subjects (Ulrich, 1981), that showed an effect of more positively toned emotional states, for exposure to nature scenes, also showed broadly consistent recordings of brain electrical activity of the subjects, suggesting that the individuals were more “wakefully relaxed” during exposure to nature (Ulrich, 1981). Additionally, it has been shown that surgical patients in rooms with windows looking out on a natural scene showed benefits, including shorter postoperative hospital stays, and requiring fewer potent analgesics, as opposed to patients in similar rooms, but with windows facing a brick building wall (Ulrich 1984). A study by Wells showed that cognitive functioning in children, following a move to a different home, was higher for those whose new homes had greater levels of nature nearby (Wells, 2000). Likewise, studies have shown both immediate and durational effects of exposure to the natural environment on cognitive functioning (Hartig, Mang, & Evans, 1991, Driver, 1976; Knopf, 1987; Schroeder, 1989)

It has additionally been found that coherent autonomic response (e.g. skin conductance) to specific environmental stimuli can occur in the absence of recognition or conscious awareness of the elements (Ohman, 1986; Ohman et al., 1989). “Other studies have found that well defined emotional responses to stimuli (assessed by facial electromyography) can occur so rapidly that it is difficult to reconcile with a purely ‘controlled’ cognitive response perspective on humanenvironment interactions (Dimberg, 1990; Ulrich, 1991).” These findings eliminate the suggestion that people may be conditioned, through cultural influences, to develop positive associations with nature (e.g. Tuan, 1974), as a sole mechanism in restorative environment theory.

Theoretical bases for the positive psychophysiological effect of the natural environment have been widely published – most notably, Attention Restoration Theory (Kaplan & Kaplan 1989) and the affective (rather than cognitive) response model (Ulrich 1983) - both relying on the notion of fascination. However, neither model explicitly addresses the basis for fascination itself (i.e. the characteristics of a fascinative stimulus). Assumptions that have addressed this basis include: it is the

complexity of the natural environment that contributes to its ability to fascinate (Kaplan & Kaplan 1989), and that the human species is genetically predisposed to respond, with "fascination," to the form and structure of the natural environment (Ulrich 1983).

Perspectives on such an evolutionary basis for the nature response often draw on the intuitive notion that humans' long term evolution in natural environments must have resulted in some physiological and perhaps psychological 'adaptation' to natural, as opposed to urban, physical settings. Central to this argument is the position that humans have an unlearned predisposition to respond positively to natural content (e.g. vegetation, water) and to configurations characteristic of settings that were favorable to survival or ongoing well-being during evolution (e.g. Stainbrook, 1968; Appleton, 1975; Driver & Greene, 1977; Kaplan & Kaplan, 1989; Ulrich 1983; Orians, 1986).

The evolutionary perspective has been furthered by speculation that natural content may be processed with relative ease and efficiency because the brain and sensory systems evolved in 6 (11)

natural environments, in a parallel manner (Wohlwill, 1983; Hughes 2001). Because this evolutionary tuning is lacking for urban or built environments, encounters with such settings place greater demands on processing resources, and may overload the individual or require more coping or adaptation effort (Stainbrook, 1968).

In summation, it seems possible that there exists a human response to repetition and periodicity, found within the natural environment in the form of visual stimuli. Additionally, perhaps due to the corresponding structure of the somatosensory cortex, as well as physiological function (Hughes 2001, Ivanov 1999), these naturally structured stimuli "resonate well" with the human mind and body, showing measurable effects.

The results of this study suggest that there may be elemental characteristics of the natural environment that produce, for instance, the fascination response, and that quantitatively distinguish it from the built environment. This does not necessarily imply the ability to separate such a characteristic from the natural environment and effectively reproduce it within the artificial, built environment; a proposition carries extremely powerful philosophical implications.

Towards a Physiological Basis

Previous studies on this topic have not taken into account the variability of thresholding conditions that can greatly affect the fractal dimension value obtained, for images with information over the entire range of intensity, as is commonly processed by the human eye (Olhausen & Field, 2000).

It is not surprising that intensity (brightness) characteristics did not show as a predictor for preference. Physiological aspects of the human visual system indicate a wide range of sensitivity to light intensity (with a more localized, focused sensitivity to color). The vast dynamic intensity range of natural images is managed by the human eye through adjustment of the iris, which controls the total amount of light admitted to the eye, and with neurons in the retina that do not directly register light intensity. Rather, they encode contrast, as a measure of the fluctuations in intensity relative to the mean level. This widely accepted contrast sensitive excitatory and inhibitory receptive field model of the human visual system suggests the relevance of a method of analyzing images according to threshold borders.

In research on image encoding, Olhausen and Field (2000) have suggested that image compression algorithms may provide insight into the neurological processes that take place with human vision. They propose that nature has thus found solutions that are near to optimal in efficiently encoding images of the visual environment; that the visual system has organized itself to represent efficiently the sorts of images it normally takes in, which we call natural scenes.

A clue to human neurological function may be rooted in the postulations of Horace Barlow (University of Cambridge), nearly 40 years ago - that the nervous system might be able to form representations of the underlying causes of images (Olhausen & Field, 2000). Therefore, a model for sensory function may involve fractal algorithms that probabilistically identify stimulus structures without providing a one-to-one representation. That is to say that with human image processing, we

process a mathematical compression of a visual image when we see things – allowing neural resources to be specifically directed at elements in the visual field, as desired, while maintaining a low cost understanding of the ambient environment.

10. References

[1] Appleton, J. (1975). The Experience of Landscape. London, U.K.: Wiley.

[2] Avnir, D., Biham, O., Lidar, D., & Malcai, O. (1998). Is the Geometry of Nature Fractal? Science, 279. 39-40.

[3] Baum, A., Singer, J. E. (1985). Advances in Environmental Psychology. Hillsdale, N.J.: Lawrence Erlbaum Associates.

[4] Bernaldez, F. G. & Parra, F. (1979). Dimensions of landscape preferences from pairwise comparisons. In Proceedings of Our National Landscape: A Conference on Applied Techniques for Analysis and Management of the Visual Resource. USDA Forest Service General Technical Report PSB-35. Berkeley: USDA Forest Service, pp 256-262.

[5] Chater, N., Brown, G. D. A. (1999). Scale Invariance as a unifying Psychological Principle. Cognition, 69. B17-B24.

[6] Dan Y, J. J. Atick and R C. Reid. (1996). Efficient coding of natural scenes in the lateral geniculate nucleus: experimental test of a computational theory. Journal of Neuroscience 16:3351-3362.

[7] Dimberg, U. (1990). Facial electromyography and emotional reactions. (Distinguished Contribution Award Address). Psychophysiology, 27, 481-494.

[8] Driver, B. L. (1976). Quantification of outdoor recreationists' preferences. In B. Smissen & J.Myers, Eds., Research: Camping and Environmental Education, HPEP Series No.11. University Park, PA: Pennsylvania State University, pp 165-187.

[9] Driver, B. L. & Green, P. (1977). Man's nature: innate determinants of response to natural environments. In Children, Nature, and the Urban Environment, USDA Forest Service Report NE-30. Upper Darby, Pennsylvania: Northeastern Forest Experiment Station, pp 63-70.

[10] Driver, B. L. & Knopf, R. C. (1975). Temporary escape: one product of sport fisheries management. Fisheries, 1, 24-29.

[11] Field, D. J. (1987). Relations between the statistics of natural images and the response properties of cortical cells. Journal of the Optical Society of America, A, 4:2379-2394.

[12] Field, D. J. (1994). What is the goal of sensory coding? Neural Computation 6:55901.

[13] Field, D. J. & Brady, N. (1997). Visual Sensitivity, Blur and the Sources of Variability in the Amplitude Spectra of Natural Scenes. Vision Research, 37(23). 3367-3383.

[14] Gray, P. M., Krause, B., Atema, J., Payne, R., Krumhansl, C., Baptista, L. (2001). The music of nature and the nature of music. Science, 291(5501). 52-54.

[15] Hagerhall, C. M., Purcell, T., & Taylor, R. (2004). Fractal dimension of landscape silhouette outlines as a predictor of landscape preference. Journal of Environmental Psychology, 24. 247-255.

[16] Hartig, T., Mang, M. & Evans, G. W. (1991). Restorative effects of natural environment experiences. Environment and Behavior, 23(1). 3-26.

[17] Herzog, T. R. (1987). A Cognitive Analysis of Preference for Natural Environments: Mountains, Canyons, and Deserts. Landscape Journal, 6(2). 140-152.

[18] Herzog, T. R. (1997). Reflection and attentional recovery as distinctive benefits of restorative environments. Journal of Environmental Psychology, 17: 165-170.

[19] Hughes, J. R. (2001). The Mozart Effect. Epilepsy & Behavior, 2. 396-417.

[20] Hughes, J. R. (2002). The Mozart Effect: Additional Data. Epilepsy & Behavior, 3. 182-184.

[21] Kaplan, S., Kaplan, R. & Wendt, J. S. (1972). Rated preference and complexity for natural and urban visual material. Perception and Psychophysics, 12, 354-356.

[22] Kaplan, S. (1978). Attention and fascination: The search for cognitive clarity. In S. Kaplan & R.Kaplan (Eds.), Humanscape: Environments for people (pp. 84-90). Belmont, CA: Duxbury (Ann Arbor, MI: Ulrich's Books, 1982).
[23] Kaplan, S. & Kaplan, R. (1982). Cognition and Environment: Functioning in an Uncertain World. New York: Praeger.
[24] Kaplan, S. (1987). Mental fatigue and the designed environment. In J. Harvey & D. Henning (Eds.), Public Environments (pp. 55-60). Washington, DC: Environmental Design Research Association.
[25] Kaplan, S., & Talbot, J. F. (1983). Psychological benefits of a wilderness experience. In I. Altman & J. F. Wohlwill (Eds.), Human Behavior and environment: Vol. 6. Behavior and the natural environment (pp. 163-203). New York: Plenum.
[26] Kahneman, D., & Treisman, A. (1984). Changing views of attention and automaticity. In R. Parasuraman & P. R. Davies (Eds.), Varieties of attention. New York: Academic Press.
[27] Keller, J. M., Chen, S., & Crownover, R. M. (1989). Texture Description and Segmentation through Fractal Geometry. Computer Vision, Graphics, and Image Processing, 45. 150-166.
[28] Keller, J. M., Crownover, R. M., & Chen, R. U. (1987). Characteristics of Natural Scenes Related to the Fractal Dimension. IEEE Transactions on Pattern Analysis and Machine Intelligence, 9(5). 621-627.
[29] Knill, D. C., Field, D., & Kersten, D. (1990). Human discrimination of fractal images. Journal of the Optical Society of America, 7(6). 1113-1123.
[30] Knopf, R. C. (1987). Human behavior, cognition and affect in the natural environment. In D.
[31] Stokols & I. Altman, Eds., Handbook of Environmental Psychology (2 Vols). New York: John Wiley, pp783-825.
[32] Mandelbrot, B. B. (1977). The Fractal Geometry of Nature. Freeman, New York.
[33] Nežádal, M., Zmeškal, O., & Buchníček, M. (2001). The Box Counting: Critical Study. www.fch.vutbr.cz/lectures/imagesci/ download/en04_zlin01.pdf
[34] Öhman, A. (1986). Face the beast and fear the face: animal and social fears as prototypes for evolutionary analyses of emotion (Presidential Address). Psychophysiology, 23, 123-145.
[35] Öhman, A., Dimberg, U. & Esteves, F. (1989). Preattentive activation of aversive emotions. In T. Archer & L-G. Nilsson, Eds., Aversion, Avoidance, and Anxiety. Hillsdale, NJ: Lawrence Erlbaum Associates, pp 169-193.
[36] Olshausen, B. A., and D. J. Field. (1996). Emergence of simple-cell receptive field properties by learning a sparse code for natural images. Nature 381:607-609.
[37] Olhausen, Bruno A. & Field, David J. (2000). Vision and Coding of Natural Images. American Scientist, 88:3, 238-245.
[38] Orians, G. H. (1986). An ecological and evolutionary approach to landscape aesthetics. In E. C. Penning-Roswell & D. Lowenthal Eds., Meanings and Values in Landscape. London: Allen & Unwin, pp 3-25.
[39] Ott, E. (1993). Chaos in Dynamical Systems. Cambridge University Press.
[40] Parsons, R., Tassinary, L. G., Ulrich, R. S., Hebl, M. R., Grossman-Alexander, M. (1998). The view from the road: Implications for stress recovery and immunization. Journal of Environmental Psychology, 18. 113-139.
[41] Pentland, A. P. (1984). Fractal-Based Description of Natural Scenes. IEEE Transactions on Pattern Analysis and Machine Intelligence, 6(6). 661-674.
[42] Schiffrin, R. M. & Schneider, W. (1977). Controlled and automatic human information processing: perpetual learning, automatic attending, and a general theory. Psychological Review. 84, 127-190.
[43] Schroeder, H. W. (1989). Environment, behavior, and design research on urban forests. In E. H. Zube & G. T. Moore, Eds., Advances in Environment, Behavior, and Design, New York: Plenum, Vol. 2, 87-117.

[44] Stainbrook, E. (1968). Human needs and the natural environment. In Man and Nature in the city. Proceedings of a symposium sponsored by the Bureau of Sport Fisheries and Wildlife. Washington, DC: U.S. Department of the Interior, pp 1-9.
[45] Taylor, R. P. (1998). Splashdown. New Scientist, 3030.
[46] Taylor, R. P., Micolich, A. P. & Jonas, D. (1999). Fractal Analysis of Pollock's Drip Paintings. Nature, 399. 422. TruSoft Inc. (1999) Benoit, Fractal Analysis System, http://www.trusoft.netmegs.com/
[47] Tuan, Y. F. (1974). Topophilia: A study of Environmental Perception, Attitudes, and Values. Englewood Cliffs, NJ: Prentice Hall.
[48] Ulrich, R. S. (1979). Visual landscapes and psychological well-being. Landscape Research, 4: 17-23. Manchester, England.
[49] Ulrich, R. S. (1981). Natural versus urban scenes – Some psychophysiological effects. Environment and Behavior, 13(5): 523-556.
[50] Ulrich, R. S., Addoms, D. L. (1981). Psychological and recreational benefits of a residential park. Journal of Leisure Research, 13(1): 43-65.
[51] Ulrich, R. S. (1983). Aesthetic and affective response to natural environment. In I. Altman & J. F. Wohlwill (Eds.), Human Behavior and environment: Vol. 6. Behavior and the natural environment (pp. 85-125). New York: Plenum.
[52] Ulrich, R. S. (1984). View through a window may influence recovery from surgery. Science, 224. 420-421.
[53] Ulrich, R. S. (1986). Human Responses to Vegetation and Landscapes. Landscape and Urban Planning, 13(1): 29-44.
[54] Ulrich, R. S., Simons, R. F., Losito, B. D., Fiorito, E., Miles, M. A., & Zelson, M. (1991). Stress recovery during exposure to natural and urban environments. Journal of Environmental Psychology, 11. 201-230.
[55] van Hateren, J. H., and D. L. Ruderman. (1998). Independent component analysis of natural image sequences yields spatio-temporal filters similar to simple cells in primary visual cortex. Proceedings of the Royal Society of London, Series B 265:2315-20.
[56] Vinje, W E., and J. L. Gallant. (2000). Sparse coding and decorrelation in primary visual cortex during natural vision. Science 287:12731276.
[57] Wells, N. M. (2000). At home with nature: The effects of nearby nature on children's cognitive functioning. Environment & Behavior, 32, 775-795.
[58] Wells, N. M. & Evans, G. W. (2003). Nearby nature: A buffer of life stress among rural children. Environment & Behavior, 35, 311-330.
[59] Wilson, E. O. (1992). The Diversity of Life. Harvard University Press. Cambridge.
[60] Wohlwill, J. F. (1983). The concept of nature: a psychologist's view. In I. Altman & J. F. Wohlwill, Eds., Human Behavior and the Environment, New York: Plenum, Vol. 6, Behavior and the Natural Environment, 5-37.
[61] Zajonc, R. B. (1980). Feeling and thinking: preferences need no inferences. American Psychologist, 35, 151-175.
[62] Zmeškal, O., Nežádal, M., & Buchnícek, M. (1999). HarFA - Harmonic and Fractal Image Analyzer, http://www.fch.vutbr.cz/lectures/imagesci/harfa.htm

Fractal Analysis of Apple Flesh Structure

Ľubomír Kubík

Department of Physic, Slovak University of Agriculture in Nitra, Tr. A. Hlinku 2, 94976 Nitra, Slovak Republic, Lubomir.Kubik@uniag.sk

1. Introduction

Box-Counting method was used for evaluating of the fractal properties of the apple flesh texture. The method is often used to determine fractal box dimension of digitised images of fractal structures. Nežádal et al. (2001) and Buchníček et al. (2000) have implemented Box-Counting procedure in software called HarFA, which was developed on Institute of Physical and Applied Chemistry, Technical University of Brno in Czech Republic. HarFA analyses black&white images. Box-Counting method utilizes the covering fractal pattern with raster of boxes (squares) and than evaluating how many boxes N_{BW}, $N_{BBW} = N_B + N_{BW}$ or $N_{WBW} = N_W + N_{BW}$ of the raster are needed to cover fractal completely, where:

N_B - number of black squares,
N_W - number of white squares,
N_{BW} - number of black&white squares,
N_{BBW} - number of black&white and black squares,
N_{WBW} - number of black&white and white squares.

Repeating this measurement with different sizes of boxes $r = 1/\varepsilon$ will result into logarithmical function of box size r and number of boxes $N(r)$ needed to completely cover fractal. The slopes of the linear functions

$$\ln N_{BW}(r) = \ln(K_{BW}) + D_{BW} \ln(r), \quad (1)$$

$$\ln N_{BBW}(r) = \ln(K_{BBW}) + D_{BBW} \ln(r), \quad (2)$$

$$\ln N_{WBW}(r) = \ln(K_{WBW}) + D_{WBW} \ln(r), \quad (3)$$

give D_{BW}, D_{BBW} and D_{WBW} the fractal dimensions. D_{BW} characterises properties of border of fractal pattern. D_{BBW} characterises fractal pattern on the white background and D_{WBW} characterises fractal pattern on the black background.

2. Samples and storage properties

Measurement was realized for apples of variety Topaz. Experimental measurements were realized during of apple storage from 27th October 2003 to 2nd March 2004, i.e. in the start and the finish of the storage. Thirty values of fractal dimension were evaluated for each sample and variant of fertilization. Together 240 experimental values of the fractal dimension were realized for all variants. The new samples of apples were used for each measurement.

The storage was provided in the storage boxes at the temperature from 2°C to 3°C and 90% of the air moisture content. The measurement was realized for four variants A, B, C, K of the variety Topaz.

3. Experimental measurement

Apple samples were always cut on two half parts and the section of the depth 3-4 mm was cut from the middle part. Thirty area digital images were obtained from each sample section. The pores and the grains of the apple flesh represented a fractal object. Box Counting method was used for measurement of fractal dimension. Fractal dimension characterized influence of storage on the changing of the apple flesh structure. D_{BW}, D_{BBW} and D_{WBW} fractal dimensions were determined for surfaces of the area

samples scanned by video microscope combined with color digital CCD camera GKB CS-8606S with the array of size 768 × 576 pixels and trinocular microscope MI XSZ 107.

The frame grabber KAPA PLUS that provided the collaboration with PC digitised the images. The control software IMPOR'99 was used for a camera to provide a pre-processing of the snapshots. The software HarFA 4.9.3 was used for digital filtering of images and establishing of fractal dimension. The digitised samples were adjusted on the size 768 × 576 pixels with the resolution 38 pixels/cm. The magnification forty times was obtained. The real area of scanned surface was 3,4 × 3,4 mm for each digital image. The snapshot of the original apple flesh sample of variety Topaz, variant A is represented in the *Figure 1a*. The processing of the snapshot by intensity tresholding is shown in the *Figure 1b*. The fractal dimension of the flesh structure was evaluated from the equations (1,2,3).

4. Obtained results and discussion

Fractal dimensions D_{BW}, D_{BBW} and D_{WBW} were determined from 27 points equivalent 27 raster used on the each snapshot of the samples. The values 1.67963, 1.90499, 1.82381 from the equations shown below represents the experimental values of the fractal dimensions D_{BW}, D_{BBW} and D_{WBW} of the flesh structure of the variety Topaz, variant A shown in the *Figure 1* at the beginning of storage. R is a correlation coefficient. The values in the brackets are standard deviations of the slope and intercept in the regression model.

$\ln N_{BW} = 1.67963 \ln(r) (\pm 0.03729) + 11.74606 (\pm 0.11915)$; $R = 0.98831$

$\ln N_{BBW} = 1.90499 \ln(r) (\pm 0.00846) + 12.62747 (\pm 0.02651)$; $R = 0.99951$

$\ln N_{WBW} = 1.82381 \ln(r) (\pm 0.01484) + 12.31104 (\pm 0.04651)$; $R = 0.99835$

The same procedure was realized for all 240 snapshots of the samples and the arithmetical averages of the fractal dimensions were calculated. Each average was calculated from thirty values. The 720 experimental values of fractal dimensions were used together.

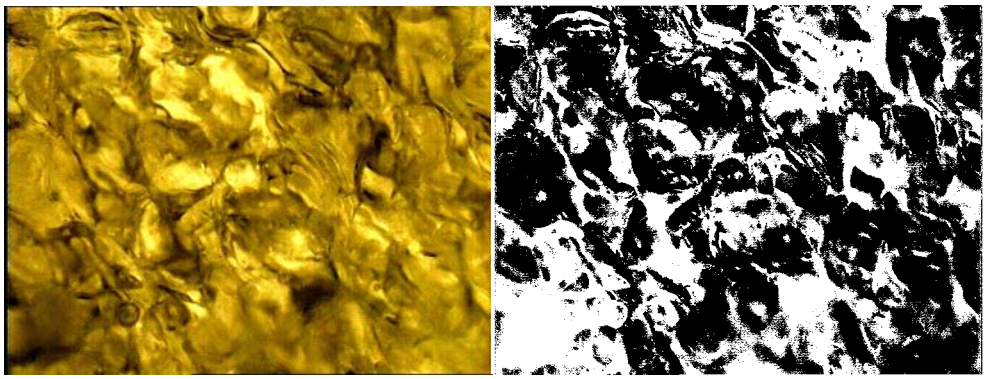

Figure 1 Original snapshot of apple flesh and the processing of the snapshot by HarFA's intensity tresholding. Variety Topaz, variant A at the beginning of storage (40 times magnification)

The graphical representation of the regression equations for one evaluation of the trinity of the fractal dimensions of the apple flesh of variety Topaz, variant A at the beginning of storage (from *Figure 1*) is shown in the *Figure 2*. D_{BW} characterized the properties of the border of black and white colour, i.e. the border of pores and grains of the fractal apple flesh. Its value was the smallest from the trinity of dimensions. D_{BBW} characterized the properties of the grains of the apple flesh structure. Its values were the highest from all. It means that the grains mesh the most part of the apple flesh structure. D_{WBW} characterizes the properties of the pores of the apple flesh and its values were between D_{BW} and D_{BBW}.

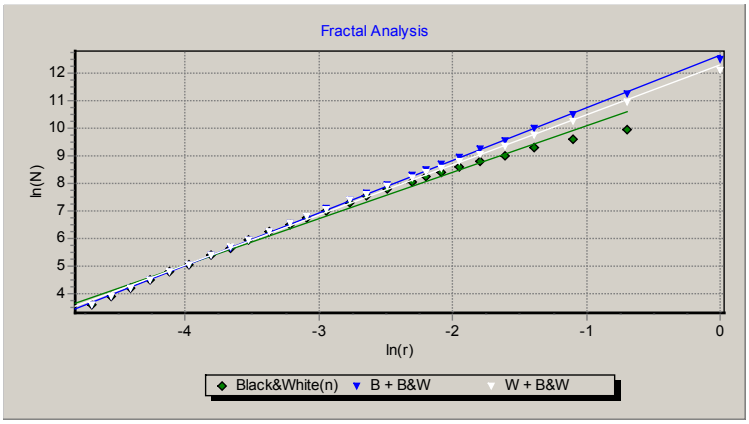

Figure 2 Determination of fractal dimensions D_{BW}, D_{BBW} and D_{WBW} by Box Counting method (software HarFA). Variety Topaz, variant A at the beginning of storage.

The study of influence of long period storage on the fractal dimension and influence of variants of fertilization in dependency on the time on the fractal dimension was also realized by statistical methods. Analysis of variance was used after data test of normality (Shapiro-Wilks'W test) and data test of variance correspondence (F-test). Statistical calculations were realized by software Statistica ver. 6.0. Analysis of variance of fractal dimension D_{BBW} of variety Topaz for factor variant of fertilization and time of storages is shown in the *Figure 3*.

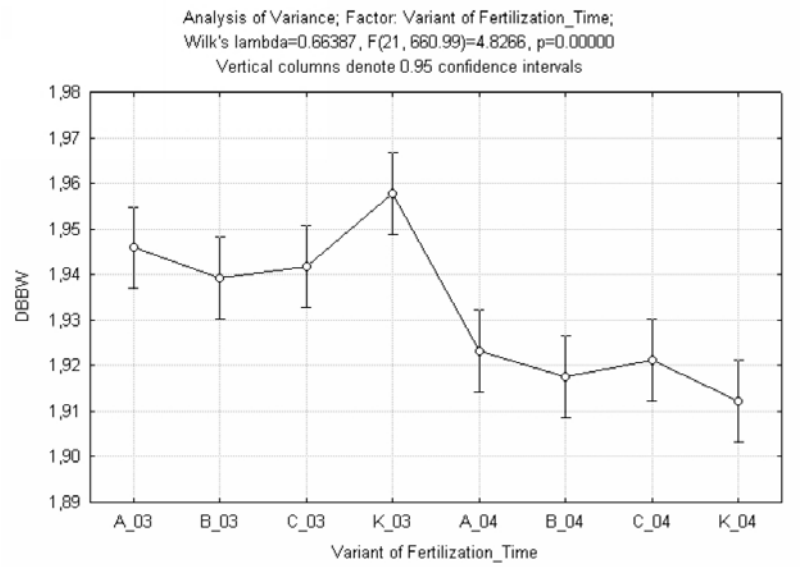

Figure 3 Analysis of variance of fractal dimension D_{BBW} of variety Topaz for factor variant of fertilization and time of storage. F is F-statistic of the F distribution and p is probability level.

5. Conclusion

The method of fractal analysis of the apples of the variety Topaz was used at the study of the apple flesh structure which is changing in the period of the long term storage in standard conditions. The fractal dimensions of the apple flesh express the degradation of apple structure caused by changing of representation of the pores and grains during the period of storage. The flesh structure transforms during long term storage in consequence of maturing and the chemical processes, which are passing inside.

The effect of the variant of fertilization and the time of storage on the fractal dimensions D_{BW}, D_{BBW} and D_{WBW} was proved by method of analysis of variance. D_{BBW} dimensions, which characterised the properties of the grains of the apple flesh structure decreased in dependency of time of storage. D_{WBW}

dimensions, which characterises the properties of the pores of the apple flesh structure increased in dependency of the time of storage.

Acknowledgement

The research was realised in the framework of the Slovak grant Agency in the project Fractal Properties of Fruits, no. 1/1321/04.

6. Literature

[1] Buchníček, M., Nežádal, M., Zmeškal, O.: Numeric Calculation Of Fractal Dimension, 3rd Coference on Prediction, Synergetic and more ..., Faculty of Technology Zlin, BUT Brno, October 2 - 3, 2000, ISBN 80-214-1668-8, p. 10-15.

[2] Lencki, R.W., Riedl K.: Effect of fractal flocculation behaviour on fouling layer resistance during apple juice micro filtration. Food Research International, 1999, 32 (4): 279-288.

[3] Nežádal, M., Zmeškal, O., Buchníček, M.: The Box-Counting: Critical Study, 4th Conference on Prediction, Synergetic and more ..., the Faculty of Management, Institute of Information Technologies, Faculty of Technology, Tomas Bata University in Zlin, October 25 - 26, 2001, ISBN 80-7318-030-8, p. 18.

Global Characterization of Time Series Using Fractal Dimension of Corresponding Recurrence Plots: From Dynamical Systems to Heart Physiology

P. Babinec, M. Kučera and M. Babincová

Department of Nuclear Physics and Biophysics, Faculty of Mathematics, Physics, and Informatics, Comenius University, Mlynská dolina F1, 842 48 Bratislava, Slovakia; email: babinec@fmph.uniba.sk

Abstract

Novel method for the global characterization of time series, based on the calculation of fractal dimension of a two-dimensional recurrence plots is proposed. The method is used for the characterization of differences between regular and chaotic systems and for the analysis of human electrocardiogram.

1. Introduction

There is a long history of using image analysis to determine the morphology of a system associated with an image [1]. Recently, techniques based on concepts from the field of artificial life have been used for image analysis [2]. The measures of complexity that they use involve fractal dimension and percolation.

The concept of a fractal dimension to describe structures, which look the same at all length scales, was first proposed by Mandelbrot [3]. Although in strict terms, this is a purely mathematical concept, there are many examples in nature that closely approximate a fractal object, though only over particular ranges of scale. Such objects are usually referred to as *self-similar* to indicate their scale-invariant structure. In simple terms, the common characteristic of such fractal objects is that their length (if the object is a curve, otherwise it could be the area or volume) depends on the length scale used to measure it, and the fractal dimension tells us the precise nature of this dependence.

Our aim in this study is to apply the concepts of fractals to global characterization of time series through the fractal structure of their two-dimensional images – recurrence plots.

2. Visual recurrence analysis method

Recurrence Plots (RPs) are relatively new technique for the qualitative assessment of time series [4]. With RP, one can graphically detect hidden patterns and structural changes in data or see similarities in patterns across the time series under study. The fundamental assumption underlying the idea of the recurrence plots is that an observable time series is the realization of some dynamical process, the interaction of the relevant variables over the time. Because the effect of all the other (unobserved) variables is already reflected in the series of the observed input, one can recreate a topologically equivalent picture of the original multidimensional system behaviour by using the time series of a single observable variable [5]. Furthermore, the rules that govern the behaviour of the original system can be recovered from its output.

Recurrence plots are intricate and visually appealing [6]. They are useful for finding hidden correlations in highly complicated data. Because they make no demands on the stationarity of a data set, RPs are particularly useful in the analysis of systems whose dynamics may be changing. The use of recurrence plots in time-series analysis has become more common in recent years, particularly in the area of physiology, for instance, they have been used to discern between “quiet“ and “active“ breathing in laboratory rats [7] or to study neuronal spike trains in cats [8]. RPs have been also used in mathematical problems primarily to identify transition points in non-stationary data sets [9], and in the

area of molecular dynamics simulations as a tool for the detection of transients and both linear and nonlinear state changes.

An RP is a two-dimensional representation of a single trajectory. The time series spans both ordinate and abscissa and each point (i, j) on the plane is shaded according to the distance between the two corresponding trajectory points y_i and y_j. In an unthresholded RP (UTRP) the pixel lying at (i, j) is color-coded according to the distance, while in a thresholded RP (TRP) the pixel lying at (i, j) is black if the distance falls within a specified threshold corridor and white otherwise. RPs are symmetrical along the $x = y$ axis, where each point is plotted against itself, and this diagonal roughly represents time [10]. Figure 1 shows UTRPs generated from four different data sets: (a) a time series electrocardiogram, (b) a time series of a Brownian motion, (c) a time series of a Dow Jones index. The colors on these plots range from white for very small spacing to dark blue for large inter-point distances, as shown on the calibration bars in the figure. With this in mind, the sine-wave RP is relatively easy to understand; each of the "blocks" of colour simply represents half a period of the signal. The RP generated from a chaotic data set is far more complicated, although it too has block-like structures resembling to what might be expected from a periodic signal. For random signal, the uniform (even) distribution of colours over the entire RP is expected and the colours on the UTRP for the time sequence "deepen" away from the main diagonal.

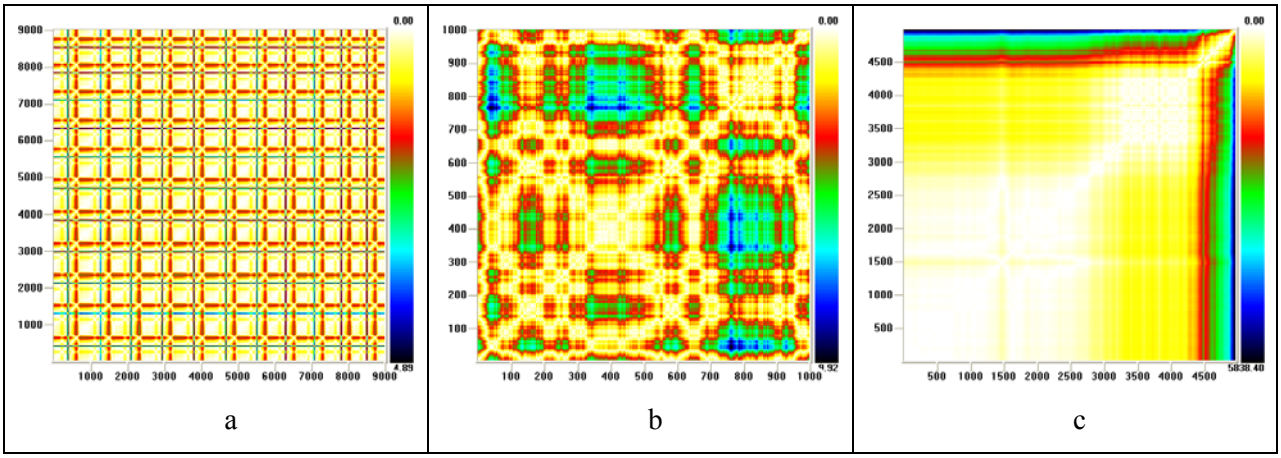

Figure 1 Recurrence plots of (a) a time series electrocardiogram, (b) a time series of a Brownian motion, (c) a time series of a Dow Jones index. On the right side of each recurrence plot is shown calibration bar showing its colour range.

The basic idea behind the interpretation of the RPs is simple: if the underlying signal is truly random and has no structure, the distribution of colours over the RP will be uniform, and so there will not be any identifiable patterns. If, on the other hand, there is some determinism in the signal generator, it can be detected by some characteristic, distinct distribution of colours. The main advantage of the recurrence plots over another widely used techniques as for example Fourier analysis, is that they preserve both temporal and spatial dependence in the time series. Even though Fourier analysis reveals the distribution of spectral frequencies, it does not show how self-similar, resonant frequencies are patterned as a function of time. Yet, RP is mostly a qualitative tool and the precise meaning of the patterns is unknown.

Recurrence plots of the obtained time series from the DRP simulations we performed, were created with the program *Visual Recurrence Analysis* (VRA) provided by E. Kononov [11]. In VRA, a one-dimensional time series from a data file is expanded into a higher-dimensional space, in which the dynamic of the underlying generator takes place. This is done using a technique called "delayed coordinate embedding", which recreates a phase space portrait of the dynamical system under study

from a single (scalar) time series. To expand a one-dimensional signal into an m-dimensional phase space, one substitutes each observation in the original signal X(t) with vector

$$y(i) = \{x(i), x(i - T), x(i - 2T), ..., x(i - (d - 1)T)\} \quad (1)$$

where i is the time index, d is the embedding dimension and T represents the time delay. As a result, we have a series of vectors

$$Y = [y(1), y(2), y(3), ..., y(N - (d - 1)T)] \quad (2)$$

where N is the length of the original series. Using $T = 1$ merely returns the original time series; one-dimensional embedding is equivalent to no embedding at all. Proper choice of the time delay and the embedding dimension is said to be critical to this type of phase space reconstruction. Only correct values of these two parameters yield embeddings that are guaranteed to be topologically equivalent to the original (unobserved) phase-space dynamics [5].

Once the dynamical system is reconstructed, a recurrence plot can be used to show which vectors in the reconstructed or original space are close and far from each other. VRA calculates the Euclidean distances between all pairs of vectors and codes them as colors.

Essentially, UTRP is a color-coded matrix D, where each $[i][j]$th entry is calculated as the distance between vectors $Y(i)$ and $Y(j)$ in the reconstructed series

$$D_{ij} = \sqrt{(x(i) - x(j))^2 + (x(i-d) - x(j-d))^2 + ... + (x(i-(m-1)d) - x(j-m-1)d)^2} \quad (3)$$

in the case of $d = 1$

$$D_{ij} = |x(i) - x(j)| \quad (4)$$

After the distances between all vectors are calculated, they are mapped to colors from the predefined colour map and are displayed as coloured pixels in their corresponding places.

3. Calculation of fractal dimension

The images were analysed using program *HarFA 5.1* provided by O. Zmeskal [12] based on the improved box counting method where binary images were covered with different grids (box length ε), and the number of boxes $N(\varepsilon)$ required to cover the structures of the images is recorded

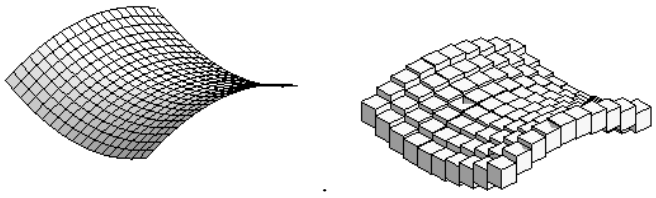

If an object is fractal, $N(\varepsilon)$ increases according to the relation

$$N(\varepsilon) = C\varepsilon^D \quad (5)$$

where D is fractal dimension and C is a constant. From this equation the fractal dimension can be obtained as

$$D = \lim_{\varepsilon \to 0} \{-\log(N(\varepsilon)) / \log(\varepsilon)\}. \quad (6)$$

The HarFA code is based on counting of squares (black, white, and partially black) from a squared network behind the fractal figure. The difference between calculated and exact values of fractal dimensions obtained using HarFA is very small (e.g. for Sierpinsky triangle the error is less than 0.2 %).

4. Comparison of regular and chaotic systems

Determinism in the mathematical sense means that there exists an autonomous dynamical system, defined by a first order ordinary differential equation $\dot{\boldsymbol{x}} = f(\boldsymbol{x})$ in a state space $\Gamma \subset \mathrm{R}^d$, which we assume to be observed through a single measurable quantity $h(x)$. The system thus possesses d natural variables, but the measurement is usually nonlinear projection onto a scalar value. Deterministic chaos offers an interesting explanation for the emergence of aperiodicity and unpredictability. Since rather simple systems exhibit chaos, one is lead to use nonlinear time series methods to verify whether such source of unpredictability is underlying a given observation. In fact, the concept of deterministic low-dimensional chaos has proven to be fruitful in the understanding of many complex phenomena despite the fact that very few natural systems have actually been found to be low-dimensional deterministic in the sense of the theory. Deterministic chaos is not the only, and not even the most probable source of aperiodicity. The superposition of a large number of active degrees of freedom can produce extremely complicated signals, which may not be distinguishable from randomness. Stochasticity in the sense that a system is driven by processes whose dynamics are too complex to be inferred from the information stored in the observations is the most frequent source of unpredictability in open systems and field measurements.

To investigate the capabilities of this method we have used three time series, sine function – prototype of regular deterministic signal, the same signal slightly perturbed with white noise, and white noise itself. In Figure 2 are shown the series together with their recurrence plots produced using VRA program. These plots (images without the frames, bars and captions, of course) were then analyzed using HarFA program. The obtained fractal dimensions are shown in Figure 3. As can be seen the fractal dimensions in this case correlate with the complexity of the signals.

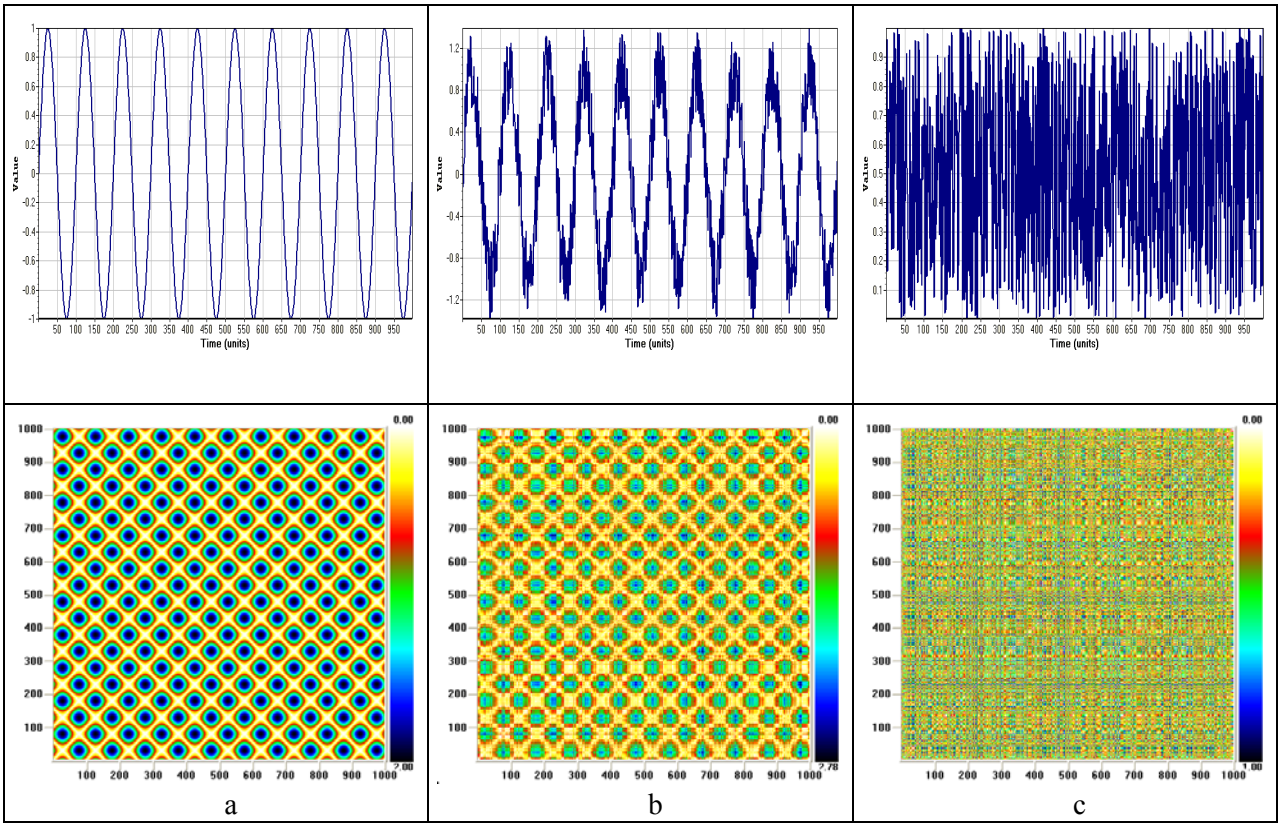

Figure 2 Time series and recurrence plots of (a) time series derived by sampling the function sin*(t), (b) a time series of a sine perturbed with white noise signal, (c) a time series of a random signal (white noise). On the right side of each recurrence plot is shown calibration bar showing its colour range.*

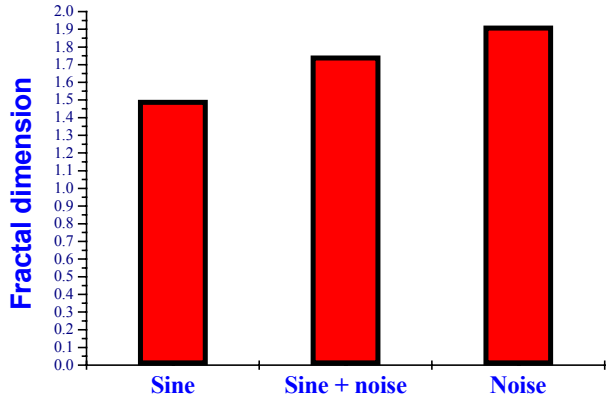

Figure 3 Fractal dimensions of a recurrence plots of the corresponding time series.

5. Applications in heart physiology

In the mid-1880's Ludwig and Waller discovered that the electrical activity of the heart could be monitored through the skin. Their device, called a capillary electrometer, used sensor electrodes and magnets to generate an electrical field. A capillary tube with fluid was placed in the field. As current passed through the electrodes, the field increased and decreased causing the fluid in the tube to bounce up and down. This device, as cool as they probably thought it was, was far too crude for clinical use. Einthoven devised a clever system for recording the same electrical activity on light-sensitive paper. Noticing a recurring pattern of movement, Einthoven named the prominent waves alphabetically, P, Q, R, S, and T the P-wave, representing the impulse across the atria to the A/V node; The QRS representing the impulse as it travels across the ventricles; the T-wave, representing the repolarisation of the ventricles (Figure 4).

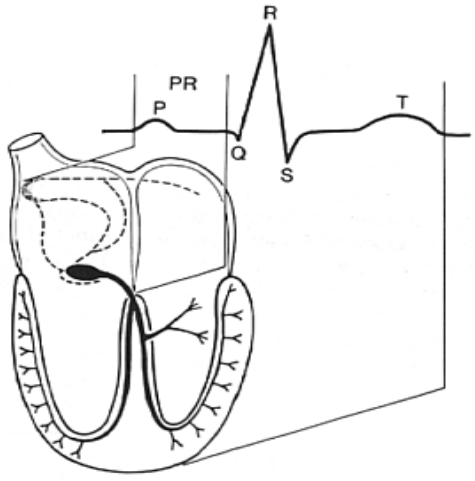

Figure 4 Anatomy of the heart with assignment of P, Q, R, S, T, and P waves.

Inter-beat intervals of a two groups of healthy subjects, young (mean age 27 yr.) as well as 5 old (mean age 74 yr.) were analysed in our recent study [13]. A. L. Goldberger, Harvard University, made these data available. Subjects lay supine for 120 min while continuous ECG signals were collected. All subjects remained in an inactive state in sinus rhythm while watching the movie ”Fantasia” (Disney) to help maintain wakefulness.

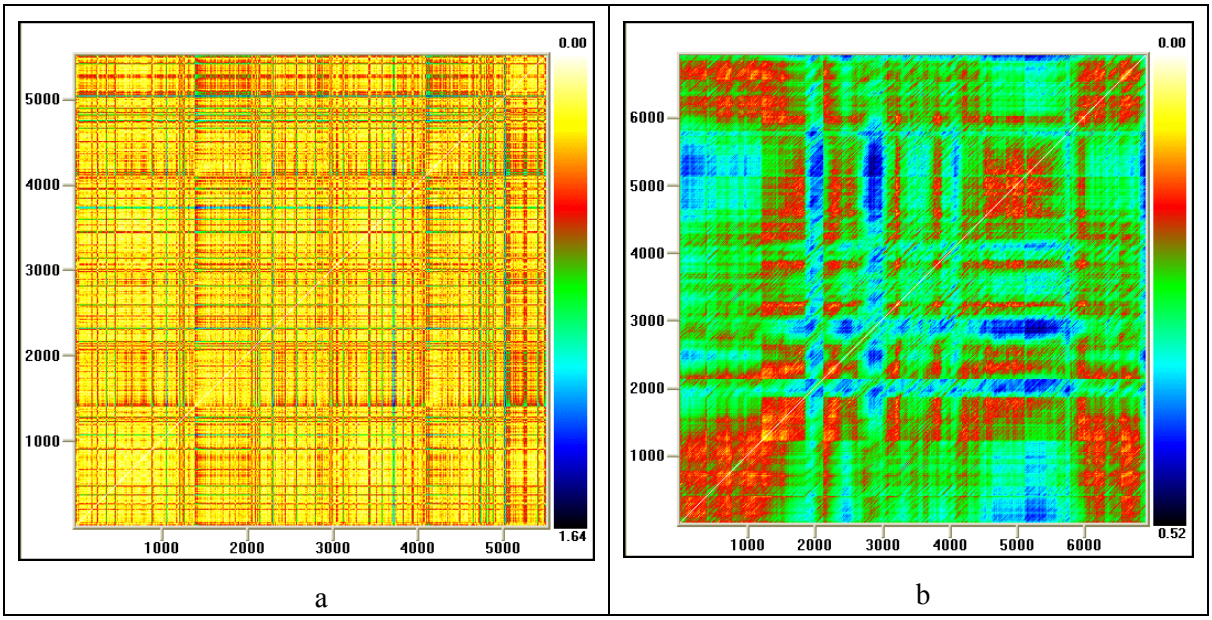

Figure 5 Recurrence plots corresponding to ECG of a young (a) and an old person (b).

The continuous ECG was digitised at 250 Hz. Each heart-beat was annotated using an automated arrhythmia detection algorithm, and each beat annotation was verified by visual inspection.

The R-R interval (inter-beat interval) time series for each subject was then computed and using them we have constructed recurrence plots as those shown in Figure 5.

Fractal dimensions of these plots are equal to 1.61 and 1.82 for old and young persons, respectively. This reflects the fact that the data obtained from old subjects have a more deterministic origin and the data obtained from young subjects are more random and complex. The complex dynamics of the healthy heart-beat arise from numerous coupled control systems and feedback loops that regulate the cardiac cycle on different time scales. Aging has a profound impact on many of the interacting neural and endocrine mechanisms that regulate heart rate, which may explain why the heart-rate time series loses much of its complex, irregular behaviour. This suggests that the distinctive patterns evident in recurrence plots of inter-beat intervals are empirically correlated with the age of the studied subjects, as they diagrammatically represent the complex dynamical interaction of the sympathetic and parasympathetic nervous systems.

6. Conclusions

In this study we have for the first time demonstrated fractal nature of recurrence plots and used fractal dimension of these images for the interpretation of various time series.

Acknowledgement

This work was supported by VEGA grant 1/2012/05.

References

[1] P. Soile, (2002) *Morphological Image Analysis*, Springer-Verlag, New York.

[2] Spillman, W.B., Jr. and Huston, D.R., Cellular automata for image analysis of damage in large structures. *Optical Engineering* 37, 898, (1998).

[3] Mandelbrot, B.B., How long is the coast of Britain? Statistical self-similarity and fractional dimension. *Science* 156, 636-638, (1967).

[4] Eckmann, J. P., Kamphorst, S. O. and Ruelle, D., Recurrence plots of dynamical systems. *Europhysics Letters, 4,* 973-977, (1987).

[5] Takens, F., Detecting strange attractors in turbulence. In*: Dynamical Systems and Turbulence*, Lecture Notes in Mathematics, No. 898, Springer-Verlag, Berlin, (1981).

[6] Marwan, N. URL: http://www.recurrence-plot.tk/

[7] Webber, C L., and Zbilut, J. P., Dynamical assessment of physiological systems and states using recurrence plot strategies. *Journal of Applied Physiology, 76,* 965-973, (1994).

[8] Kaluzny, P., and Tarnecki, R., Recurrence plots of neuronal spike trains. *Biological Cybernetics*, 68, 527-534, (1993).

[9] Trulla, L.L, A. Giuliani, J.P. Zbilut, and Webber, C.L., Recurrence quantification analysis of the logistic equation with transients, *Physics Letters A,* 223, 255-260, (1996).

[10] Zbilut, J. P. and Webber, C. L., Embeddings and delays as derived from quantification of recurrences. *Physics Letters A,* 171*,* 199-203, (1992).

[11] Visual Recurrence Analysis (*VRA*) can be downloaded from the following URL: http://home.netcom.com/~eugenek/download

[12] Zmeskal, O., Bzatek, T., and Nezadal, M., *HarFA*: Harmonic and Fractal Image Analyser. Software for determination of fractal dimension. Available at the following URL: http://www.fch.vutbr.cz/lectures/imagesci, (2005).

[13] Babinec, P., Zemanová, L. Babincová, M., Randomness and determinism in human heart-beat dynamics: Recurrence plot analysis, *Physica Medica*: *International Journal of Medical Physics*, 18, 63-68, (2002).

Fractal dimension of U373 astrocytoma cells in DMEM or RPMI cultures

I. de la Haza, J. Cobo-Molinos, M. Garrido-García, J. Navas*, P. Rueda, C. Torres, A. Caruz, F.J. Esteban

Departments of Experimental Biology and Mathematics*, University of Jaén, Campus Las Lagunillas s/n, 23071, Jaén, Spain. e-mail: festeban@ujaen.es

Abstract

In order to characterize a possible difference in the organization of U373 astrocytoma cells under different culture medium (DMEM or RPMI), we have obtained the fractal dimension (FD) of cell cultures using HarFA image analysis in the whole range of thresholding conditions (http://www.fch.vutbr.cz/lectures/imagesci/). The obtained results showed a significant increase in the astrocytoma FD depending on the time culture but not on the growth medium. We may conclude that the increased cellular organization and complexity reached in astrocytoma cultures with time, deduced from FD, is not related to the culture medium.

1. Introduction

Fractal geometry is based on the observation that structures growing apparently according to stochastic processes are not really as disordered as they appear; thus, these structures may be characterized using fractal dimension (FD) as a quantitative parameter (Fernández and Jelinek, 2001). One of the advantages of fractal analysis is the ability to quantify the irregularity and complexity of objects. In this sense, a tissue has been described as a self-organizing cellular system with fractal dynamics, where an increase in the FD has been related to aggregation and cell expansion, and a decrease in the FD with cellular differentiation (Waliszewski and Konarski, 2001).

DMEM and RPMI are the habitual media used for U373 astrocytoma cell cultures. The aim of our work is to analyse the possible influence of the culture medium in the complex organization of astrocytoma cell cultures using the FD as a discriminative parameter.

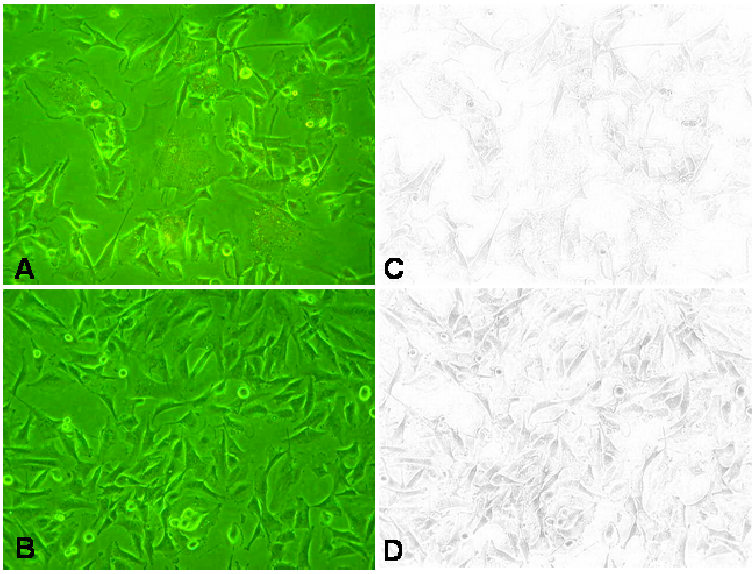

Figure 1 Astrocytoma cultures in RPMI medium at time 0h and 24 h, before (A, B) and after processing (C, D) with ImageJ, respectively.

Obtaining the fractal dimension from image analysis is not a trivial procedure because it depends on the particular image thresholding. To avoid a biased decision, we have selected the FD corresponding

to the slope change detected in the whole range of thresholding conditions, a very useful processing tool implemented in HarFA fractal analysis software.

2. Methods

U373 human astrocytoma cells were propagated in RPMI (with Glutamax) or DMEM (Gibco) media, both supplemented with 10 % (v/v) heat-inactivated fetal calf serum (Linus) and Penicillin-Streptomycin (Sigma). RGB images were taken 24 hours after seedling (time 0h) and twenty-four hours later (time 24h) for each experimental group ($n = 5$). Images were processed (RGB to 8-bit conversion and background subtraction) using ImageJ software (http://rsb.info.nih.gov/ij/) (*Figure 1*). After this, a FD analysis was carried out from the whole range of thresholding conditions using HarFA v4.9 software (http://www.fch.vutbr.cz/ lectures/imagesci/); we selected the FD corresponding to the slope change as indicated in *Figure 2*. Statgraphics Plus 5.1 was used as the statistical software.

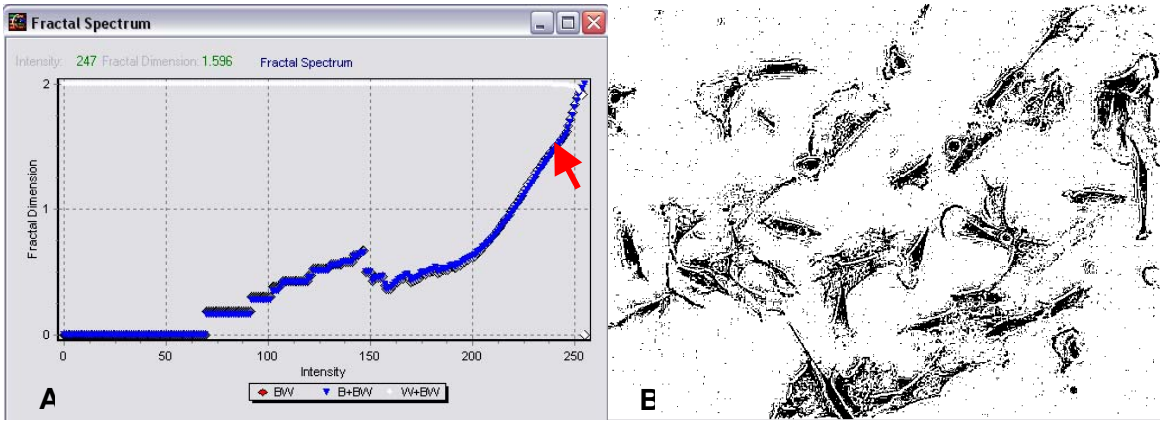

Figure 2 A: HarFA fractal spectrum; the red arrow indicates the change in the slope where the FD is selected. B: thresholding related to FD in A.

3. Results and Conclusion

Figure 3 shows the obtained individual values of FD corresponding to each experimental group. A significant increase was only detected when comparing the mean (±σ) FD related to time of culture (DMEM, 0h vs 24h: 1.54±0.11 vs 1.76±0.10, $p < 0.05$; RPMI 0h vs 24h: 1.60±0.07 vs 1.78±0.02, $p < 0.05$).

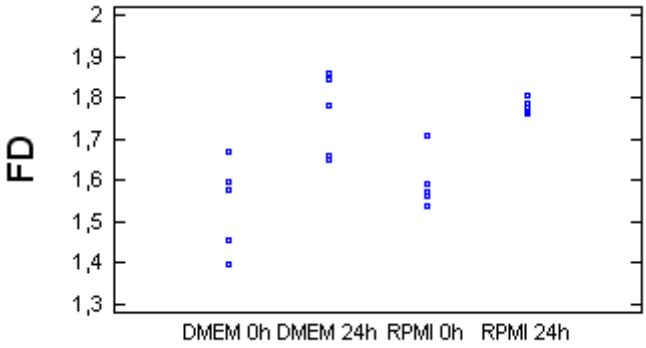

Figure 3 Fractal dimension (FD) for each image and group

From the obtained results, we conclude that the increased cellular organization and complexity reached in astrocytoma cultures with time, deduced from FD image analysis, is not related to the culture medium.

Acknowledgements

Supported by *Junta de Andalucía* (CVI-302).

References

[1] Fernández E, Jelinek HF. (2001) Use of fractal theory in neuroscience: methods, advantages, and potential problems. Methods, 24: 309-321.

[2] Walisewski P, Konarski J. (2001) Tissue as a self-organizing system with fractal dynamics. Adv. Space Res., 28: 545-548.

A Computational Analysis of Multi-temporal Vegetation Changes Using the Fractal Dimension Spectrum

J.C. Linares[§]*, F.J. Esteban¶, B. Viñegla*, J.A. Carreira*

Area of Ecology[§], University Pablo de Olavide, Ctra. Utrera, Km. 1, 41013 Sevilla (Spain). Department of Experimental Biology[¶] and Area of Ecology*, University of Jaén, Las Lagunillas s/n, 23071, Jaén (Spain).
e-mail: festeban@ujaen.es

Abstract

We present a methodological work for testing and applying the use of both Fractal Spectrum (FS) and Fractal Dimension (FD) to discriminate and quantify, respectively, cover and structure changes along time in a relic *Abies pinsapo* Boiss. (Pinaceae) forest located at Andalusia (southwestern Mediterranean Basin). To achieve this, plots at different elevation were selected from Orto-rectified aerial photographs of the same locations taken at different dates (from 1957, 1991 and 2001). The selected images were analyzed using *HarFA* software (http://www.fch.vutbr.cz/lectures/imagesci/) in the whole range of thresholding conditions, which allows us to use the Fractal Spectrum (FS) as a criterion for forest cover delimitation and FD characterization. In order to test the accuracy of the method, image thresholding was also determined by mean of a conventional supervised classification of the aerial photographs using *ImageJ* analysis software (http://rsbweb.nih.gov/ij/). The obtained results showed FS analysis might improve the criterion of visual delimitation of forest cover in landscape digital images and, thus an optimal FD characterization. Finally, the obtained FD provided an adequate parameter for detecting the increase in forest cover and vegetation structure diversity in image time analysis series.

1. Introduction

Fractal Dimension (FD) [1] is a useful tool to quantify the inherent irregularity of nature. Fractals are self-similar and infinitely detailed, and the related FD is an index of its morphometric variability and complexity; moreover fractal analysis has been applied to a variety of natural objects [2] and the FD may be obtained even if the object is not a fractal. Thus, among the different methods of FD calculation, the box-counting method is the most appropriate in landscape structural FD estimation because it can be apply to fractal patterns with or without self-similarity.

Potential applications of fractal geometry are not limited to quantifying natural lines and surfaces. Fractal geometry may produce new methods for estimating stand density, predicting forest succession, and describing the form of trees. It is shown that the fractal dimension of tree crowns is a good indicator of various tree and site features such as species tolerance, crown class, and site quality [3]. The aim of our work is to analyse the possible use of Fractal spectrum (FS) in image classification and FD as indicator of stand complexity in Orto-rectified aerial photographs from 1957, 1991 and 2001of relic *Abies pinsapo* Boiss. (Pinaceae) forest from Andalusia in the southwestern Mediterranean Basin.

2. Material and Methods

Digital panchromatic aerial photographs from 1957, 1991 and 2001 were used in order to analyse changes in forest coverage and structure in the last 50 years. ArcView GIS 3.2 (ESRI) was used for selecting, scaling and geographic coordinate determination of plots (six plots of 17.9 ha - 550 m × 325 m - from each image). A digital map scale 1:10000 was simultaneously used to confirm the correct selection of the plot and to determine the mean elevation in metres at sea level (thereafter m a.s.l.).

FS and FD of the digitalized images were obtained using the fractal functions implemented in *HarFA 5.1* software (http://www.fch.vutbr.cz/lectures/imagesci/). A deep computational fractal analysis of images may be easily achieved using *HarFA*, because it includes three categories of the necessary

boxes for the box-counting method: N_W, which contains only the white background; N_B, which covers only the black segmented object; N_{BW}, which covers the border of the black object (e.g., those boxes which contains at least part of the black object). According to this counting mechanism it obtains not one but three FDs (FD_W, FD_B, FD_{BW}). Another two FDs (FD_{B+BW}, FD_{W+BW}) can also be computer from N_{B+BW} (the sum of N_B and N_{BW}) and N_{W+BW} (the sum of N_W and N_{BW}). The FS in the whole range of thresholding conditions, also implemented in *HarFA*, was applied to the selected images in order to test the FS as a criterion for thresholding. To confirm this, a conventional image analysis of the plots was carried out by independent observers (experts in the study area and vegetation type) using the computerized-assisted image analysis software *ImageJ* (http://rsbweb.nih.gov/ij/), where the pixel intensity range and the fraction area of *Abies pinsapo* forest was obtained avoiding shadowy zones corresponding to rocks and others topographical irregularities. In addition, the pixel intensity value obtained after interpolation in the FS graph was also used as the conventional maximum threshold delimitation at each image to confirm that FS graphical interpolation is an adequate approach for thresholding and FD relationship (*Figure 1*); to obtain an appropriate FD parameterization, the box-size range was selected after a single slope analysis.

The pixel intensity obtained using both approaches (conventional and FS thresholding) was correlated by linear regression; a statistical significance was tested for $p < 0.01$ [4]. In addition, one-way ANOVA was applied to test FD differences in the time series [5].

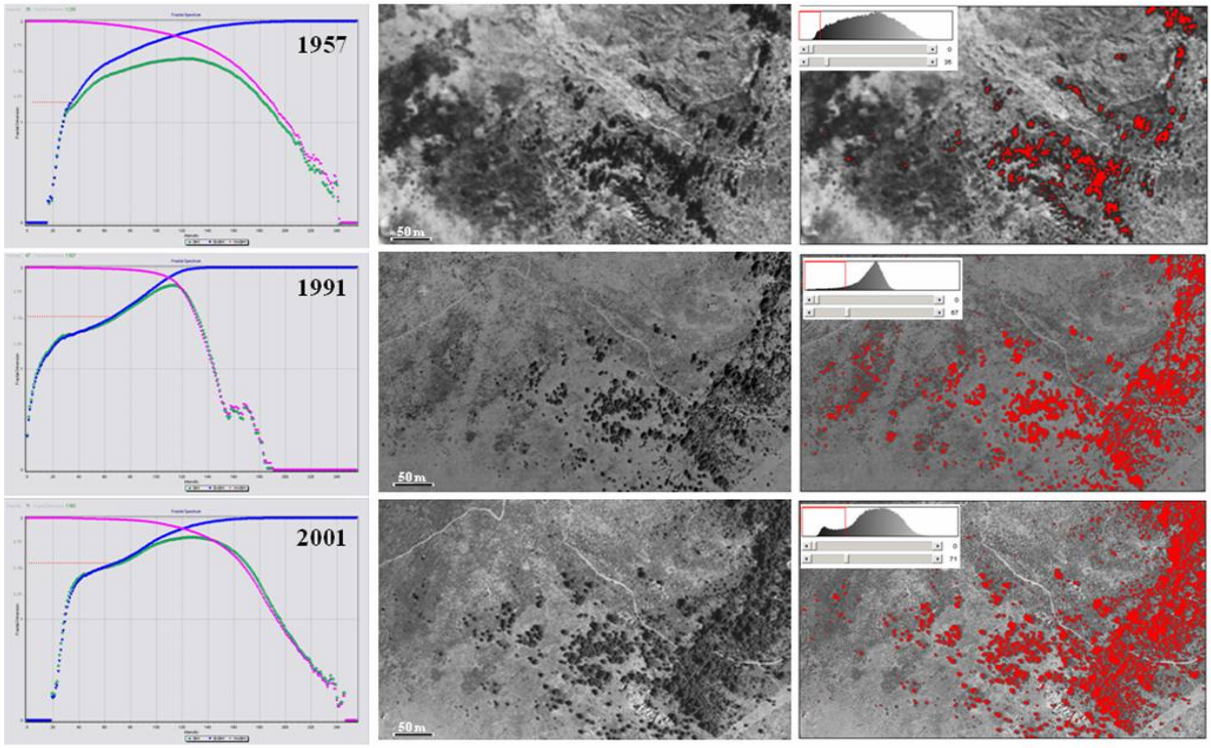

Figure 1 FS (left column) of the selected aerial images (middle colum) at different dates. The selected FD (red horizontal line at left column) was appropriated since it corresponds to an adequate -independently selected- forest covering threshold (right column).

3. Results and Discussion

3.1. Conventional and FS thresholding relationship

Figure 1 shows that the more adequate FD for each image corresponds to the inflexion point of the FS curve related to FD_{B+BW}, because the interpolated pixel intensity value may be used as an appropriate thresholding value for forest covering. Under this value, the pixel range includes the most

darkness values (only a mosaic from black and white spots was obtained) and, thus, FD_{B+BW} is too small. Over the selected interpolation point, the range of pixel intensities included is too large, and the forest patches will disappear by overlapping, where the FD_{B+BW} reached a maximum. This visual transition is well noticeable when FS is running in *HarFA*. The critical inflexion point may be also easily detected because just over this point is when the FD_{B+BW} (blue line in *Figure 1*) value start to be different to the FD_{BW} value (green line in *Figure 1*), the functional meaning corresponding to the limit of the forest cover; so, the suitable criterion to determine both the FD and the corresponding pixel range is the first FD_{B+BW} value higher than FD_{BW} value. *Figure 2* shows the linear regression between the values obtained from conventional (visual) and FS thresholding approaches ($p < 0.01$, $R^2 = 0.79$, $n = 18$). Thus, we can assume that the FD_{B+BW} at this threshold is a representative parameter of the forest stand complexity.

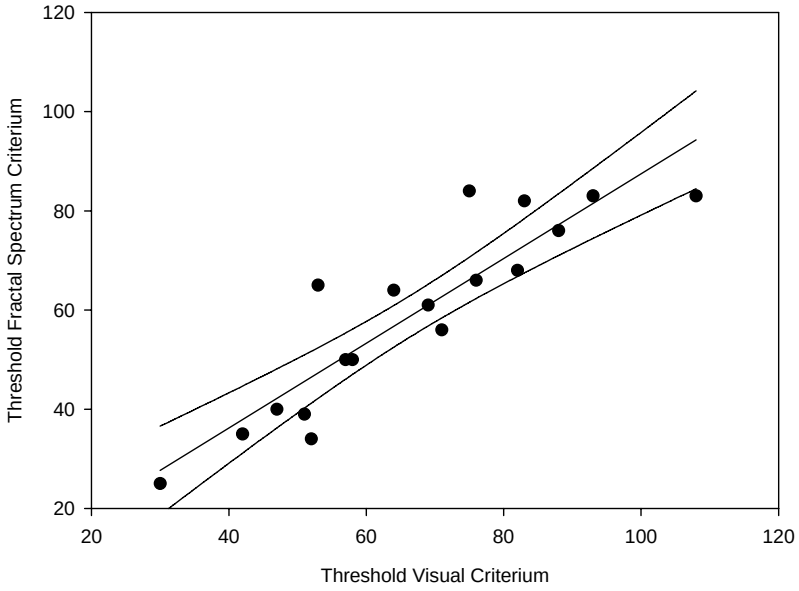

Figure 2 Linear regression performed between the threshold obtained from visual and FS delimitations ($p < 0.01$, $R^2 = 0.79$, $n = 18$).

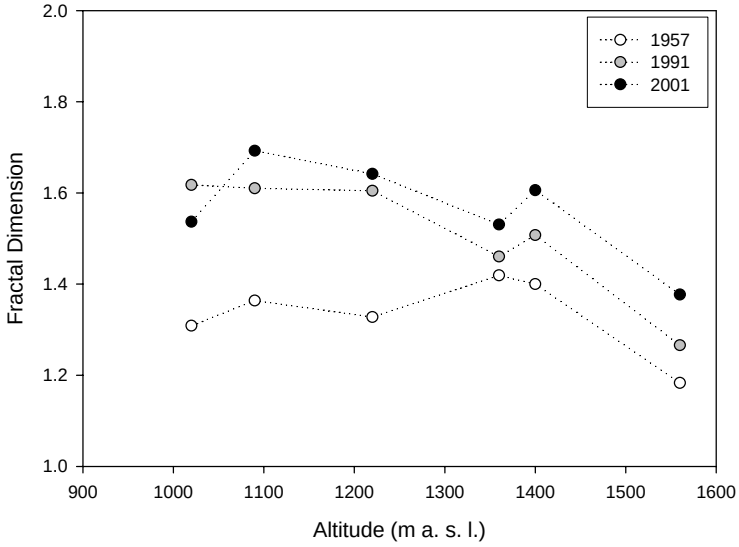

Figure 3 Final (tendency analysis) of the FD obtained for 1957 (empty circles), 1991 (grey circles) and 2001 (black circles).

3.2. FD as indicator of forest change

Significant differences were found between the FD and the corresponding dates (*Figure 3*). The FD from 1975 plots was 1.33 ± 0.08 (mean ± standard deviation), which was lower than the obtained at 1991 and 2001 images: 1.51 ± 0.17 and 1.56 ± 0.11 ($p < 0.05$ and $p < 0.01$), respectively; however, statistically significant differences were not found between 1991 and 2001 plots. Within dates, it appears to be a fall in the FD at those plots located at upper elevation (m a.s.l.). These results suggest that the increased forest cover and vegetation structure diversity reached in the last 50 years can be detected after image FD analysis. In addition, and as stated above, FS may improve the criterion of the forest cover visual delimitation. Because radiometric attributes of images differ among dates, and this radiometric correction is difficult and not at all cases reliable and useful, we consider that the independent classification of each image by mean of a quantitative approach, as the Fractal Dimension Spectrum analysis implemented in *HarFA*, complete and improve any conventional (as visual) criteria.

Acknowledgments

Supported by *Junta de Andalucía* (CVI-302 and RNM-296).

References

[1] Mandelbrot BB. 1982. *The fractal geometry of nature*. W. H. Freeman and Co., New York.
[2] Sugihara G, May RM. 1990. *Applications of Fractals in Ecology*. Trends in Ecology and Evolution 5:76-86.
[3] Zeide B. 1991. *Fractal geometry in forestry applications*. Forest Ecology and Management 46:179-188.
[4] Zar JH. 1999. *Biostatistical Analysis* (4th ed.). Prentice Hall, New Jersey.
[5] Sokal RR, Rohlf FJ. 1995. *Biometry* (3rd ed.). New York.

Surface Defects Evaluation by Fractal Geometry and Statistical Analyses

Vlastimil Hotař, František Novotný

Technical University of Liberec, Department of Glass Producing Machines and Robotics,
Hálkova 6, 460 17 Liberec
vlastimil.hotar@tul.cz

1. Introduction

Many natural structures cannot be described by conventional methods, because they are complex and irregular. Relatively a new approach is the application of fractal geometry [1]–[3]. This geometry is successfully used in science, but an application in industry is sporadic and experimental only. However, the fractal geometry can be used as a useful tool for an explicit, objective and automatic description of production process data (laboratory, off-line and potential on-line).

The data having complex and structured character can be also met during a glass manufacturing. The data may have a form of digitalized pictures, time series (progressions) or a topologically one-dimensional interface (especially a surface roughness). When analysing this data, it is suitable to use - in addition to classic mathematical statistics - modern tools of the fractal geometry expressing the complexity degree of structured data by means of a single number, the fractal dimension [1]–[3].

A use of the fractal dimension and statistic tools together forms an interesting and powerful tool for complex data quantification, for a poor quality source searching, a production optimalization and a non-stability of production process subsystems searching.

Now, there are tools application possibilities for monitoring for three basic data format types: digitalised photos, time series and topological one dimension dividing lines (especially surface roughness) [5]–[9]. On this account, we are developing three off-line softwares that can be converted into on-line control systems in the future. The software tools use mathematical statistics and fractal geometry. They are tested in an off-line classification of surfaces and defect pictures, in a description of time series, which were obtained from outputs of a glass production control system, for evaluation of metal surfaces (iron aluminides in comparison with the carbide-nickel steel) in contact with the glass melt as well as changes of their quality and for quality control of window glass sheet (an objectification of the corrugation test).

The following article demonstrates possibilities of the fractal geometry with combination of statistic tool for the evaluation of 2D pictures of surface defects - structures of the hole cracks in costume jewellery. Software Matlab 6.5 and HarFA 4.0 [4] were used for these experimental evaluations.

2. Methods of analyses

The explicit, objective and automatic description of images complexity can be made by different methods both statistic and fractal dimension. Only some of the possibilities are presented below.

- The process of description has five steps practically:
- Preparing of samples - structure must be visible, the costume jewellery is cut, *Figure 1A*.
- Taking digital photographs. Photos of the hole cracks in costume jewellery are from an electronic microscope, *Figure 1B* (it is possible obtain “classic” photographs and they scan).
- Software preparation of the digital photographs, *Figure 1C* (cutting of the photographs, because only some parts of the photos are important for analysis).
- Analyses of the images.
- Evaluation analyses results.

Digital image is a matrix (or matrixes) of pixels (rectangular array of points, *Figure 1D*). Pixels can reach different numbers, which depend on the used format of digital images. The pixels have numbers between 0 (black) and 255 (white) for the grey 8-bit palette bitmap and the bitmap has only one matrix. (Colour bitmap has 3 matrixes for RGB colour model – one matrix of red, green and blue colour.)

Figure 1C shows two typical poor quality surfaces of costume jewellery holes. The cutting C-1 has deep cracks and C-2 has a thin structure.

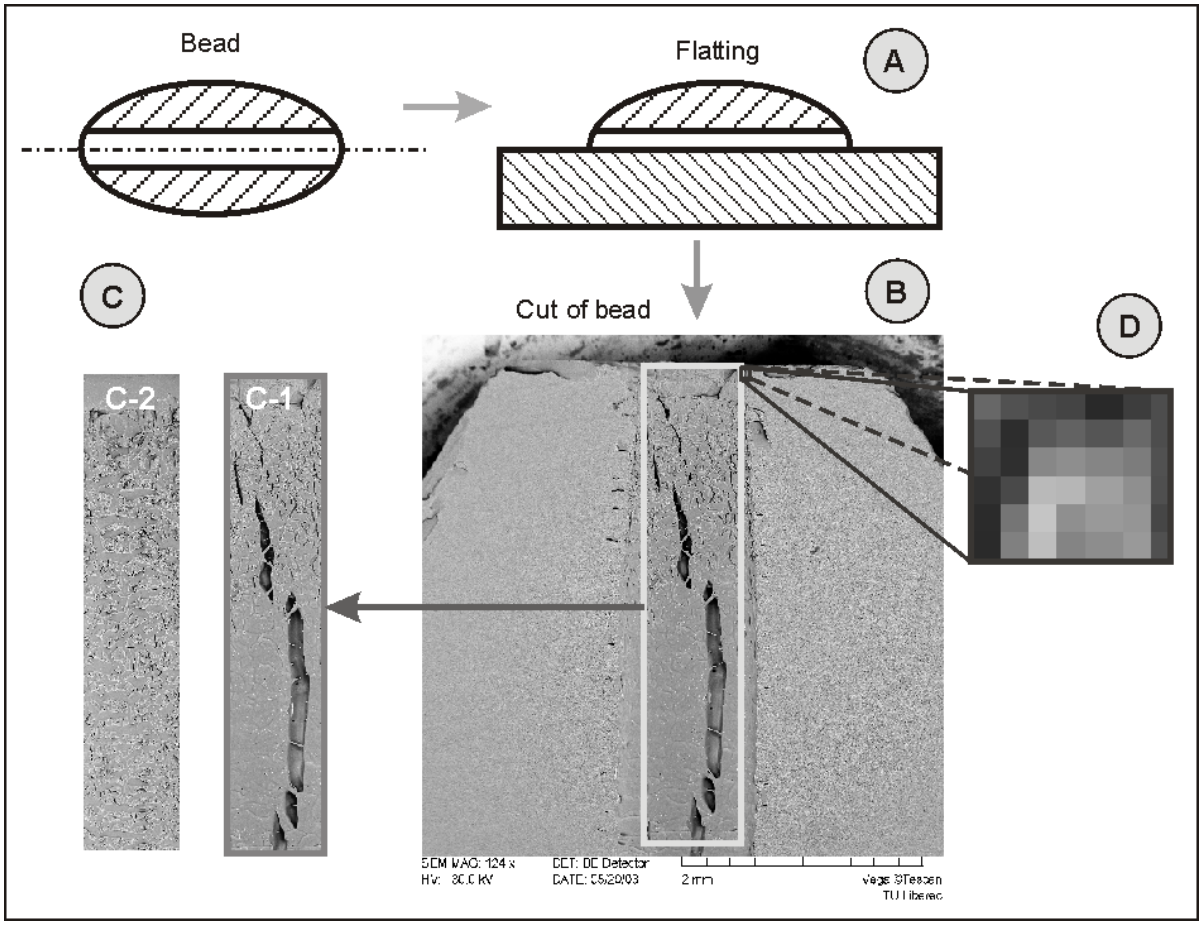

Figure 1 Preparing of samples, taking photographs, software preparation

2.1. Histogram

An evolution of a structure of the bitmap is possible by the statistical description of a histogram, *Figure 2*. Modus, median, average, range, standard deviation and other statistic tools can be used easily.

A suitable method is the histogram cut off on 5% level and the method describes the image by a single number. The analysis computes a width 90% of all pixels value of the histogram from an average value of the image, *Figure 2*.

The method is very sensitive to shadow, that can occur in the hole cracks. The analysis is easy, but describes all defects, cracks, shadows and structure together.

2.2. Thresholding

Next analyses are based on a technique called "thresholding", that transforms grey or colour image object into black & white (binary) one. The binary image can be determined from the grey 8-bit palette bitmap, where black are all pixels which fulfil condition e.g. 0 = black <= 100 and all the other pixels

become white (100 < white <=255), *Figure 3*. It means, that all pixels lesser than or equal to the threshold 100 are black and greater than 100 are white. (More than one threshold can be used or the technique for matrixes of colour images can be used too.)

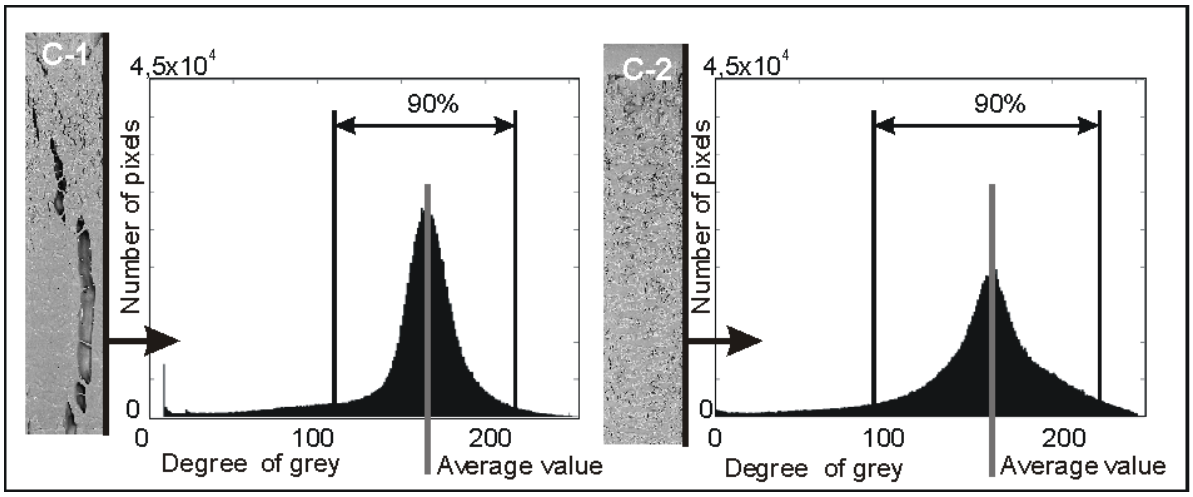

Figure 2 Histogram cut off on 5% level

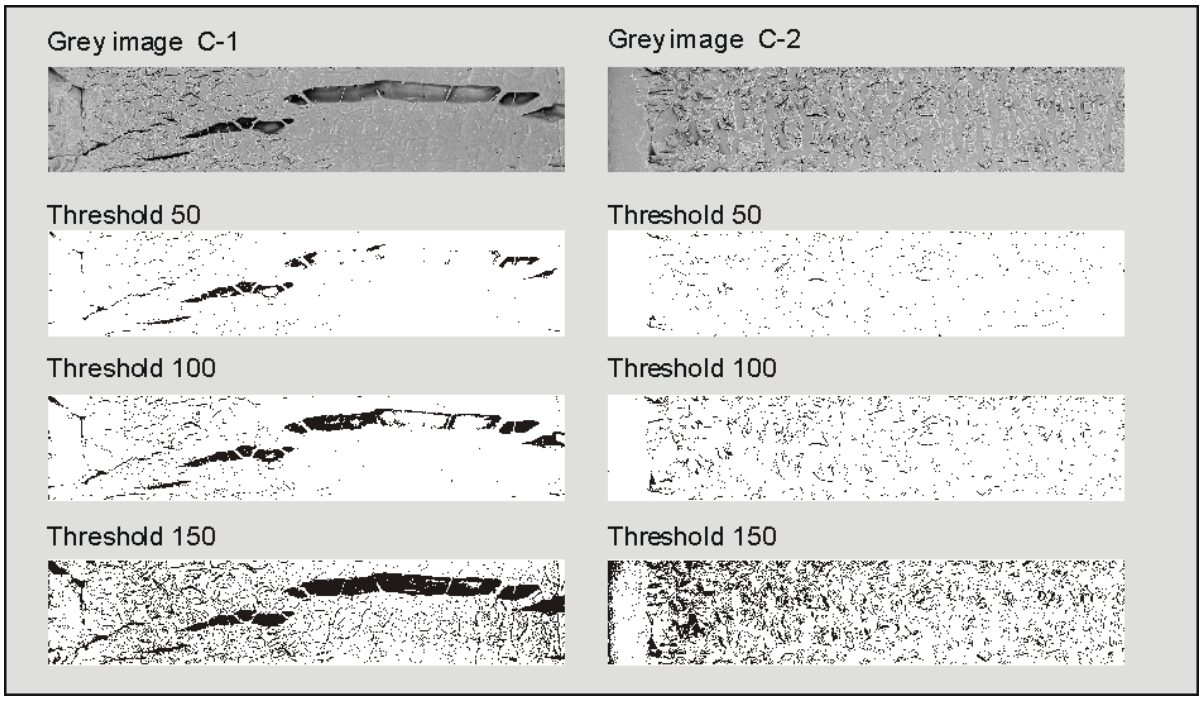

Figure 3 Thresholding of grey images

The procedure of thresholding can be used for all thresholds of the grey image, 256 binary images are obtained. An analysis is done for all binary images and as far the analysis produces single number classifying a binary image, a spectrum of dependence between single number and threshold is given (e.g. *Figure 4*).

Thresholds between 50 and 150 are suitable for the images of the hole cracks, because binary images, obtained by these thresholds, show the best structure of the surface. Thresholds between 10 and 50 show the large cracks. Binary images produced by the thresholding with thresholds over 150 contain shadow.

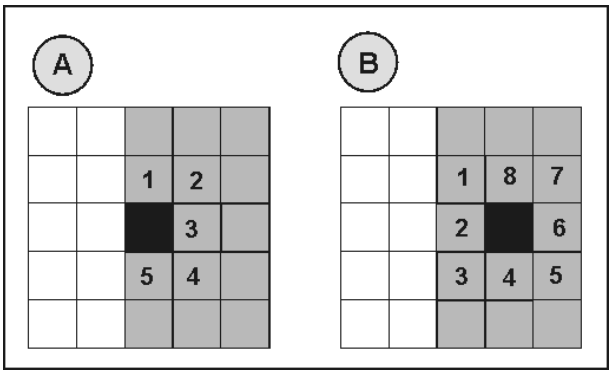

Figure 4 Percentage of black pixels of binary images spectrum

2.3. Percentage of black pixels

The analysis is based on computation of percentage of black pixels in binary images – the method computes number of black pixels in percents. It is supposed: a greater count of black pixels represents a greater complex structure and more defects.

A spectrum of dependence between percentage of black pixels of binary images and thresholds is in *Figure 4.* The analysis is easy, but describes all defects, cracks, shadows and structure together.

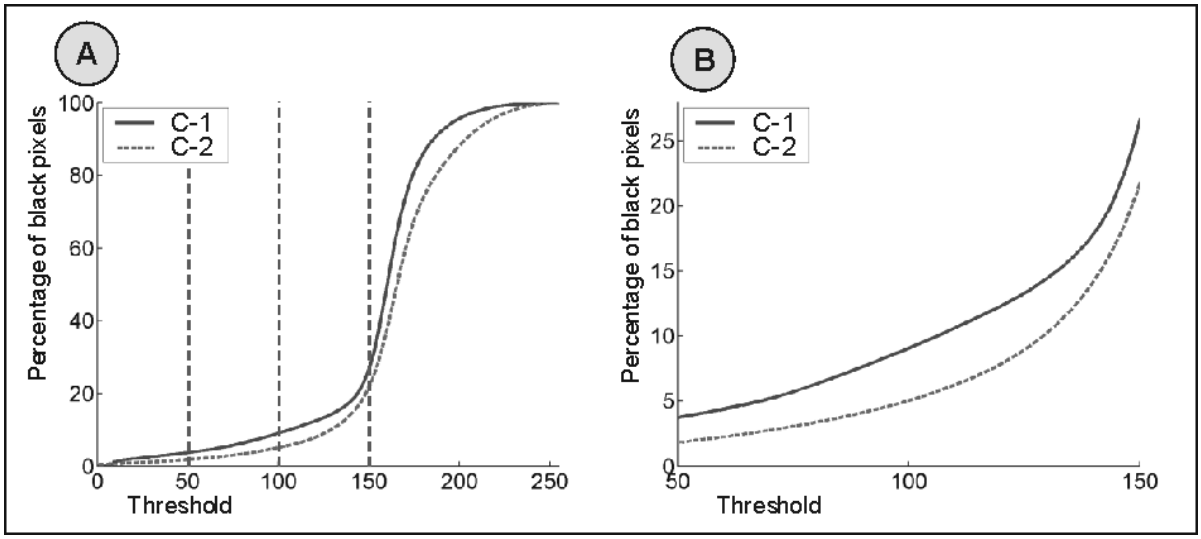

Figure 5 Pixels on boundary crack.

2.4. Percentage of deep cracks

The method is suitable for detection of relatively large and single cracks and defects. The method computes percentage of pixels with neighbouring pixels of the same value. The analysis searches black pixels (value 0) in a binary image, which have five or more neighbouring black pixels. The black pixels represent defect, structure, cracks, etc. Especially large cracks and defects contain black pixels with five or more neighbouring black pixels. *Figure 5* shows part of boundary crack. Black pixel in *Figure 5A* has five neighbours and in *Figure 5B* has 8.

Figure 6A shows spectrum of dependence between percentage of black pixels with five or more neighbouring black pixels of binary images and thresholds. For detection of large hole cracks in costume jewellery thresholds from 10 to 50 are the most suitable, *Figure 6B*. For the threshold 50, the cutting C-1 has more single cracks and defects, numerically: $T_{50\_C\text{-}1} = 3.17\%$ than the cutting C-2, numerically: $T_{50\_C\text{-}2} = 0.8\%$.

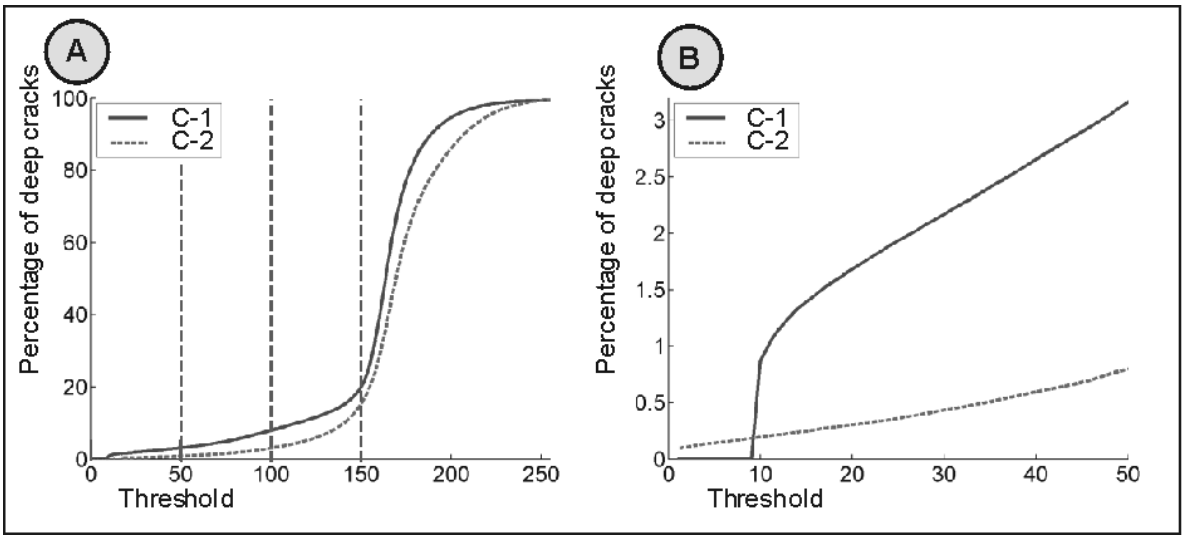

Figure 6 Percentage of black pixels with five or more neighbouring black pixels spectrum.

2.5. Box dimension

The software HarFA 4.0 [4] is used for the analysis and software tools developed in Matlab 6.5 makes data evaluation.

The box counting method is shown in [2] and based on fractal geometry. The analysis describes structure by single number: the box dimension D_B. The box counting method works by laying meshes of different sizes r and then counting numbers of boxes N needed to cover a binary image (*Figure 7A*) completely (*Figure 7B*, *C*). The number $N(r)$ of boxes needed to cover the structure is given by a power law:

$$N(r) = const. \cdot r^{-D_B} \tag{1}$$

D_B is the box dimension. Logarithmic dependence between $\log_2 N(r)$ and $\log_2 r$ is called Richardson-Mandelbrot plot (*Figure 7D*). The box dimension (that estimate fractal dimension) can be determined by slope s of the regression line in *Figure 7D*:

$$s = D_B = -\frac{\Delta \log N(r)}{\Delta \log r} \tag{2}$$

The box dimension is multiplied by 1000 for a better confrontation.

The fractal spectrum (that was discovered in project HarFA) of the cuttings C-1 and C-2 are shown in *Figure 8*. The box dimensions over threshold level 150 are similar, because over the value an influence of shadow is significant. Results of analysis for threshold level 120 are: $D_{B\_C\text{-}1}$ =1429.6 (C-1) and $D_{B\_C\text{-}2}$ = 1562.4 (C-2), where the higher value represents greater complexity of the structure in the image. The cutting C-2 is more structured than the C-1 and box dimension quantifies the structures.

3. Results

The most suitable methods for describing of structures of the hole cracks in costume jewellery box dimension and percentage of deep cracks counting appear. *Figure 9* and *10* show a selection of results. For whole analysis with classification to quality class both methods must be use.

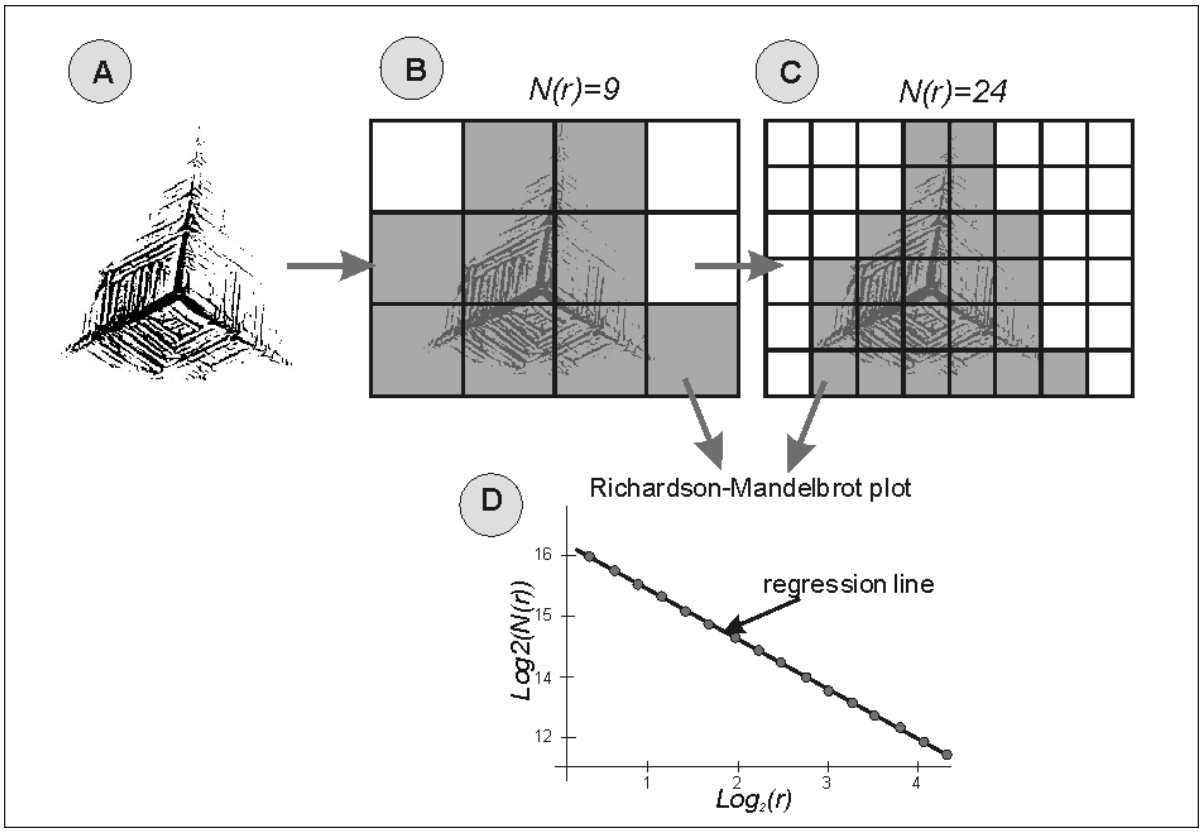

Figure 7 Box counting method.

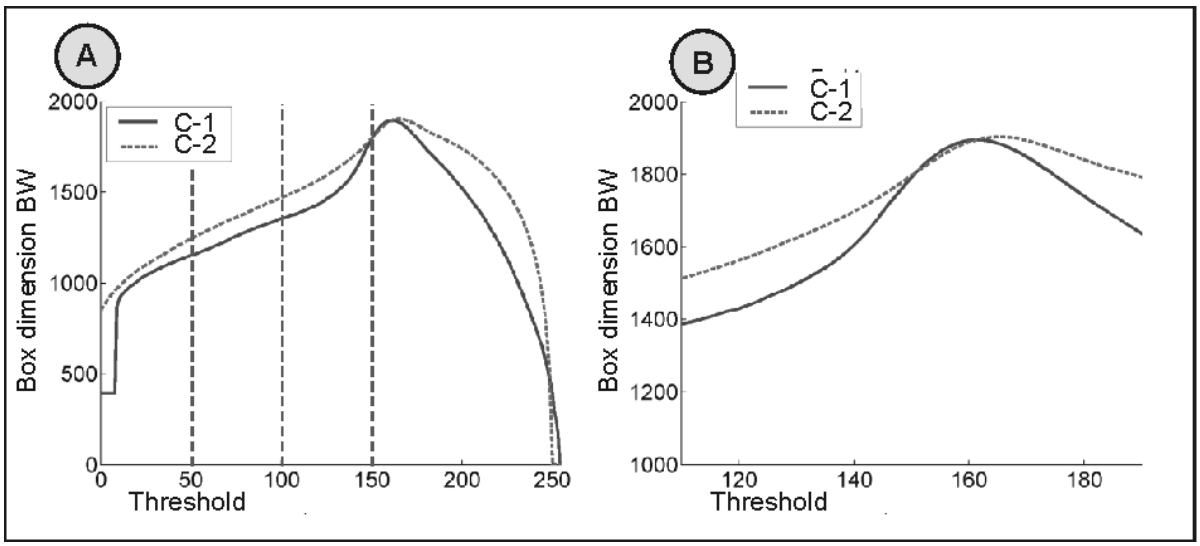

Figure 8 Fractal spectrum.

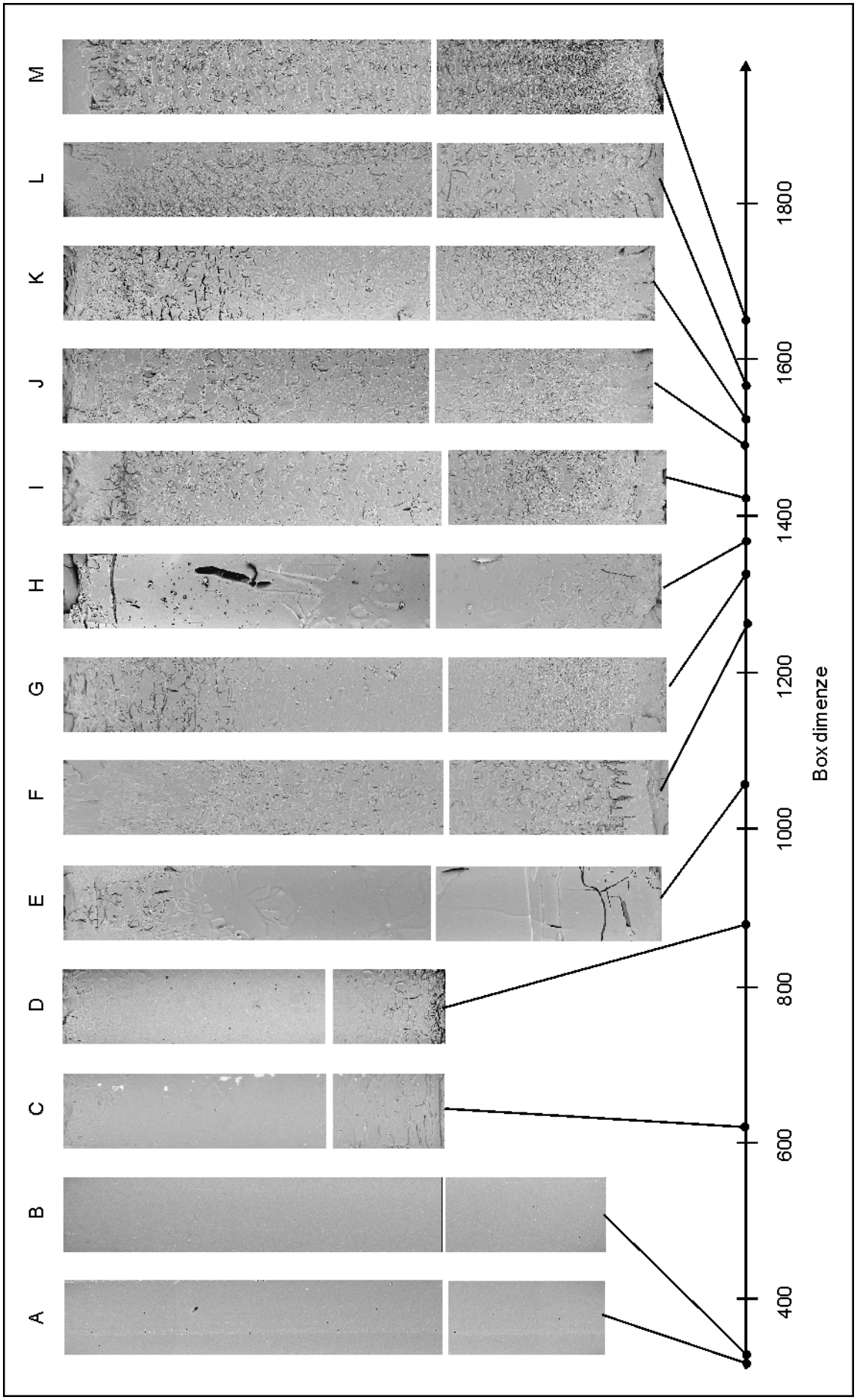

Figure 9 Selection of hole surfaces and their position in BD.

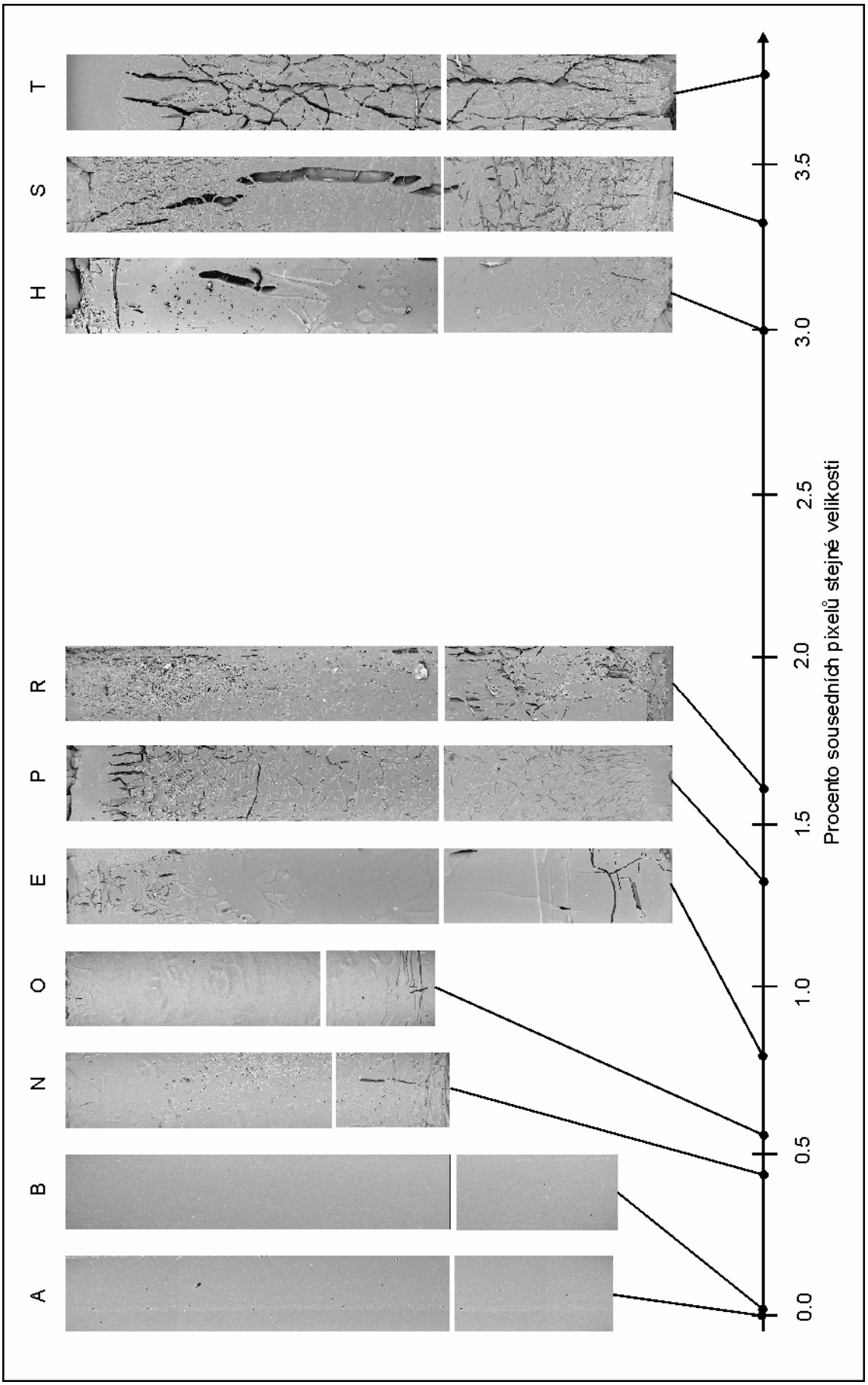

Figure 10 Selection of hole surfaces and their position in percentage of black pixels with five or more neighbouring black pixels.

4. Conclusion

Photos of structures can be described by the statistic analysis and the fractal dimension. 33 images were analysed and we found out, that percentage of deep cracks and box dimension are the most suitable for the experimental evaluation of hole cracks in costume jewellery, because two types of defects can be met in the hole: deep cracks, a thin structure. The box dimension is specialized for the thin structure and the analysis of percentage of deep cracks is specialized for the deep cracks, which is better for the explicit evaluation.

Acknowledgments

This work was created in the frame of the research project No. MSM 4674788501, which is financed by the Ministry of Education of the Czech Republic.

References

[1] Mandelbrot. B. B. *The fractal geometry of nature*. New York: W. H. Freeman and Co.,1982.

[2] Peitgen, H.O., Juergens, H. and SAUPE, D. *Chaos and Fractals: New Frontiers of Science*. New York; Berlin; Heidelberg: Springer-Verlag, 1992.

[3] Bunde, A. and Havlin, S. *Fractals in science*. Berlin: Springer, 1994.

[4] Zmeskal, O., Nezadal, M., Buchnicek, M. and Sedlak, O. *HarFA and HarFA: e-journal*. http://www.fch.vutbr.cz/lectures/imagesci/ Brno: Ústav fyzikální a spotřební chemie, 2002

[5] Hotař, V., Novotný, F. *Possibilities of Fractal Geometry Application in Glass Industry*. In: Glass Odyssey. Montpellier (France) 2002. p. 120, 6 pages.

[6] Hotař, V., Novotný, F., Hotař A. *Interpretation of the production data by means of the fractal geometry and statistical analyses*. Sklář a keramik **53** (2003), no. 7-8, p. 148-154.

[7] Hotař, V., Novotný, F. Surface *Profile Evaluation by Fractal Dimension and Statistic Tools*. In Proceedings of 11th International Conference on Fracture. Turin (Italy): CCI Centro Congressi Internazionale s.r.l., 2005. p. 58.

[8] Hotař, V., Hotař, A. *Non-conventional methods application for data evaluation in glass industry*. Sklář a keramik **56** (2006), no. 9, p. 179-184.

[9] Hotař, V. Industrial *Data Evaluation Using of Fractal Geometry*. Thesis, Liberec: Technická univerzita v Liberci, 2005.